High-Order Harmonic Generation with Structured Beams

by
Fanqi Kong

A thesis submitted to the
Faculty of Graduate and Postdoctoral Studies
in partial fulfillment of the requirements for the degree of
Doctor of Philosophy in Physics

Department of Physics
Faculty of Science
University of Ottawa

Supervisor: Prof. Paul B. Corkum

Doctor of Philosophy in Physics (2019)

Department of Physics

University of Ottawa

Ottawa, Ontario, Canada

TITLE:

High-order harmonic generation with structured beams

AUTHOR: Fanqi Kong

SUPERVISOR: Professor Paul. B. Corkum

TOTAL PAGES: ix, 100

Contents

Abstract

The generation of high-order harmonics opened an era of attosecond science wherein coherent light bursts are used to probe dynamic processes in matter with a time resolution short enough to resolve the motions of electrons. It enabled the development of extreme ultraviolet (XUV) and X-ray table-top sources with both temporal and spatial coherence, which provides the ability to shape the temporal and spatial structure of the XUV pulses.

Scientists developed techniques to control and measure the temporal structure high harmonic emissions. These techniques exploited control of the driving laser pulse in the time domain and facilitated development of more advanced high-harmonic based XUV sources that have greatly impacted ultrafast measurements.

In this thesis, I apply techniques to control and measure the spatial structure of high harmonic emissions, and discuss the underlying physics and potential applications of the interaction between spatially structured laser beams and materials. This study exploits the spatial degree of freedom in strong field interaction, which has not been given as much attention as the temporal degree of freedom.

I use liquid crystal devices to shape the wave front of a fundamental laser beam to a vortex structure, then imprint this structured wave front onto XUV beams through high harmonic generation. This method provides an alternative to special XUV optics, which can manipulate the wave front of XUV radiation by all optical means. This result also reveals the conservation of orbital angular momentum in this extreme nonlinear wave mixing process. In addition to shaping the wave front, shaping the polarization of the driving beam also allows generation of circularly polarized the XUV radiation using a high harmonic source.

This thesis also highlights the interplay between shaping the wave front and polarization in the high harmonic generation process. The topology of the structured beam can be maintained through this extreme nonlinear interaction due to the spin selection rules and spin-orbit conservation.

Moreover, this thesis demonstrates an approach to integrate a vector beam into a broadband ultrafast light source and overcome the bandwidth limitation of mode converters. We use this approach to generate a few-cycle structured beam. In the future, this beam will be used to generate a strong ultrafast magnetic impulse in gas and solid targets by driving currents in a loop, which is a valuable tool for the future of magnetic metrology.

The novel properties of structured laser beams discussed in this thesis expanded the capabilities of high harmonic based XUV sources and have opened a new field to explore this additional degree of freedom in strong field interactions.

Acknowledgements

Five years of PhD means a lot more than interesting physics experiments and fascinating scientific results. It also trained me a creative way of thinking and a responsible manner of tackling unknown problems. I am grateful to have the opportunity to work in this world-leading research lab and learn from some of the best scientists.

First, I would like to express my sincere gratitude to my PhD supervisor Prof. Paul Corkum for his continuous support to my study and related research, for his patience, motivation, and immense knowledge. His guidance helped me in all the time of study and research. He is always the best role model to me for being a responsible and honourable scientist.

My gratefulness also goes to Prof. Robert Boyd and Prof. Ebrahim Karimi, who provided me an opportunity to collaborate with their research team and shared with me profound insight based on their expertise. Without their precious support it would not be possible to conduct this research.

I would like to thank my fellow colleagues, Dr. Zhengyan Li, Dr. Chunmei Zhang, Dr. TJ Hammond, Dr. Shawn Sederberg, Dr. Donghyuk Ko, Dr. Marco Taucer, Tyler Clancy, Vicky Yu-Hsuan Wang, Dr. Ladan Arissian, Prof. Andre Staudte, Prof. David Villeneuve from both the University of Ottawa and the National Research Council of Canada for the stimulating discussions, patient guidance and the scientific passion you passed on me. I would also like to thank Graham Brown, Matthew Britton, Frédéric Bouchard, Hugo Larocque and many other the peer graduate students, for the sleepless nights we were working together, and for all the fun we have had in the last five years.

Last but by no means least, I would like to thank my family and my friends for their invaluable support throughout my PhD journey and my life in general. To my parents, Tianyi and Yandi, who unconditionally love and support me. Thank you, Xiaoxi, my eternal cheerleader, for always being there for me. I would not be here without you. You have made my PhD journey far more enjoyable.

Statement of Contributions

Joint Attosecond Science Laboratory (JASLab) is a research partnership between the University of Ottawa and the National Research Council of Canada. It involves many talented researchers who contribute to research and development. I summarize my contributions in the projects related to this thesis. My publication list at the time of writing is available below.

When I join the attosecond lab at the University of Ottawa, a new lab started to build at the Advanced Research Complex, University of Ottawa. I was involved in building and developing the infrastructure of the new lab. I also performed the testing, commissioning and calibration of the high harmonic XUV apparatus with which the major results of this thesis are performed.

In Chapter 1 I give an overview on strong field physics and beam shaping research. As an introduction, many of the concepts are the work of previous research by other researchers. References are given to the original publications where appropriate.

Chapter 2 presents analysis on how the XUV emission phase is influenced by controlling the spatial structure of the fundamental beam. I derived the theoretical analysis based on the semiclassical three-step model and performed the numerical simulation. The experimental results are published in [P4], which I was involved in setting up and performing the measurements in collaboration with Dr. Zhengyan Li, who was a post-doc in the group.

Then I led the project to use structured beams in high harmonic experiment, in which I participated in almost every part of the project from designing experiment, performing numerical simulation to analysing the experimental results. I also collaborated with Frédéric Bouchard, Hugo Larocque and Felix Hufnagel, who are graduate students from Dr. Ebrahim Karimi's research group to fabricate liquid crystal phase plates. The phase front shaping results shown in Chapter 3 are partly published in [P1].

After implementing the phase front structured beam in high harmonic generation, I then devised the project to use polarization structured beam, another important category of structured beam, in further enhancing the capability of table-top XUV sources. Chapter 4 is based on the results published in [P8] that demonstrated the capability to generate circularly polarized XUV radiation. As the project lead, I conceived and designed the experiment and performed the analysis. Combining the existing polarimetry of XUV and 2-dimensional profiling of the XUV beam, I also developed a method to characterize the polarization state of a XUV vector beam.

During the polarization shaping experiment, I came up with an idea to study the interplay between the two parts of the angular momentum, which corresponds to the polarization and phase front of a light beam. Then I designed the experiment to control the orbital angular momentum by shaping the polarization in high harmonic generation. I performed the measurement of the experimental results reported in Chapter 4, which are also published in [P5].

While developing of the lab infrastructure, I participated in integrating the structured beam into our existing ultra-fast light sources in collaboration with Dr. Chunmei Zhang, who was

the senior lab manager. In the project to produce few-cycle vector beam, I designed generation scheme and performed the beam characterization measurements. The results are published in [P6].

Publication List

[P1]
Controlling the orbital angular momentum of high harmonic vortices
F. Kong, C. Zhang, F. Bouchard, Z. Li, G. G. Brown, D. H. Ko, T.J. Hammond, L. Arissian, Robert W. Boyd, E. Karimi, P.B. Corkum
Nature Communications 8, 14970, 2017

[P2]
Perturbative High Harmonic Wave Front Control
Z. Li, G. Brown, D.H. Ko, **F. Kong**, L. Arissian, P.B. Corkum
Physical Review Letters 118 (3), 033905, 2017

[P3]
Testing the Role of Recollision in Air Lasing
M. Britton, P. Laferrière, D.H. Ko, Z. Li, **F. Kong**, G. Brown, A. Naumov, C. Zhang, L. Arissian, P.B. Corkum
Physical Review Letters 120 (13), 133208, 2018

[P4]
Perturbing laser field dependent high harmonic phase modulations
Z. Li, **F. Kong**, G. Brown, T.J. Hammond, D.H. Ko, C. Zhang, P.B. Corkum
Journal of Physics B: Atomic, Molecular and Optical Physics 51 (12), 125601, 2018

[P5]
Spin constrained orbital angular momentum control in high-harmonic generation
F. Kong, C. Zhang, H. Larocque, F. Bouchard, Z. Li, M. Taucer, G. Brown, T.J. Hammond, E. Karimi, P.B. Corkum
arXiv preprint arXiv:1810.05894, 2018

[P6]
Generating few-cycle radially polarized pulses
F. Kong, H. Larocque, E. Karimi, P.B. Corkum, C. Zhang
Optica 6 (2), 160-164, 2019

[P7]
Ultrashort magnetic impulses driven by coherent control with vector beams
S. Sederberg, **F. Kong**, P.B. Corkum
arXiv preprint arXiv:1901.07444, 2019

[P8]
F. Kong, C. Zhang, H. Larocque, Z. Li, F. Bouchard, D.H. Ko, G. G. Brown, A. Korobenko, T.J. Hammond, Robert. W. Boyd, E. Karimi & P.B. Corkum
Vectorizing the spatial structure of high-harmonic radiation from gas
Nature Communications 10, 2020, 2019

Chapter 1 Introduction

Einstein's theory of photoelectric effect revolutionized understanding of how light interacts with matter [1]. As a glimpse to the quantum world, the theory predicts no photocurrent can be produced, regardless of intensity, if the photon energy is smaller than the ionization potential of the material [2]. However, the "regardless" in this scenario has its regard, and the theory fails when the intensity of the light becomes strong enough. Light can still produce photocurrent even when the photon energy is smaller than the ionization potential. The medium has a probability of absorbing two or more photons, which overwhelms the bounding energy from the nucleus and produces photoelectric current. Intense light makes this photocurrent become measurable and gives birth to this new type of light-matter interaction.

Generally, the interaction accompanied by absorption or emission of more than one photon per elementary act is denoted as multiphoton process [3,4]. Besides producing photocurrent, multiphoton processes can produce electromagnetic radiation with new frequencies. Following this path, this nonlinear frequency conversion enabled the creation of many artificial light sources that produce radiation covering almost the entire electro-magnetic spectrum. These new technologies allowed humanity to reveal the fine structure of matter [5,6], track fast dynamics in chemical reactions [7,8], and create even more powerful light sources [9–12].

Towards longer wavelengths, radio and terahertz region, which have much lower frequencies than visible light, can be generated by nonlinear interactions such as difference frequency generation and optical wave mixing [13,14]. Towards shorter wavelengths, second-order optical harmonics can be produced by interacting with nonlinear materials without inversion symmetry [15,16]. Furthermore, multiple nonlinear effects can cascade and produce optical supercontinuum, a broadband optical radiation. This requires either high energy pumping pulses [17,18], or highly nonlinear devices, for example photonic crystal fibres [19,20]. Recent studies have shown that the generated wavelength can be tailored to the deep or even vacuum ultraviolet region by designing fibre structures and dispersion [21,22]. In a more extreme case, the field is strong enough that a high-order and nonperturbative nonlinearity extends the spectrum of the radiation to the extreme ultraviolet (XUV) or soft X-ray range. Radiation in this range has applications in photoelectron spectroscopy [23–25], advanced lithography [26] and solar imaging [27]. This high-order nonlinear interaction is named high-harmonic generation [28,29].

Different from XUV and X-ray radiation produced by sun corona or plasma-based sources which are incoherent in both time and space, XUV created through nonlinear optics inherits the coherence from its driving laser beam. This guarantees the phase of such radiation is synchronized in time and controllable in space. Furthermore, this coherent interaction ensures that the polarization of the electromagnetic radiation is largely preserved as well.

In 1993, Corkum developed a semi-classical model for high-order harmonics generation with gas molecules [30]. This model suggests a feasible route for developing XUV or X-ray light

table-top source with both spatial and temporal coherence. The model describes how a single atom interacts with an intense laser field, and how XUV radiation is produced in three steps. Using this single-atom response, the non-perturbative nature of the high harmonics is well-explained, such as spectral plateau and cut-off photon energy [28–33]. It also opened the era of attosecond science, wherein attosecond (10^{-18} s) duration laser pulses are used to probe dynamic processes in matter with a time resolution short enough to resolve the motions of electrons [11,34–36].

A number of theoretical and experimental studies expanded this model in the temporal and spatial domain [32,37], and revealed a more comprehensive picture of the generation process that guides the development towards more advanced high-harmonic based XUV sources. By understanding phase matching, high-harmonic XUV sources are extended to produce kiloelectron volts radiation [38–40], which grants us access to inner shell electron dynamics [23,41]. In the time domain, scientists have learned to control and measure the temporal structure of attosecond and high harmonic pulses. For example, a controlled driving laser pulse can produce an isolated pulse with an attosecond pulse duration [42–44], which are used in pump-probe experiments to study the electron dynamics.

In this thesis, I discuss the underlying physics when spatially structured laser beams interacting with materials and look ahead potential applications of structured XUV radiation. The study intends to exploit the spatial degree of freedom in strong field interaction, which was a new research area in strong-field physics. Shaping this additional degree of freedom opens a new field that is important for both fundamental science and ultrafast metrologies.

To study the interaction of spatially structured beams with gas and condensed phase matter, two essential technologies are implemented:

1) Femtosecond laser systems that produce repeatable and strong laser field which enables highly nonlinear interactions with gas and solid-state medium.

2) Liquid-crystal-based beam shaping technology that provides flexibility of designing spatial profiles and manipulating both the phase and polarization of laser beams.

Combining these two powerful tools allows us to inspect how the structured photons interact with the materials.

1.1 Strong field interactions and femtosecond lasers

1.1.1 From perturbative to non-perturbative interactions

Research in nonlinear optics usually involves a laser field that is weak compared to the ionization potential of interacting atomic or molecular system. Therefore, the system is almost unchanged by the presence of the external field. In this case, the polarizability of the nonlinear system can be expanded by a Taylor series described with nonlinear susceptibilities $\chi^{(n)}$ shown as Eq. (1.1) [45]

$$P(t) = \varepsilon_0 \left[\chi^{(1)} E(t) + \chi^{(2)} E^2(t) + \chi^{(3)} E^3(t) + \ldots \right], \tag{1.1}$$

where $\chi^{(n)}$ is the nonlinear susceptibilities, n is the order of nonlinearity, $E(t)$ is the time-dependent electric field and ε_0 is vacuum permittivity. This approach allows investigating numerous nonlinear optical effects involving few photons or when the optical field is weak comparing the to the potential of the atomic system.

However, as the laser field gets stronger, high order terms become non-negligible. The definition of "strong field" can be different depending on the system and process being studied. For example, in considering multiphoton absorption or ionization, the term strong field can be defined by the intensity required for the probability of absorbing (n+1) photons to be comparable to that of absorbing n photons [4]. In relativistic-laser plasma interaction, the term strong field requires that the field is strong enough to accelerate the particle to a velocity where its relativistic mass becomes comparable to two times its rest mass [46]. The term strong field in high harmonic generation, which is most relevant to this thesis, is quantified by the Keldysh parameter [47]

$$\gamma = \omega \frac{\sqrt{2m_e I_p}}{eE} , \tag{1.2}$$

where I_p is the ionization potential of the nonlinear medium, m_e is the electron rest mass, e is the electron charge, E is the amplitude of external field and ω is the angular frequency of the external field. It suggests the condition that the tunnelling ionization is likely to happen, and the wave nature or the instantaneous optical field become important. In practice, when interacting 800 nm laser pulse with noble gas atoms (e.g. argon), the critical intensity is ~0.2 PW cm^{-2}. At this intensity, the potential of the atomic system is altered by the presence of the external field, and the external field becomes comparable to the Coulomb forces experienced by the electron. In this condition, the external field can no longer be treated as a small perturbation, and perturbation theory fails. Multi-photon processes and higher order nonlinearities start to appear. The intensity is so high that the probability of absorbing multiple photons increases. Several multiphoton processes involving electronic dynamics (ionization, electronic rescattering, etc.) are successfully described within nonperturbative approaches [47–49], and other optical process are described by a plasmas perspective like high-order harmonic generation (HHG) [30,32].

1.1.2 High harmonic generation

McPherson *et al.* first observed high-order harmonic generation with gases in 1987 [50]. The high harmonics intensity decreases with increasing order at low orders, but then forms a plateau where the intensity remains comparable for many orders. Additional experiments with proper phase matching techniques observe the plateau to be extended over hundreds of electron volts into the soft X-ray regime [38–40]. This plateau ends abruptly at a position called the high harmonic cut-off which is related to the laser peak intensity [51,52]. In addition, the yield of harmonics is highly dependent on the polarization of the driving laser field [53], and drops dramatically with increasing ellipticity. The plateau in the HHG spectrum appears to be inconsistent with the perturbative theory, as higher order terms are smaller.

The nonperturbative mechanism of high harmonic generation is explained by a semi-classical model [30]. The model described the interaction between intense laser field with two

procedures: ionization of electrons using tunneling ionization model and evolution of the freed electron in the continuum using classical mechanics. With a third step, re-collision of the electron with its parental ion, this model is then known as three-step model or re-collision model, as shown in Fig. 1-1. The model successfully explains the intensity depend cut-off in the high harmonic spectrum. It also suggests that using higher intensity or longer wavelength laser can expand the high harmonic source to higher photon energy [38].

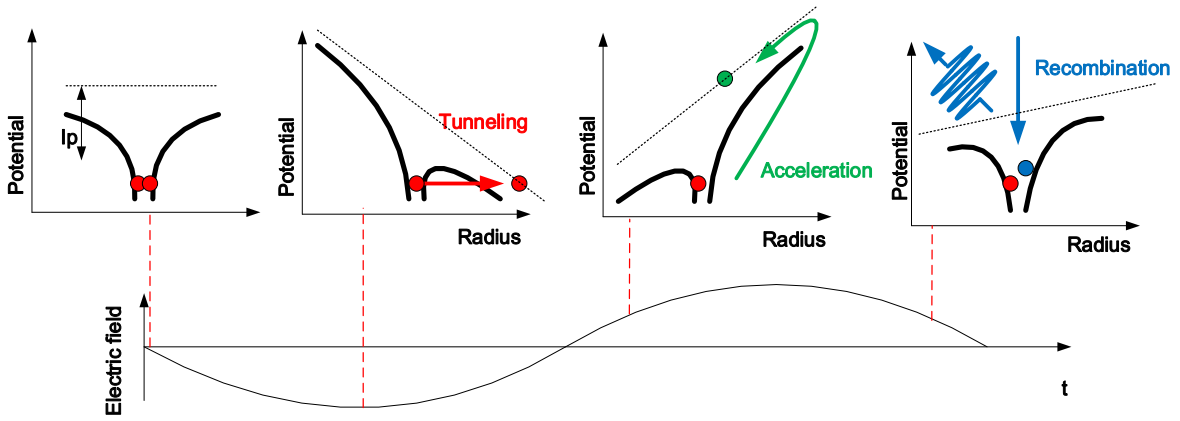

Fig. 1-1 Illustration of semi-classical three-step model of high harmonic generation. Tunneling: Intense infrared laser field tilts the Coulomb potential. Thus, the electron can tunnel out of the barrier. Acceleration: Freed electron is then accelerated by the driving field in the continuum and gain kinetic energy. Recombination: Electron recombines with parent ion and emit an energetic photon.

When the electron is accelerated in the presences of strong laser field, it can gain hundreds of electron volts of kinetic energy [32,38]. Upon recombining with its parent ion and decaying to a ground state, the system will release the excessive energy in the form of emitting a photon. The wavelength of this photon can be in the extreme ultraviolet or soft X-ray range, from tens of nanometers down to a few nanometers. The energy can potentially reach keV range by choosing the interaction medium and phase matching condition [40]. All of the electrons are synchronized with the driving laser field, so all emitters possess a phase relation to the driving laser field. This gives rise to the coherent nature of such light source.

1.1.3 Ultrafast laser technology

The development of nonlinear optics and ultrafast laser technology are tightly linked, since nonlinear interaction with matter favours a high instantaneous laser field and short time duration. However, obtaining intensities near 1 PW cm^{-2} or field strengths near 10^9 V/m is impractical with conventional electrical amplification schemes. Without considering the conversion efficiency, to create 1 PW cm^{-2} intensity on a 100 μm^2 area continuously for 10 minutes requires 60 TJ energy, which is the power consumption of Ontario for a day! Therefore, we can only create an electric field with high intensity for a short period of time.

For a pulsed laser, the intensity equals to the pulse energy per unit area per unit time; therefore, building a pulsed laser with high pulse energy and short duration becomes a feasible option.

By scaling up the size of the amplifying material and coherently combining multiple beams, recent development in the high power solid state laser allows for peak powers of petawatts at low sub-Hertz repetition rate and sub-picosecond duration [54] [55]. This provides an extreme experimental environment for scientific research, but its extremely large size and low repetition rate greatly limit its use in weak signal measurements and commercialization. To create a strong field environment on a tabletop, we need to further reduce the pulse duration.

There are different strategies for creating pulses with different durations. A mechanical shutter can gate an optical beam at millisecond opening time, while an opto-electrical modulator operates at tens of picosecond (hundreds of Gigahertz). To reach the femtosecond time scale, we must ask the light beam to gate itself. Again, the coherence of the laser beam plays a crucial role. The duration of the generated optical pulse is pushed to femtosecond by mode-locked laser technology.

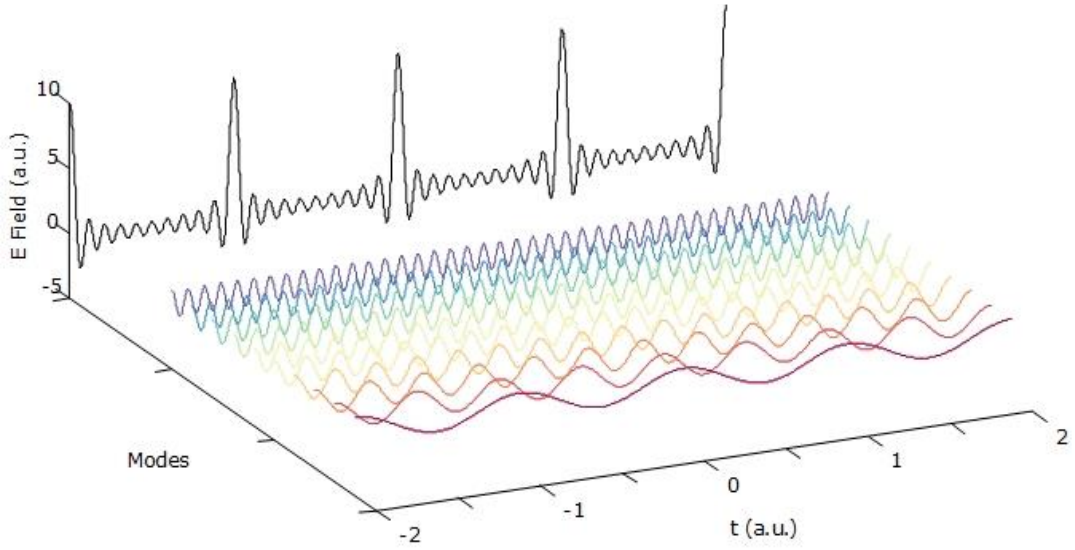

Fig. 1-2 Illustration of mode locking. Constructive interference of waves with difference colour forms a periodic short pulse shown in the black waveform. The pulse duration of the black waveform determined by the number of different frequency components and their phase synchronization.

The mode locking techniques create the femtosecond laser pulses by synchronizing the radiation at different frequencies. The sinusoidal functions in Fig. 1-2 represent monochromatic light waves. When the waves are all in phase at one instant in time, the fields add constructively and produce a narrow pulse. At other times, they destructively interfere. The duration of the pulse is determined by the bandwidth and phase of the spectrum. This shortest pulse duration supported by a bandwidth is called transform limited pulse duration. The current mainstream technology for producing femtosecond pulses is the Titanium

Sapphire (Ti:S) laser, which can simultaneously support radiation from 700-1000 nm. If all frequency components can be synchronized in phase, the output radiation can be compressed to tens of femtoseconds in pulse durations.

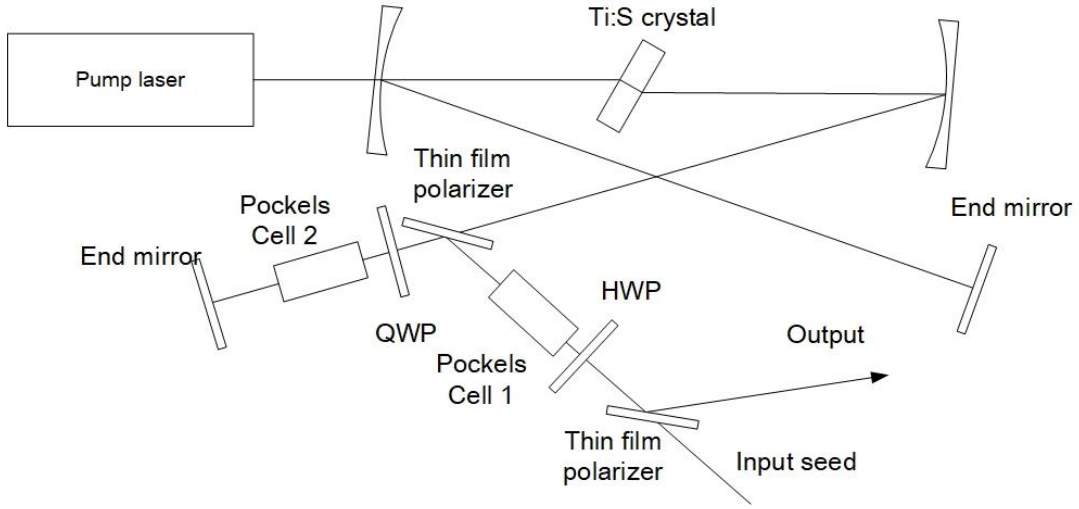

Fig. 1-3 Schematics of regenerative cavity. HWP: half-wave plate; QWP: quart-wave plate

Apart from reducing the pulse duration, increasing the output power is another way to achieve intense electromagnetic fields. Assuming a transform limited pulse duration around 30 fs from a Ti:S laser is focused to a 100 μm diameter focal spot, we would need 0.6 mJ pulse energy to achieve 0.2 PW cm^{-2}, the critical intensity for strong field interaction with noble gas. However, the typical pulse energy from above mentioned mode locked laser or oscillator is only a few nJ, which requires further optical amplification.

To build up stronger optical pulses, the seed pulses from a Ti:S optical oscillator are injected into a regenerative amplifier cavity where they pass through another Ti:S crystal multiple times before leaving the cavity. As shown in Fig. 1-3, the initial pulse is injected into the cavity through Pockles Cell 1 which is opened for a short time. After that, the pulse can undergo many round trips in the cavity. The radiation is enhanced each time the light goes through the amplification medium. Finally, the pulse is released from the resonator by flipping its polarization state using a second electro-optic switch (Pockles Cell 2), or the same one as used for injecting the initial pulse.

After passing through the gain medium recurrently, pulse energies are amplified to the millijoule level using a table-top amplifier, but higher energies require larger devices. A typical Ti:S regenerative amplifier can produce 30 fs pulses at a repetition rate of 1 kHz with an average output power of 1 W, or 1 mJ per pulse. This technology allows us to generate high harmonic from noble gases, but we need even higher power to obtain the flexibility to shape the beam.

Higher pulse energy allows more flexibility in shaping the spatial structure of the fundamental beam. However, we cannot amplify a pulse indefinitely by passing it through a crystal more

times. As the pulse energy gets higher, the pulses experience increasing nonlinearity. For example, self-focusing can occur inside the crystal and cause damage to the gain medium. This bottleneck of amplifying powerful optical pulses was overcome by Strickland and Mourou in 1985 with a technique called chirped pulse amplification [56]. The pulses are stretched in time (chirped) to reduce their peak power and nonlinearity inside the medium. Then the pulses are amplified to a higher energy without distorting their phase front. Finally, dispersive elements with opposite chirp compress the pulses back to their original duration. This technique is the standard for high-intensity laser systems and was awarded Nobel Prize in physics in 2018.

The high intensity laser system (Legend Elite Duo HE, Coherent, Inc.) with which we performed most experiments in this thesis uses both regenerative cavity technology and the chirped pulse amplification technique. The pulse energy can reach 10 mJ at 1kHz repetition rate after two-stage amplification. Such energy provides us the flexibility to shape the beam and keep the intensity above the critical intensity for high harmonic generation. The high laser power and short pulse duration initiate nonperturbative behaviour and introduce new physics and new opportunities to shape the XUV emission.

1.2 Structured beam generation

The generic spatial profile of a laser is a Gaussian mode. Most research in strong field laser physics concerns interactions with a Gaussian laser beam. This is because dispersion control and spatial filtering allow us to well-maintain and control the Gaussian profile, even when it propagates in a medium. However, we can control both the temporal and spatial shape of the pulse in the experiment, and these are interesting degrees of freedom to explore.

Numerous studies use Fourier transform pulse-shaping of femtosecond pulses in the temporal domain. In this technique, the pulse is first transformed into Fourier domain. Then, dispersive optical elements control the spectral phase. Carefully controlling the spectral phase over a broadband spectrum can compress infrared pulse to single cycle region. This ultrashort pulse infrared can generate an isolated attosecond pulse [57]. Extra chirp can be induced to elongate the pulse. For example, in the chirped pulse amplification, the pulses are chirped to avoid self-focusing while being amplified. Besides shortening and elongating the pulse, the femtosecond pulse can also be shaped to generate complex waveforms. The spectral phase and the amplitude are modified independently in the Fourier domain using a spatial light modulator [58–60]. This technique has been widely used in coherent control, biomedical imaging and optical communications [61–64].

Structuring the spatial profile of an optical pulse is another active research field. Complex spatial profiles enable many interesting phenomena that Gaussian optics cannot achieve. For example, optical tweezers and stimulated emission depletion microscopy both exploit the spatial properties of the optical beam. As a result, the interaction occurs in only part of the beam, and the dynamics are no longer uniformly distributed across the beam. This not only simplifies the experiment by making multiple measurements in one shot across the ensemble, but it also creates a tiny and complex experimental environment that can be about the size of wavelength. Such a micro-environment has been implemented in microfluid researches [65].

1.2.1 Liquid crystal phase plate

Liquid-crystal-based devices are a convenient and powerful tool to shape the spatial properties (e.g. polarization, phase front and intensity) of a laser beam. Due to the birefringence of a liquid crystal molecule, radiations with different polarizations will experience different phase delays after propagating through the device. The polarization and the phase front of electromagnetic radiation are entwined in many other ways than birefringence. For example, when the polarization of an electromagnetic wave undergoes a continuous sequence of transformations following a closed path in the space of polarization states on the Poincare sphere, the wave acquires a phase shift known as the Pancharatnam-Berry phase. This phase is also called geometric phase since it is determined only by the geometry of the polarization path [66–68].

By the same principle, if a wave is subjected to transversely inhomogeneous polarization transformations with a homogeneous initial and final polarization state, the associated inhomogeneous geometrical phases will induce an overall phase front shaping. For example, consider the case of circularly polarized light (left-handed in the following analysis) that is incident to a half-wave plate. The half-wave plate can be represented as $\mathrm{HWP}=\begin{pmatrix}1 & 0\\ 0 & -1\end{pmatrix}$ and the incident polarization is $\mathrm{LCP}=\frac{1}{\sqrt{2}}\begin{pmatrix}1\\ i\end{pmatrix}$, in the Jones matrix representation. To generalize the matrix representation of the HWP, a rotation matrix is left multiplied to the HWP matrix, as shown in Eq. (1.3), where α is the relative angle between the direction of the waveplate and the lab frame.

$$\begin{pmatrix}\cos\alpha & -\sin\alpha\\ \sin\alpha & \cos\alpha\end{pmatrix}\begin{pmatrix}1 & 0\\ 0 & -1\end{pmatrix}\begin{pmatrix}\cos\alpha & \sin\alpha\\ -\sin\alpha & \cos\alpha\end{pmatrix}=\begin{pmatrix}\cos 2\alpha & \sin 2\alpha\\ \sin 2\alpha & -\cos 2\alpha\end{pmatrix} \tag{1.3}$$

Assuming a circularly polarized laser beam is incident on this wave plate, the Jones representation of the output is

$$\begin{pmatrix}\cos 2\alpha & \sin 2\alpha\\ \sin 2\alpha & -\cos 2\alpha\end{pmatrix}\frac{1}{\sqrt{2}}\begin{pmatrix}1\\ i\end{pmatrix}=\frac{1}{\sqrt{2}}\begin{pmatrix}\cos 2\alpha+i\sin 2\alpha\\ \sin 2\alpha-i\cos 2\alpha\end{pmatrix}=\frac{1}{\sqrt{2}}\exp\left(i2\alpha\right)\begin{pmatrix}1\\ -i\end{pmatrix}. \tag{1.4}$$

In Eq. (1.4), a left circularly polarized beam is converted into a right circularly polarized beam. In addition, an α-dependent phase is imposed uniformly.

Instead rotating a single waveplate, we use a special phase plate whose birefringence is position-dependence. In this case, the angle α is a function of spatial coordinate $\alpha(x,y)$. Therefore, the uniformed phase term $\exp(i2\alpha)$ becomes a position dependent term $\exp(i2\alpha(x,y))$ in the output beam representation, as shown in Eq. (1.5).

$$\begin{pmatrix}\cos 2\alpha(x,y) & \sin 2\alpha(x,y)\\ \sin 2\alpha(x,y) & -\cos 2\alpha(x,y)\end{pmatrix}\frac{1}{\sqrt{2}}\begin{pmatrix}1\\ i\end{pmatrix}=\frac{1}{\sqrt{2}}\exp\left(i2\alpha(x,y)\right)\begin{pmatrix}1\\ -i\end{pmatrix} \tag{1.5}$$

This approach is different from conventional optics like lenses or wedges, as they introduce optical path length differences to different parts of a beam. This approach only imposes pure phase to shape the wave front of a laser beam. In terms of ultrafast laser pulses, it changes the carrier envelope phase of a laser beam instead of delaying it. Therefore, it is suitable for broadband and ultrafast optics applications.

To engineer this position-dependent birefringent plate, researchers chose liquid crystals as the birefringent medium. The advancement of display technologies enables pixel-by-pixel control of the optical property of liquid crystal molecules. The pattern of the liquid crystal plate can be either premade or actively controlled during its operation. To modify the orientation of the liquid crystal molecules, a linearly polarized ultraviolet laser (405 nm) is illuminated onto the sample (Fig. 1-4). A digital micromirror device (DMD) in the imaging plane controls the beam shape on the sample, while a half-wave plate controls its polarization. The ultraviolet laser will make cells within polymer layer along the direction of the laser field where the beam illuminates. After the polymer cells have been made, the liquid crystal is injected between the two substrates and the liquid crystal molecules align along the direction of the polymer cells [69].

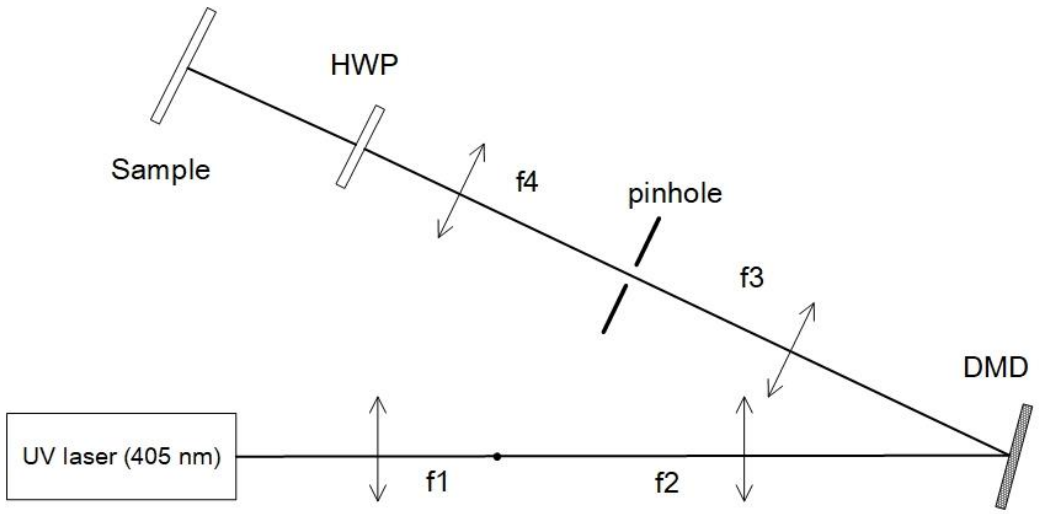

Fig. 1-4 Liquid-crystal phase plate fabrication apparatus. A 405 nm linearly polarized light beam is rotated and enlarged by going through a cylindrical 4-f system (*f*1 and *f*2). The beam then interacts with the digital micromirror device (DMD) programmed to reflect a specific light intensity pattern. The reflected beam goes through another 4-*f* system (*f*3 and *f*4) and an iris in order to select only its brightest diffraction orders as a means to clearly image the pattern onto the sample. The polarization of the beam is then adjusted by a half-wave plate (HWP) to the required orientation. After this rotation, the resulting beam aligns a specific region of the sample's photo-alignment layer.

Alternatively, spatial light modulators are commercially-available devices that perform similar transformations to the laser beam through a holographic approach [70–72]. Like

standard holography, the interference pattern between a reference beam and a target beam (a hologram) is created on the spatial light modulator. When this spatial light modulator is illuminated by a laser beam with plane wave front, the diffracted beam reproduces the same wave front as the target beam. However, the diffraction is wavelength-dependent and may cause the light to diffract into different directions, especially when the pulse is short and its bandwidth is large [73,74]. This limits the complexity of the shaping we can implement in broadband pulses using this approach. In contrast, a liquid crystal phase plate works mainly in a transmission mode and does not rely on the diffraction, which is beneficial for ultrafast pulse applications.

1.2.2 *q*-plates and vortex beams

A specially patterned plate called *q*-plate, whose phase front retardation is a function of the azimuthal angle, arouses great interest in quantum optics research. Its helical wave front retardation is associated with orbital angular momentum of light [75]. After passing a Gaussian beam through the *q*-plate, the output beam possesses a helical wave front and donut beam shape [76]. The most commonly used spatial mode carrying orbital angular momentum is the Laguerre Gaussian (LG) mode.

As a new type of beam that is different from Gaussian plane waves, the vortex beam is undergoing intense study in both classical and quantum optics research. Its exotic topology and quantum behaviours are of particular interest: A Mobius strip-like polarization is observed in the tightly focused vortex laser beam. Even more complex knots and structures are discovered [77–80]. These twisted photons can also be entangled in the dimension of angular momentum [81,82] and form high-dimensional quantum encryption, which benefits the noise tolerance [83,84] in quantum key distribution.

As an application of vortex beams, researchers encoded different information in channels formed by orthogonal spatial modes and achieved terabit-per-second high speed optical communications [85–87]. The spatial mode is an additional degree of freedom that increases the capacity of free-space communications. Different Laguerre-Gaussian modes act as different channels when transmitting signals, as they are orthogonal to each other. The OAM multiplexing is also independent to polarization and wavelength multiplexing, so they may be used simultaneously. Using high-dimensional multiplexing forms more advanced modulation scheme and improves the bandwidth efficiency in communications.

Bandwidth becomes a main challenge when communicating with objects in outer space, so this advanced modulation scheme particularly benefits communication with satellites and aircrafts. However, Laguerre-Gaussian modes at longer wavelength diffract faster and degrades the detection of vortex photons. Moving towards shorter wavelength with less diffraction provides an option for overcoming such problem. In addition, the higher energy of a single photon may also benefit to simplify the detection system, since the noise is much weaker for detecting radiation at shorter wavelength.

Vortex beams are also used to overcome the diffraction limit. In 1994, Hell and Wichmann developed stimulated emission depletion microscopy, which was experimentally demonstrated in 1999 by Hell and Klar [88,89]. It creates super-resolution images by

exploiting the nonlinearity in deactivating fluorophores using vortex beams. The sample is first excited by a Gaussian beam to pump the carriers to the excited state. Then a vortex beam, which possesses a dark hole in its centre, depletes the excited carriers through stimulated emission. Since the centre region is not exposed to the deactivation beam, the carriers stay in the excited state. After relaxation, these carriers will decay to the ground state and emit fluorescence from the centre region. Through this nonlinear excitation/depletion process, the size of the non-exposed centre becomes smaller than the achievable resolution for an optical system. The modified resolution is determined by

$$D = \frac{\lambda}{2NA\sqrt{1+\frac{I}{I_{\text{sat}}}}}\ , \tag{1.6}$$

where D is the transverse resolution, λ is the wavelength of the depletion light, I is the intensity of the depletion light and I_{sat} is saturation intensity. The resolution is dependant on both intensity and wavelength of the depletion light. The resolution can be improved by increasing the intensity of the deactivation beam to deplete more carriers, but this is limited by damage to the sample. Besides increasing the intensity, the spatial resolution can reach sub-nanometer levels when this technique is applied with much shorter wavelengths like XUV or soft-x ray. With solid-state samples, XUV beams are able to resolve nanostructures [90–92] and distinguish magnetic material [93]. The imaging power of XUV may be extended to the imaging of biological samples in the future. The work presented Chapter 3 intends to develop a light source for this potential imaging application by creating vortex beam with controllable wave fronts.

1.2.3 Polarization structured beam and generation

Apart from controlling the phase front of laser beams, the polarization can also be controlled and structured. Instead of uniformed polarization across the transverse mode, as shown in Fig. 1-5 (a), the polarization of the laser beam can be a function of spatial coordinates. Two widely studied polarization structured modes are radially polarized and azimuthally polarized modes, as shown in Fig. 1-5(b). Since their amplitudes need to be represented in a vector form, these beams with inhomogeneous polarization are often referred as vector beams.

One way to generate vector beam is to coherently combine two orthogonally polarized laser beams with different wave fronts. For example, radially polarized or azimuthally polarized laser beam can be decomposed into a Laguerre Gaussian $LG_{1,0}$ mode beam with a left circularly polarized beam and a Laguerre Gaussian $LG_{-1,0}$ mode beam with a right circularly polarized beam [94,95], where the first index is the azimuthal index l and the second index is the radial index p. Varying the relative phase between these two beams can switch the polarization from a radial one to an azimuthal one.

Radial and azimuthal beams can be decomposed in the linearly polarized basis in addition to the circularly polarized basis. For example, superimposing two orthogonal linearly polarized Hermit-Gaussian $HG_{0,1}$ and $HG_{1,0}$ modes can construct radially/azimuthally polarized beam [94,96], where the first index is the horizontal index m and the second index is the radial index n. The two polarization decompositions have different advantages when implementing

experiments or illuminating the mechanisms: The linearly polarized states can be directly distinguished and experimentally measured by optical elements like Brewster's angle or wire grid polarizers at relatively high intensity. The circular basis, on the other hand, are the eigenstates of the spin angular momentum operator, which is convenient in analysing the conversion of the angular momentum in nonlinear processes. Therefore, there is flexibility in the choice of polarization basis to suit the application.

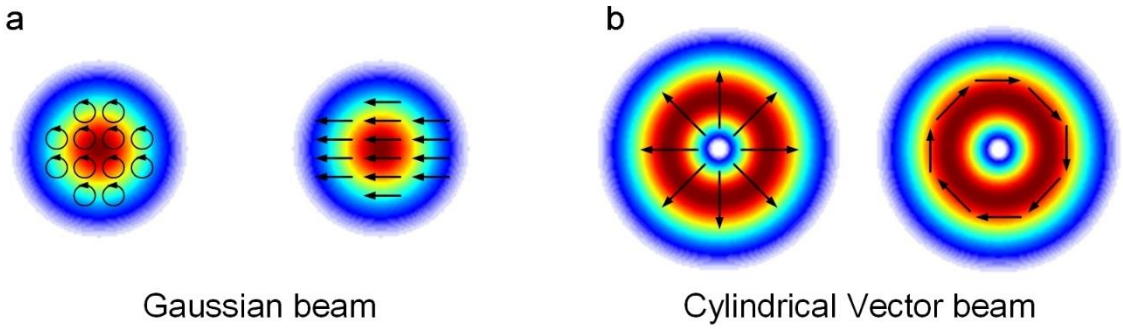

Fig. 1-5 Polarization profile of normal Gaussian beam and cylindrical vector beam (a) Polarization distribution of conventional Gaussian beam. left: circularly polarized Gaussian beam; right: linearly polarized Gaussian beam. (b) Polarization distribution of vector beams. Left: radially polarized beam; right: azimuthally polarized beam.

The radially polarized beam intrinsically gives a better match to the solution of light field emitted from single atom and therefore can be focused to an even smaller spot than focusing a uniformly polarized light [97,98]. This leads to several important implications of using vector beams to achieve better spatial resolution in optical microscopy, optical trapping and laser machining [99–104]. If such beam is tightly focused, the radially polarized electric field in the transverse plane will constructively interfere in the transverse direction, which gives rise to a longitudinal electric field at the beam centre [105]. Such fields are used to accelerate particles to relativistic speeds over a short distance [106,107]. When focusing such a beam on materials, the orientation of the polarization can be transferred to both metal and dielectric surfaces. The mechanism is explained in a plasma-formation perspective. More complex polarizations or patterns can be imparted onto surfaces with a polarization shaping technique based on liquid crystal devices [108,109] .

As a result of the cylindrical symmetry, radially or azimuthally polarized modes are also eigenmodes of propagation in a cylindrically symmetric waveguide. Therefore, they are suitable for use in the generation of ultrashort pulses with currently available high-power pulse compression technology based on a gas-filled hollow-core capillary. The pulse can maintain its properties after nonlinear interaction and spectral broadening, which extends its interesting spatial characteristics to few-cycle pulses [110]. For example, the radial (azimuthal) mode is a superposition of two Laguerre-Gaussian modes with opposite spin states. Such non-separable states are maintained after the spectrum is broadened and the pulse is compressed down to few-cycle duration. This is studied experimentally and discussed in Chapter 6 in details.

Similar to phase front shaping, liquid crystal-based devices are convenient for preparing vector beams. Besides superimposing two beams with different wave fronts, the

radial/azimuthal beam can be generated by a linearly polarized beam that is incident on a *q*-plate. The liquid crystal molecules serve as micro half-wave plate and shape the local polarization as they are oriented [95,111]. Therefore, the polarizations of a light beam can be shaped almost “at will” and “point by point” across its transverse profile.

The polarization structures can be more exotic than linearly polarizations at different orientations. The structure can consist polarizations with any ellipticity. In an extreme case, beams containing all possible polarizations on a Poincare sphere are called full Poincare beams [112]. Hybrid beams are another interesting example of beams with complex structure, as they have polarizations that evolve while the beams propagate [113]. In this way, the polarization of a beam can be engineered not only in the transverse direction, but also along its propagation direction. A study of using this characteristic in high harmonic generation is presented in Chapter 5.

1.3 Structured beams in strong field physics

Once both high-harmonic based XUV generation and beam shaping techniques became available, many researchers began using structured beams in high harmonic generation to study the behaviour of structured photons in this highly nonlinear process. In 2012, Zürch et al. published their results of high harmonics produced with a phase vortex beam [114], and showed that the generated high harmonics preserve the singular topology from its fundamental driving beam. A further study by Gariepy et al., carefully examined the wave front structure by interfering the high harmonics, and argued that orbital angular momentum is preserved in this nonperturbative nonlinear process [74]. This result was then confirmed by measuring the divergence of high harmonics [115]. Another interesting discussion regarding the conservation of orbital angular momentum in high harmonic generation involves a special type of beam possessing a non-integer topological charge. The results suggest that the expectation value of the orbital angular momentum is still conserved [116,117], and the generated beams are superpositions of different eigenmodes.

To better control the orbital angular momentum, we added a control beam to optically manipulate the generation process. This approach can be understood in an optical holographic manner, or by the mixing of orbital angular momentum. This allows arbitrary orbital angular momentum to be transferred to any XUV wavelength, instead of the harmonic order determining the OAM [118]. Similar wave front control is demonstrated in a laser induced plasma hologram at an even higher laser intensity [119]. In such a scheme, a controlled pre-pulse is used to structure the plasma surface instead of directly using a structured beam to generate XUV.

Besides the orbital angular momentum and the phase structure, there is great interest in the dynamics of spin angular momentum in high harmonic generation. It not only concerns the conservation law of spin angular momentum, but also relates to the polarization control of XUV light. Efficient generation of circularly polarized XUV light still remains a challenge in both scientific and industrial applications. Under a slightly different context, generating circularly polarized XUV beams is primarily studied by mixing two laser beams with counter-rotating polarization states [120–122]. Then the circularly polarized XUV beams are used in probing the chiral response of the magnetic materials [123].

It is worth noting that the distinction between structured beams and combining multiple beams becomes blurry, especially when multiple beams are created coherently. The multiple-beam configuration can be seen as a special case of structured beams, even from each beam's perspective, the mode is considered uniform and unstructured. On the other hand, shaping the spatial profile of a laser beam has much more flexibility than combining two laser beams: both the polarization and phase can be designed pixel-by-pixel at micrometer precision. Due to being nearly colinear and the flexibility in patterning structures, a single structured beam has the potential to improve the phase matching while producing polarization-controlled XUV radiation and even extending the highest photon energy.

The ability to structure XUV beams is one prominent feature of coherence that high harmonics inherit from the driving field. The coherence also guarantees the phase relation between XUV radiation and the fundamental driving field. This relation gives us access to control the XUV emission phase by controlling the infrared. In comparison, large-scale synchrotron sources can only provide partial coherence [124] by spatial filtering, which limits its applications in diffraction analysis of nonperiodic structures and complex biological samples [125]. Phase-sensitive measurements at XUV wavelength are possible with high-harmonic sources by controlling the phase delay of either the XUV pulse or the fundamental infrared pulses.

Engineering both wave front and polarization will also impact industry applications in addition to scientific research. With fast establishment of EUV lithography manufacturing lines, industrial integrated circuit (IC) demands XUV light to interrogate fast switching at the nanoscale. The diffraction limit of conventional diagnostic tool using visible and UV light is becoming a main challenge for non-invasively characterizing the smaller chips being made. Mirrorless imaging becomes a feasible option for XUV imaging since it does not require physical imaging element to perform transformations. Since the post-process reconstruction algorithm relies on the coherence of the illumination, coherent high harmonic sources play an important and competitive role. Structuring the fundamental photon create an extra degree of freedom to further explore in strong field experiments. The all-optical control of phase fronts and polarization enables us to create XUV photons with complex properties that allow us to make faster and more advanced measurements.

Chapter 2 Methodology: Controlling high harmonics with fundamental fields

Controlling the polarization or phase profile of the fundamental beam generating high harmonics in experiments enables us to shape the spatial structure of the generated XUV radiation and to study the physics of the interaction of spatially structured beams with matter. Two general approaches are used to control the spatial properties of XUV beams: (i) using XUV optics to modify the XUV radiation after being generated or (ii) optically manipulating the XUV generation process and directly generating structured XUV radiation. This thesis follows the second approach, which requires understanding and controlling the high harmonic generation process. Based on a semiclassical model [30], this chapter presents analysis on how the XUV emission phase is influenced by controlling the spatial structure of the fundamental beam.

The first method of shaping XUV beams is similar to how we shape the infrared and visible beams. The XUV beam is initially generated with unstructured spatial properties. By using XUV/X-ray optics, the beam is modified to have the desired spatial profile. In broadband applications (e.g. high harmonic generation, attosecond pulses), reflective optics are more desirable, since reflective optics are more suited for broadband applications. These optics often use the incident grazing angle to increase the reflection efficiency. For example, reflecting from concave or toroidal multilayer mirrors can impose concave phase front curvatures to XUV beams and focus beams of a given wavelength [126,127]. Besides reflective optics, diffractive optics also play an important role in shaping beams at extremely short wavelengths. Zone plates use concentric ring structures used to create constructive interreferences at certain distance to focus XUV beams or to image nanostructures [5]. This can be extended to more complex beam shaping by using specially designed diffractive patterns. However, to control the phase or polarization, all these methods require sub-wavelength manufacturing precision, which ranges from nanometer to sub-nanometer precision for XUV wavelengths.

In the second method, the focus of the fundamental beam is spatially modulated using a structured infrared fundamental or perturbing beam. The XUV beams generated from this modulated focus are spatially structured during the generation process. This method does not rely on high quality XUV optics and structures the XUV beam entirely optically. Distinct from the first method, this method requires that the XUV emission possesses a deterministic relation to its generation process or the driving laser field. Therefore, the XUV generation methods that depend on spontaneous emissions or incoherent process cannot apply this “on site” manipulation.

Built on high harmonic generation, a coherent process, we modify the phase front of the driving field to control the phase structure of high harmonic radiation. This chapter discusses how the emission phase of XUV radiation is influenced by the modified laser field. In the experiment, we use a weak perturbing beam to interfere with the fundamental beam, so that the total field can be controlled by varying the phase and amplitude of the perturbing beam. Since the atoms are dilute in gas phase, we only consider the single-atom response with a

semi-classical model driven by these modified fields. The single-atom response, when perturbed by a weak field, is studied, and we see that the modulated phase of the fundamental is extended to phase modulations in the generated high harmonic beams.

2.1 Semiclassical model of high harmonic generation

For a noble gas atom interacting with a strong laser field, if the field intensity is on the order of or greater than 10^{14} W cm^{-2}, the field strength near the peak of each oscillation is comparable, to or greater than, that of the atomic Coulomb field that binds the electrons to the atom. Due to the high field strength, the potential well confining the electron is weakened and becomes a barrier, allowing the electron to tunnel into the continuum. The tunnelling rate is given by [30,128]

$$W_{dc} = \omega_s \left|C_{n^*l^*}\right|^2 G_{lm} \left(\frac{4\omega_s}{\omega_t}\right)^{2n^*-m-1} \exp\left(-\frac{4\omega_s}{3\omega_t}\right), \tag{2.1}$$

where $\omega_s = \frac{I_p}{\hbar}$, $\omega_t = \frac{eE_{dc}}{\sqrt{2m_e I_p}}$, $G_{lm} = \frac{(2l+1)(l+|m|)!\left(2^{-|m|}\right)}{|m|!(l-\|m\|)!}$, $n^* = \sqrt{\frac{I_p^H}{I_p}}$,

$\left|C_{n^*l^*}\right| = 2^{2n^*\left[n^*\Gamma(n^*+l^*+1)\Gamma(n^*-l^*)\right]^{-1}}$, I_p is the ionization potential, I_p^H is the ionization potential of the hydrogen. E_{dc} is the external field, m_e is the electron mass, e is the electron charge, m, l are the magnetic and azimuthal quantum number, l^* is the equivalent quantum number given by $l^* = 0$ for $l \ll n$ and $l^* = n^*-1$ otherwise, and Γ is the Gamma function.

The time-dependent tunnelling rate is approximated by using the tunnelling rate in response to a DC field of the same field strength and assuming it changes adiabatically with time as the field changes. This tunnelling rate is highly nonlinear and is primarily related to the external field exponentially. The wave perspective of the external field dominates the ionization step when a large number of photons are involved.

Then, the portion of the electron wave packet in the continuum moves in response to the driving laser field like a classical charged particle, and its classical trajectory can be calculated by Newton's second law:

$$\frac{d^2x}{dt^2} = -\frac{eE}{m_e}\cos(\omega t) \tag{2.2}$$

$$x = \frac{eE}{m_e\omega^2}\left\{\left[\cos(\omega t_r) - \cos(\omega t_b)\right] + \omega\sin(\omega t_b)(t_r - t_b)\right\}, \tag{2.3}$$

where x is the displacement of freed electron in x direction; E is the peak field strength; ω is the angular frequency of the driving laser field, t_b and t_r are the tunnelling time (commonly known as the 'time of birth') and recombination time.

Similarly, for the y direction,

$$\frac{d^2y}{dt^2} = -\varepsilon \frac{eE}{m_e} \sin(\omega t) \tag{2.4}$$

$$y = \varepsilon \frac{eE}{m_e \omega^2} \left\{ \left[\sin(\omega t_r) - \sin(\omega t_b) \right] - \omega \sin(\omega t_b)(t_r - t_b) \right\}, \tag{2.5}$$

where ε is the ellipticity of the driving laser field.

The tunnelling process is considered instantaneous and the initial velocity and position of the tunneled electron are assumed to be zero [129,130]. When considering linearly polarized driving fields (ε = 0), the freed electron is driven only by the *x*-component of the field and, consequently, the electron displacement and velocity along orthogonal directions is zero. We plot the electron displacement trajectory for a tunneling time between $\omega t = 0.05\times 2\pi$ and $\omega t = 0.25\times 2\pi$ in Fig. 2-1. The electron is first driven away from its parent ion in the first half cycle of the laser field and is then driven back when the laser field changes sign and, consequently, its direction. During the propagation step, the electron is accelerated by the laser field and acquires kinetic energy throughout its trajectory. Finally, the electron recombines with the parent ion and emits its excess energy upon re-entering the ground state through the emission of a photon. The photon energy, according to the conservation of energy, is equal to the sum of the ionization potential of the atom and the acquired kinetic energy of the electron.

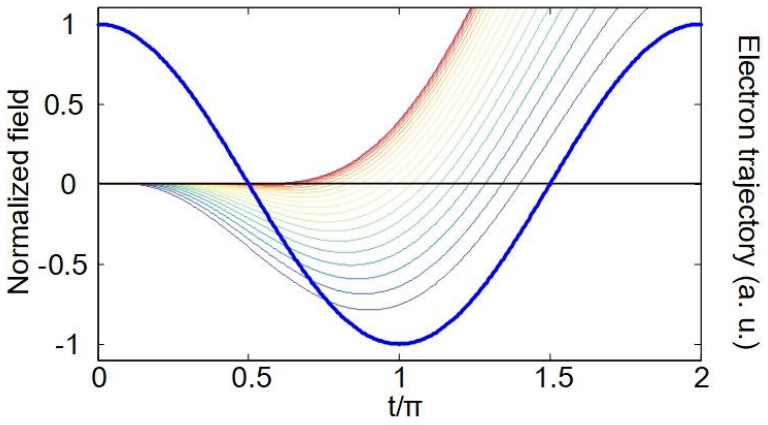

Fig. 2-1 The displacement trajectories for the electron which is tunnelled tunneled between $\omega t = 0.05\times 2\pi$ and $\omega t = 0.25\times 2\pi$. The thick blue line shows the waveform of the laser field. The colours of the trajectories represent different kinetic energies gained by the electron.

The maximum returning electron energy corresponds to a time of birth of $\omega t = 0.05\times 2\pi$ and time of return of $\omega t = 0.7\times 2\pi$ (purple line in Fig. 2-1). The energy of this photon is given by

$$\begin{aligned} \hbar\Omega &= I_p + 3.17 \frac{eE^2}{4m_e\omega^2}, \\ &= I_p + 3.17U_p \end{aligned} \tag{2.6}$$

where U_p is the ponderomotive potential. (U_p corresponds to the time averaged kinetic energy of the electron wave packet in the presence of the external laser field.) This kinetic energy is inversely proportional to the angular frequency of the driving laser field. Thus, for a given field strength, the maximum generated photon energy can be increased by increasing the driving laser wavelength. This is an intuitive result, as, for a given laser intensity, longer wavelength driving fields keep the electron in the continuum longer and, consequently, accelerate the electron for a longer time.

The wave packets are released near the peaks of each half cycle when the field is strong and, consequently, the XUV photons are generated every half period of the fundamental field. Additionally, the electric field changes sign each half cycle, which accelerates the electron wave packet in an opposite direction than the previous half-cycle. This gives rise to a π phase shift between two adjacent generated XUV pulses. In the Fourier domain, the half cycle periodicity leads to a 2ω separation between the generated harmonics and the π phase shift between adjacent pulses offsets the starting frequency from 0 to ω. This is why only discreate odd orders of harmonics are observed in a typical high harmonic generation process when using multi-cycle pulses.

In Fig. 2-1, each electron trajectory corresponds to a tunnelling time t_b, a recombination time t_r, and a photon energy $\hbar\Omega$. The emission phase of the photon is related to the ionization time, the phase that electron wave packet accumulates during the excursion, and the recombination of the electron re-entering the ground state with its parent ion. Therefore, the emission phase carries information about both the system from which the electron originated and the external field which accelerates the electron in the continuum. Decoding this information with the emission phase of different harmonic orders has been used in molecular orbital tomography, enabling the probing of atomic or molecular structure and to observe changes in said structure during chemical reactions [6,131].

Since electrons with different kinetic energies return at different times, XUV pulses generated in this way exhibit an intrinsic chirp, which has become known as the atto-chirp [132,133]. Additionally, there are two windows of time in which the same returning electron energy spectrum is observed. The first window, for electrons released between 0 to $\omega t = 0.05\times 2\pi$ of the laser cycle, gives rise to a negative chirp. The second window, for electrons released between $\omega t = 0.05\times 2\pi$ to $\omega t = 0.25\times 2\pi$, exhibits a positive chirp. These two windows of time intrinsically partition XUV emission into two subsets. For the first window, these electrons spend a greater time in the continuum than those released in the second window and, consequently, the harmonics associated with these trajectories are known as long trajectories. For the second window, the time spent in continuum is less than those from the first window and, appropriately, these trajectories are known as short trajectories. Due to the intensity dependent phase and resultant wave front curvature of the generated harmonics, the long trajectories photons are much more divergent in space and optimal phase matching conditions for generating macroscopic beams are much more stringent than those for short trajectories. Consequently, macroscopic high harmonic beams are typically dominated by short trajectory emissions. As a result, both simulation and experiments shown in this thesis only consider the contribution from the short trajectories.

2.2 Perturbation by a coherent external field

As it can be seen from the Eq. (2.3), the electron trajectory is a function of the driving laser field. If we can modify the instantaneous field strength, we can alter the trajectories of the electrons during their excursion.

To achieve control of the driving field, we introduce an external field which has a controlled phase relation to the driving laser field of the generation process. The interference of these two fields modifies the field in space and time.

If the high harmonic generation process is perturbed by a weak perturbing field $\tilde{E}_p(t) = E_p\cos(\omega_p t+\Delta\varphi)$, which is added to the intense driving field $\tilde{E}_d(t) = E_d\cos(\omega_d t)$, the electron trajectories described in Eq. (2.3) are modified accordingly. Consequently, the phase accrued during the electron's trajectory is modified and, as a result, the emitted phase of the high harmonic radiation is also modified. Here, E_d and E_p are field amplitudes, and ω_p and ω_d are frequencies of the perturbing and driving beams respectively. The harmonic phase modulation due to the perturbing laser field is predominantly present during the electron trajectory in the continuum [133].

The phase of the emitted high harmonic photon at frequency Ω associated with the electron excursion in the continuum can be obtain by

$$\Phi_{\text{amp}}(\Omega) = \int_{t_b}^{t_r} \frac{1}{\hbar}\left[\frac{\left(p - e\mathbf{A}\right)^2}{2m_e} + I_p\right] - \Omega dt \ , \tag{2.7}$$

where t_b, t_r, p are the birth time, the recombination time and the canonical momentum of a specific electron wave packet trajectory corresponding to harmonic order q at frequency Ω. A is the vector potential of the driving laser fields. The first two terms correspond to the electron phase accumulated during the electron acceleration and the third term corresponds to the global phase at the recombination time in terms of frequency Ω. Here we can see that the XUV phase is related to both the electron trajectory and the birth and recombination times. However, the recombination time of the electron is a function of the vector potential, which is highly nonlinear and has no analytical form.

If a weak perturbing field is added, with the same frequency as the driving field, $\omega_p = \omega_d = \omega$, the total laser field retains its cosine function form, but with modified amplitude and phase, which is induced by the interference between the perturbing field and driving field. Then the electron trajectories described in Eq. (2.7) will be modified accordingly.

In order to show the underlying physics of this phase shift, we break the phase estimation into two parts: (i) the phase modification due to changes of the electron trajectory caused by amplitude variation of the total laser field; (ii) the phase modification due to change of recombination time due to the phase variation of the driving field.

The change of action caused by amplitude variation can be evaluated by

$$\begin{aligned}\Delta\Phi_{\text{amp}}(\Omega) &= \int_{t_b}^{t_r} -\frac{e(p-A)}{\hbar m_e} dA dt \\ &= \int_{t_b}^{t_r} -\frac{e(p-A)A_p}{\hbar m_e} dt\end{aligned} , \tag{2.8}$$

where A_p is the vector potential of the perturbing laser field. For each harmonic order, t_b, t_r, p are obtained from solving Eq. (2.3) without considering the perturbing field.

If the pulse duration is much longer than one period of an optical cycle, the phase shift can be evaluated without considering the carrier-envelope phase effect by

$$\Delta\Phi_{\text{amp}}(\Omega) = \int_{t_b}^{t_r} -\frac{eE_p}{\omega^2\hbar m_e} E_d \left[\sin(\omega t_b) - \sin(\omega t)\right] \sin(\omega t + \Delta\varphi) dt \ , \tag{2.9}$$

where E_d, E_p are the peak field strength of the driving and perturbing laser field, and $\Delta\varphi$ is the phase difference between the driving and perturbing laser fields. The phase integral is evaluated with the same times of birth and recombination, as the additional field is treated as a weak perturbation. Consequently, a greater phase shift will be observed for longer excursion times.

Apart from the phase term induced by amplitude variation, a perturbing field of same colour will also shift the total driving field. The total field can be written as

$$\begin{aligned}&E_{total}\cos\left(\omega t + \Delta\Phi_{ph}(\omega)\right) \\ &= E_p\cos(\omega t + \Delta\varphi) + E_d\cos(\omega t) \\ &= \sqrt{E_p^2 + E_d^2 + 2\cos\Delta\phi E_p E_e}\cos\left(\omega t + \arctan\frac{\frac{E_p}{E_d}\sin\Delta\phi}{1+\frac{E_p}{E_d}\cos\Delta\phi}\right)\end{aligned} . \tag{2.10}$$

The phase shift for the qth harmonics at frequency Ω, influenced by the phase variation of the driving field, can be obtained by

$$\begin{aligned}\Delta\Phi_{\text{ph}}(\Omega) &= \frac{\Omega}{\omega}\arctan\frac{\frac{E_p}{E_d}\sin\Delta\phi}{1+\frac{E_p}{E_d}\cos\Delta\phi} \ , \\ &= q\arctan\frac{r\sin\Delta\phi}{1+r\cos\Delta\phi}\end{aligned} \tag{2.11}$$

where r is the relative amplitude ratio between the perturbing and driving laser field.

As can be seem from the expression in Eq. (2.11), when the modulation depth r is small, the phase modulation induced by time frame shift can be approximated by

$$\lim_{r\to 0} \Delta\Phi_{\mathrm{ph}}(\Omega) = qr\sin\Delta\phi \ , \tag{2.12}$$

which has a $\pi/2$ phase shift relative to the amplitude variation.

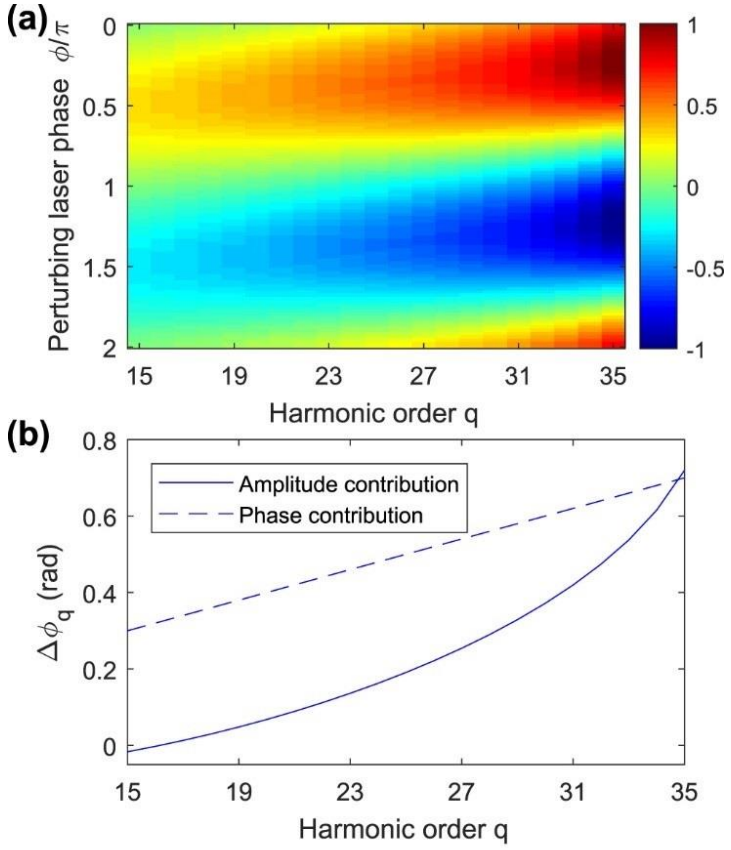

Fig. 2-2. Theoretical analysis of high harmonic phase modulation. (a) semi-classical calculation of the phase shift (color) as a function of the harmonic order q and the perturbing laser phase φ. The relative perturbing laser amplitude r = 0.02. (b) The high harmonic phase modulations contributed by the total driving field amplitude variation (solid line) and phase variation (dashed line).

The total phase modulation as a function of perturbing laser phase, $\Delta\Phi_q$, is calculated for short trajectories and qth order harmonic, as shown in Fig. 2-2 (a). In this calculation, the relative amplitude ratio between perturbing and driving laser field is r = 0.02. For a given harmonic order, q, the relation between the harmonic phase shift $\Delta\Omega q$ and the perturbing laser phase shift can be fitted by a cosine function $\Delta\Phi(\Omega) = C_q\cos(\Delta\phi-\psi_q)$.The C_q parameter encodes the modulation depth of the harmonic phase, and ψ_q encodes the delay of the harmonic phase modulation relative to the perturbing laser field. For low harmonic orders (e.g. for the parameters of our experiment, q<25), $\psi_q \approx \pi/2$ and the harmonic phase modulation is in phase with the total driving field phase variation. This result implies that, although the electron wave packet trajectories for low harmonic orders are modified by the perturbing field, the

modifications are negligible compared to the phase modulation because of the total driving field phase variation. For harmonic orders close to the cut-off frequency (e.g. q = 33), $\psi_q \approx 0.24\pi$ and the harmonic phase tends to synchronize with the total driving field amplitude variation. Changes in the phase accrued during the electron propagation induced by the amplitude variation of the total driving field becomes important for harmonic orders near the cut-off. The actual delay, ψ_q, between the harmonic phase modulation and the perturbing laser phase is determined by the interplay between the amplitude and phase variations of the total driving field and falls into the range between 0 and $\pi/2$.

To illustrate the coupled effect of these two mechanisms, phase shifts of the harmonics are estimated separately for contribution due to variations in the driving field amplitude and phase. The contribution from amplitude variation can be calculated by setting $\Delta\varphi = 0$ for the perturbing field in equation (2.9) (Fig. 2-2 (b), solid line). In the perturbation case, the maximum induced harmonic phase modulation equals q arcsin(dE/E) = q arcsin(r) and is plotted by the dashed line in Fig. 1(b). For low harmonics (e.g. q = 15 or 17) the harmonic phase shift is close to zero and is significantly smaller than that contributed by the driving field phase variation. However, the contribution from amplitude variations increases rapidly with the harmonic order, and the two parts becomes comparable for harmonics close to the cut-off.

The above calculation for harmonic phase modulation is based on the semi-classical model, and only takes the phase modulation contribution in the electron acceleration step into account. Simulation results and discussion by solving the time dependent Schrödinger equation (TDSE) about these phase modulation mechanisms can be found in [134]. The results found therein are consistent with the semi-classical calculation except near the cut-off region. Thus, the ionization and recombination steps have negligible effect on the harmonic phase modulation compared to the electron propagation step. These results also suggest that the harmonic phase modulation scheme is mostly independent of the nonlinear medium.

2.3 Measuring the emission phase shift

To complement the analysis above, an experimental *in situ* reconstruction of emitted phase is performed by interfering a weak perturbing laser beam and a strong driving laser beam with the same color (Fig. 2-3(a)).

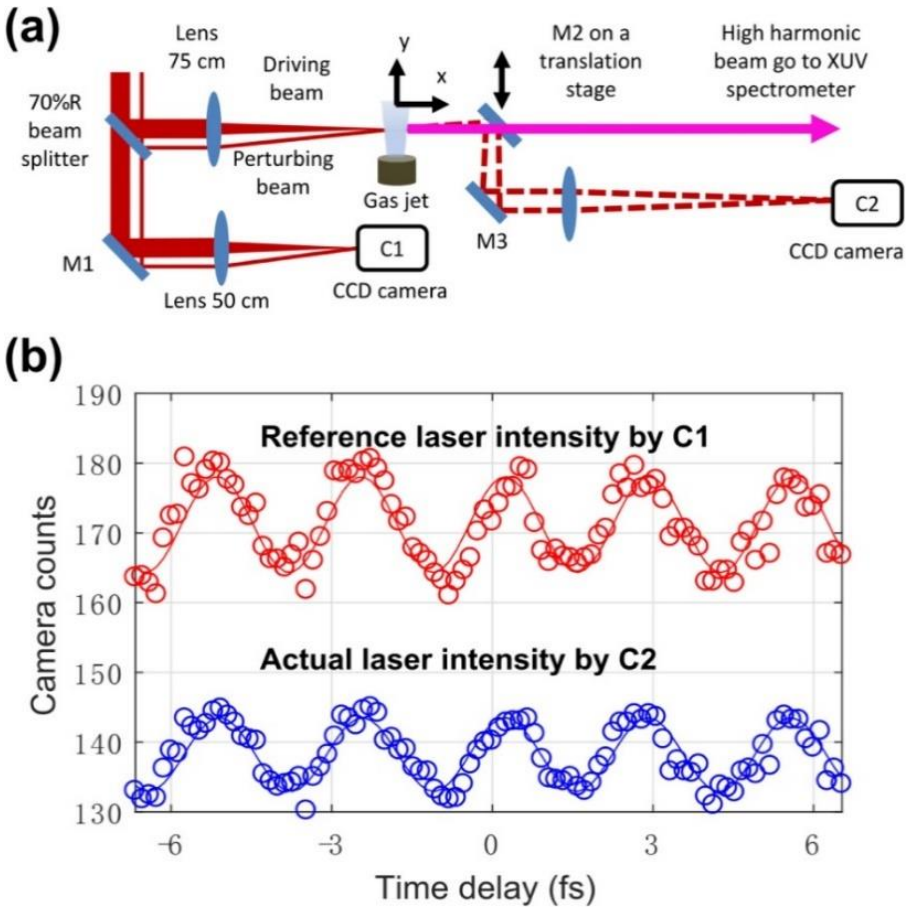

Fig. 2-3. Experimental setup for measuring phase variations of fundamental and high harmonic beams. (a) Schematic diagram of the experimental setup. The temporal delay of the driving laser beam (thick red lines) is controlled by a piezo-stage relative to the perturbing laser beam (thin red lines). M1–3 are uncoated silica plates providing 4% reflection for the laser beams at 45° incident angle. M2 is on a motorized stage. Used for calibration, it can be moved out of the high harmonic beam path in actual experiments. (b) The camera counts captured by the reference camera C1 (red) and the calibration camera C2 (blue) respectively. Measured data are labeled with circles, and the fitted sine functions are plotted with solid lines.

The relative amplitude, r, and phase, $\Delta\psi$, are measured using a replicated reference beam pair. In Fig. 2-3(a), a 70%-reflective beam splitter transmits a portion of the of the harmonic generating-perturbing pulse pair (30% of the total energy) and the camera C1 captures the interference with the reference at the focal spot. Experimentally, the mirror M2 is off-set from the XUV beam line and the high harmonic beam is monitored with an XUV spectrometer. Thus, the frequency-resolved far field profiles of the high harmonic beam and interference of the reference laser beam pair on the camera C1 are recorded simultaneously. In order to determine the perturbing laser phase and relative amplitude from the camera C1 interference data, a separate calibration procedure is done, wherein the steering mirror M2 is moved in the high harmonic generation chamber, camera C2 is used to record the interference between the

fundamental and perturbing beams, and the observed pattern is compared with the reference beam pair interference data from the camera C1.

Figure 2-3 (b) shows the C1 and C2 camera counts for the centers of the copied reference and the real focal spot at the gas target. We obtain $\Delta\varphi$ by fitting the intensity signal to a cosine function. The relative field amplitude r can be extracted from the amplitude of the AC oscillation component and the averaged camera count signal, or the DC component.

There are two main sources of systematic uncertainty in determining $\Delta\varphi$. One is the thermal or nonlinear Kerr phase effect caused by the optics. We minimize this contribution by using a 4% reflection surface from a silica plate for mirrors M1, M2, and M3, as shown in Fig. xx(a). The other source of uncertainty is the depth of field of the imaging system from the gas target to the camera C2. We minimize this source by mounting a knife-edge as a reference object at the gas nozzle and optimizing the position of the camera C2 by overlapping the images of the reference object illuminated by the driving and the perturbing beams respectively. Experimentally we observe visible degradation of the knife-edge image on the camera C2 if the knife edge is moved 0.5 mm longitudinally along the x-direction. It corresponds to ~0.06π uncertainty of $\Delta\varphi$.

As shown in Fig. 2-3 (a), the perturbing laser beam (wavelength $\lambda_p = 2\pi c/\omega_p$ = 800 nm) crossed the intense driving beam (wavelength $\lambda_d = \lambda_p$ = 800 nm, pulse duration 40 fs) at the gas jet at an angle of α = 15 mrad. The oblique angle geometry introduced a linear perturbing phase shift between the driving and perturbing fields. We tune $\Delta\varphi$ with a piezo-controlled translation stage on the driving beam arm. Thus, the qth harmonic wave front has a cosine function shaped phase modulation $\Delta\Phi(\Omega)=C_q\cos(\Delta\phi-\psi_q)$ along the y-direction and at this small angle it changes the high harmonic beam pointing and the far field divergence. By scanning $\Delta\varphi$, the oscillation of the harmonic beam pointing, and divergence reveal the harmonic phase modulation [135]. Figure 2-4 (a) shows the measured far field spectrogram of 19^{th} harmonics with different temporal delay between the driving and perturbing fields.

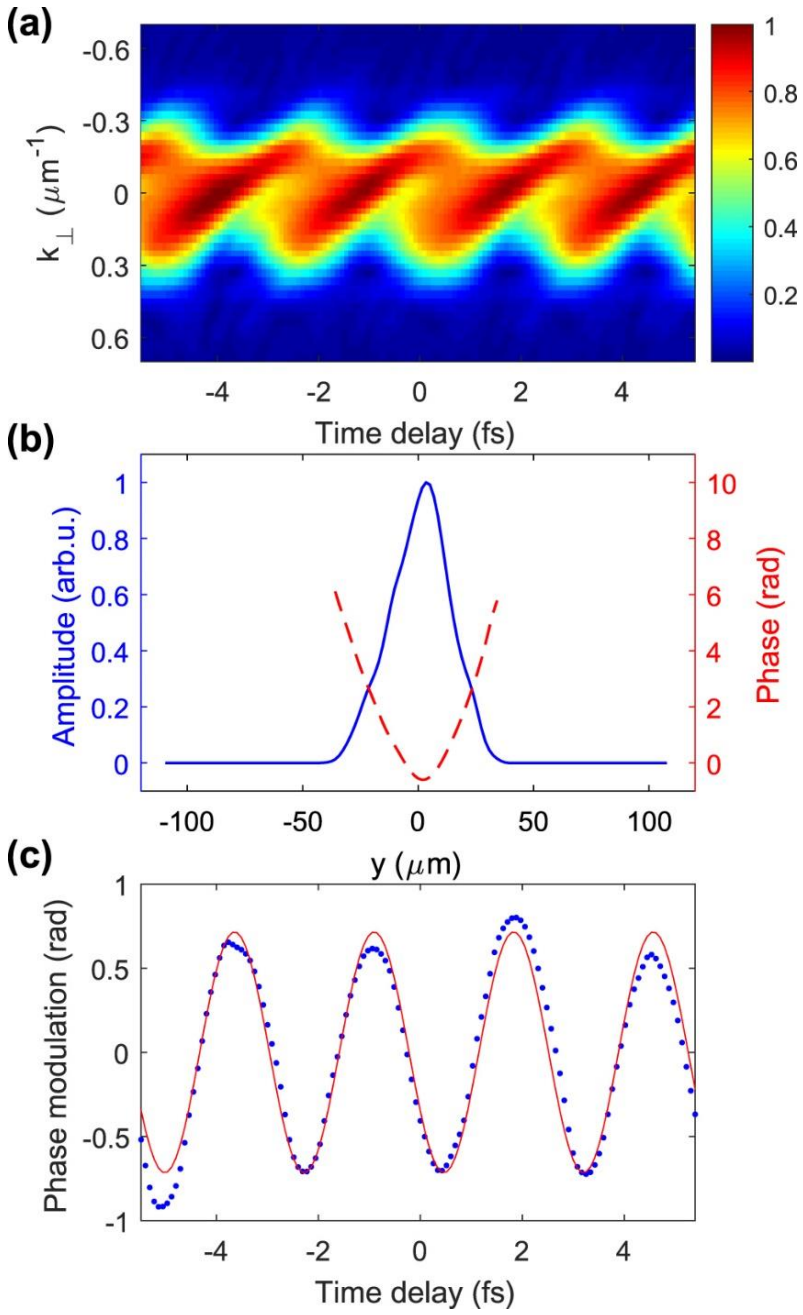

Fig. 2-4. Reconstruction of the high harmonic phase modulation for H19. (a) The measured far field spectrogram with different temporal delay between the driving and perturbing fields. (b) The reconstructed near field electrical profile of the H19 beam. The solid line for amplitude and the dashed line for phase. (c) The reconstructed phase modulation of the H19 beam at y = 0 with different temporal delay between the driving and perturbing fields (blue dotted line) and its sine function fitting (red solid line).

Propagating back to the near field, or the position at focus, the phase structure can be obtained in Fig. 2-4 (b), shown in red dashed curve with its intensity profile shown in blue solid line.

Considering the phase shift only at the position $y = 0$, the phase shift of the harmonics $\Delta\Phi(\Omega)$ with respect to the relative phase between the perturbing and driving laser field $\Delta\varphi$ is shown (blue dotted line) and fitted with a cosine function (red solid line) in Fig. 2-4 (c). The fitting cosine function is $\Delta\Phi(\Omega) = C_q\cos(\Delta\phi - \psi_q)$.

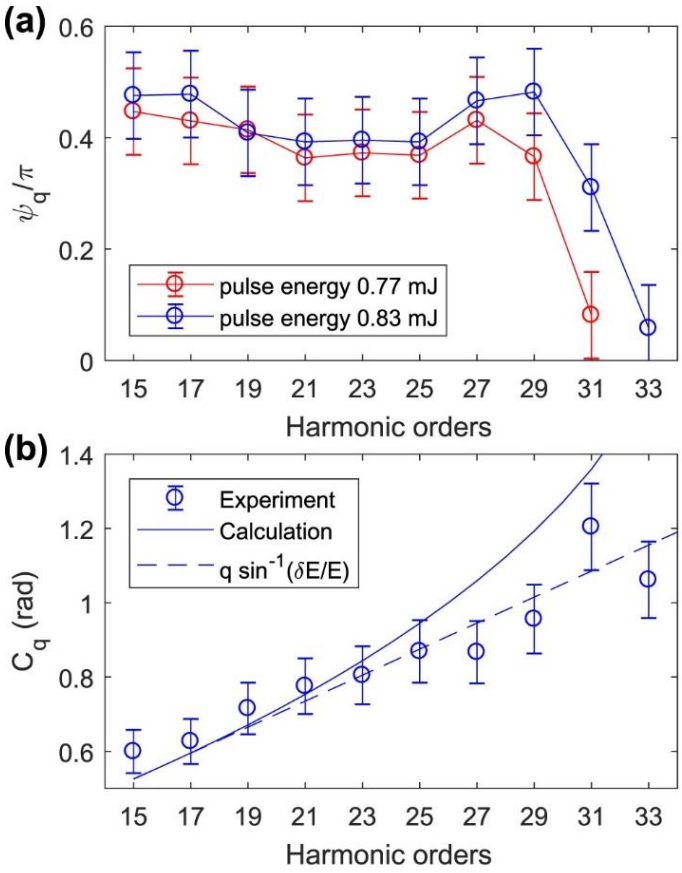

Fig. 2-5 High harmonic phase modulation delay ψ_q and depth C_q in argon. (a) The harmonic modulation delay ψ_q as a function of the harmonic order q. The driving laser pulse energy is 0.83 mJ (blue) and 0.77 mJ (red). (b) The harmonic modulation depth C_q as a function of the harmonic order q. The experimental results are shown in circles, the saddle point calculation results in the solid line, and the dash line shows the function $q$arcsin ($\delta E/E$). In (a) and (b), the relative perturbing field amplitude is $\delta E/E = 0.035$.

By fitting the curves in Fig. 2-4 (c), we can estimate the relative delay ψ_q between the harmonic phase modulation and the perturbing laser field. This relative delay is between 0 and $\pi/2$, since both the phase and amplitude of the driving laser field will contribute to the phase shift of the high harmonics. The value indicates the contributions of phase and amplitude induced phase shift.

The maximum phase modulations for different harmonic orders generated from argon gas are plotted in Fig. 2-5 (a). For low harmonic orders ($q \leq 25$), the relative delay ψ_q is around (0.50

± 0.13)π, consistent with the theoretical analysis above. It means that the high harmonic phase modulation for low orders is predominantly determined by the phase variation of the total driving laser field. For harmonic orders close to the cut-off (q = 33 for 0.83 mJ pulse energy in blue and q = 31 for 0.77 mJ in red), the parameter ψ_q decreases to ~0.1π. As discussed above, it is because the amplitude induced phase becomes important compared to the phase induced part. For harmonic orders around q = 27 or 29, an increase of ψ_q is observed that was not found in the previous theoretical analysis. This observation arises because it is experimentally difficult to suppress the long trajectory contributions near the cut-off, which were omitted in the theoretical analysis. However, at the cut-off, the long and short trajectories merge and the analysis based on the short trajectory assumption becomes available again. In addition, for both 0.83 and 0.77 mJ driving laser pulse energy, the dependence of ψ_q on the harmonic order q behaves the same, implying that the relative importance between the driving field amplitude and phase variation only depend on whether the harmonic order is close to the cut-off or not.

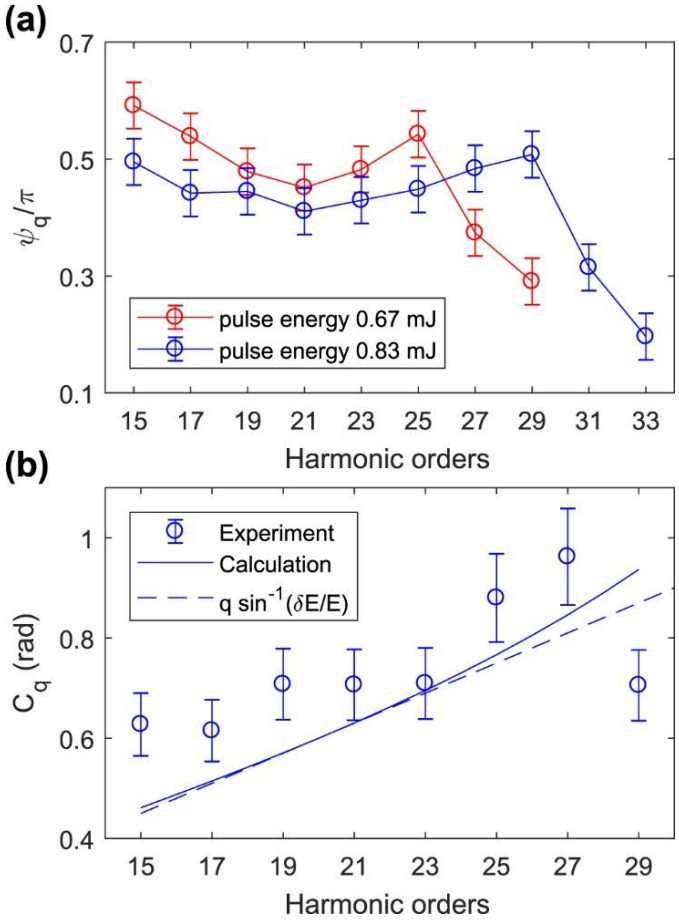

Fig. 2-6. High harmonic phase modulation delay ψ_q and depth C_q in neon. (a) The harmonic modulation delay ψ_q as a function of the harmonic order q. The driving laser pulse energy is 0.83 mJ (blue) and 0.67 mJ (red). (b) The harmonic modulation depth C_q as a function of the harmonic order q. The experimental result is shown in circles, the saddle point calculation result in the solid line, and the dash line shows the function $q$arcsin ($\delta E/E$). The relative perturbing field amplitude is $\delta E/E$ = 0.030.

A similar measurement is performed using neon gas as the nonlinear medium, to study the dependence of the high harmonic phase modulation on the nonlinear gas medium. As shown in the theoretical analysis, the ionization phase and the recombination phase contributions to the harmonic phase modulation are negligible compared to the electron propagation phase, thus the experimental results with neon about the harmonic phase modulation depth C_q and delay ψ_q in Fig. 2-6 are similar to those results with argon in Fig. 2-5. As shown in Fig. 2-6 (a), low harmonic orders below the cut-off energy generated in neon follow a $\pi/2$ delay relative to the perturbing field, whereas the delay for higher order harmonics drops as they approach the cut-off. In Fig. 2-6 (b), the measured modulation depth C_q (circles) is also close to the saddle point calculation with I_p = 21.56 eV for neon (solid line). Note that the driving field phase variation induced modulation depth q arcsin ($\delta E/E$) can also reasonably predict the measured harmonic phase modulation depth, and it is independent of the gas type.

2.4 Implications

We study the relationship between the driving laser phase and the XUV high harmonic phase, which reveal the origin of the dipole phase shift in the strong field interaction. The observed modulation is primarily attributable to the propagation of the freed electron, which corresponds to the second step in the semiclassical model. The phase shift is transferred from the fundamental beam through the modification of the electron trajectories. Since the displacement of electron trajectory is small compare to the separation between the gas atoms, the influence of the adjacent atoms is negligible and is omitted. However, the phase shift is different for harmonics generated from crystals where the electronic band structure of the generation medium needs to be taken into account [136]. Therefore, measuring the emission phase of the high harmonic beams may provide a platform for high-harmonic spectroscopy of solids.

The link between the spatial phase profiles of the fundamental and high harmonic beams generated in a gas also suggests a spatial light modulator (SLM) for XUV high harmonic radiation. High harmonic radiation is focused and delivered by various XUV or X-ray optics for nonlinear optics or imaging applications. However, such optics (and even the extremely nonlinear high harmonic generation process itself) introduces aberrations to the wave front, leading to imperfect spatial beam profiles. In this case, a weak perturbing laser beam can be spatially modulated by an ordinary near infrared or visible SLM, and the modulated perturbing field overlaps with an intense driving field at the nonlinear medium. Thus, the perturbing field wave front pattern can be directly imprinted onto the generated high harmonic wave front to pre-compensate the aberration [137]. Moreover, with the feedback from *ex situ* wave front characterizations, the *in situ* driving-perturbing wave front control scheme would be able to work in a closed loop, allowing for the possibility of highly controlled and versatile structured wave fronts for high harmonic radiation.

Besides correcting the aberration of high harmonic beams, the phase control of the fundamental beam gives us access to shape the emitted phase profiles of the high-order harmonics. The relation we discussed in this chapter provides an estimation of the phase shift which can be transferred from the fundamental beam to the high harmonics. By using the beam-shaping techniques (e.g. spatial light modulators, deformable mirrors) for infrared

beam, we can shape the spatial phase and amplitude of fundamental driving or perturbing laser beam at micrometer precision. Then using these structured laser beam to produce high harmonics enables us to shape the XUV photon into more advanced structures, such as the Fresnel pattern for focusing and defocusing beams [138] and spiral wave front for beams carrying orbital angular momentum [74,118,139].

Chapter 3 High harmonic generation with phase structured beams

Light beams which have spiral wave fronts carry orbital angular momentum (OAM). These beams can be flexibly produced and measured with infrared and visible light. Their application is an important research topic for super-resolution imaging, optical communications and quantum optics. However, only a few methods can produce OAM beams in the extreme ultraviolet or X-ray. Controlling the OAM on these beams remains challenging.

In this chapter I demonstrate a tabletop source that can generate XUV beams carrying orbital angular momentum. By applying wave mixing to a tabletop high-harmonic source, we can imprint arbitrary topological charge (OAM value) on to XUV beams. The generation process is driven by a Gaussian infrared laser beam that is perturbed by a weak beam of the same colour that carries OAM. A *q*-plate [76] imprints OAM onto the perturbing IR beam through geometric phase. Our technique enables us to produce first-order OAM beams with the smallest possible central intensity null at XUV wavelengths. By varying the input polarization of the perturbing beam, we control the OAM of the diffracted radiation, enabling us to switch the OAM of high-harmonic beams.

We also developed an interferometric method to measure the topological charge of high harmonic XUV beams. For a reference we use a separate and highly divergent coherent source. The interference between the reference and the OAM beams determines the spiral wave fronts of XUV beams.

This experiment provides a crucial step towards applications of structured XUV beams. Vortex beams at XUV wavelength can provide high spatial resolution as compared to the visible and infrared beams. These vortex beams can be focused down to nanometer scale [5] and they open a route for carrier-injected laser machining and lithography to reach the stimulated emission depletion (STED) microscopy-like super resolution, which we will discuss in the application part of this chapter. The XUV vortex beams we create in this experiment open a route for carrier-injected laser machining and lithography, which may reach nanometer or even Ångström resolution. The photon energy of these beams is from tens to hundreds of electron volts, which gives access to directly interact inner shell electrons with structured photons. Such a light source is also ideal for space communications, both in the classical and quantum regimes.

3.1 Extreme ultraviolet vortex beams

Optical vortices [75] have become an important research topic with extensive applications in particle trapping [140], super-resolution imaging [88], optical communications [86] and quantum optics. Such vortex beams can be flexibly produced, measured and manipulated with infrared and visible light. For example, stimulated emission depletion (STED) microscopy overcomes the Abbe diffraction limit by using the dark centre of the first-order optical vortex beam with a helical wave front characterized by $e^{il\varphi}$, where l is the topological charge. The resolution of STED microscopy can reach $\lambda/100$ when visible light is used [141], where λ is

the wavelength of the pump beam. Structured light sources at shorter wavelengths open a route to increasing the resolution still further.

However, previous methods [74,114,115] of producing short wavelength vortex beam via high harmonic generation placed topological charge on the fundamental beam. According to the conservation of orbital angular momentum, the topological charge of the fundamental is multiplied by the harmonic order during harmonic generation. Therefore, previous experiments fail to produce high harmonics with low-order OAM.

In addition, the phase distortion on the fundamental beam is transferred to the harmonics through high harmonic generation process. These imperfections become even more severe on the higher orders whose wavelength are shorter. It can make the phase front measurement difficult. In contrast, our method controls the wave front based on a perturbative approach, which has relative higher tolerance to aberrations.

In addition to using a perturbative control approach, we also use an advanced liquid crystal technique to generate vortex beams with fewer defects. Unlike other diffractive devices, *q*-plate works in a transmission mode and therefore does not create spatial chirp for broadband pulses [142].

Furthermore, for the detuned wavelengths, the phase is only imparted in one circularly polarized state not the other, as shown in Eq. (3.1) [143,144].

$$\begin{pmatrix} \cos\alpha & -\sin\alpha \\ \sin\alpha & \cos\alpha \end{pmatrix}\begin{pmatrix} 1 & 0 \\ 0 & e^{i\delta} \end{pmatrix}\begin{pmatrix} \cos\alpha & \sin\alpha \\ -\sin\alpha & \cos\alpha \end{pmatrix}\frac{1}{\sqrt{2}}\begin{pmatrix} 1 \\ +i \end{pmatrix} = \frac{1}{\sqrt{2}}e^{\frac{i\delta}{2}}\left[\cos\frac{\delta}{2}\begin{pmatrix} 1 \\ i \end{pmatrix} + i\sin\frac{\delta}{2}e^{i2\alpha}\begin{pmatrix} 1 \\ -i \end{pmatrix}\right], \tag{3.1}$$

where δ is the optical retardation after passing through liquid crystal plate.

A circularly polarized beam transmits through a central wavelength detuned phase plate. The output consists of two parts: 1) a counter-rotating circularly polarized beam with extra phase and 2) a same circularly polarized beam with no extra phase. Therefore, using *q*-plates in preparing the pulsed laser beams eliminates the mode contamination caused by dispersion when we select a single polarization.

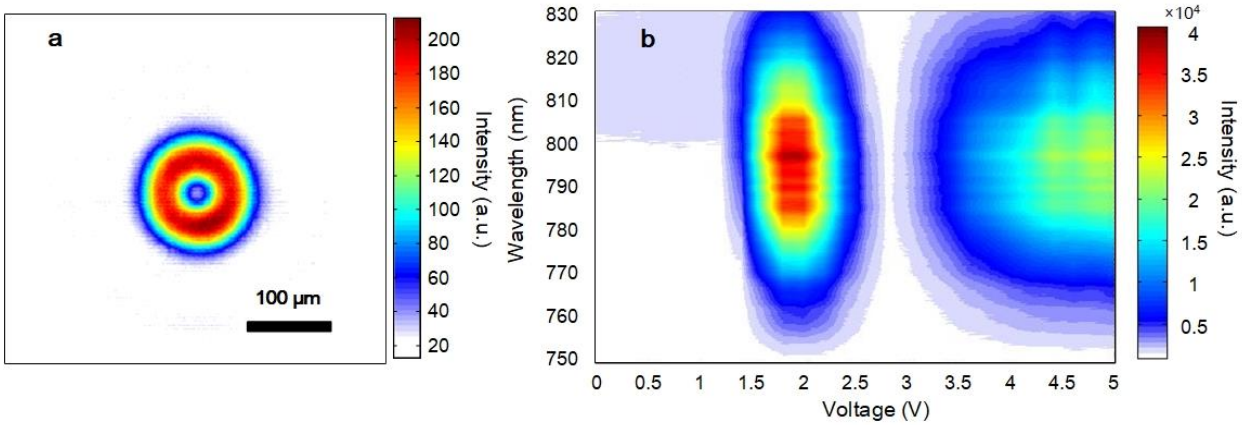

Fig. 3-1 The laser mode after passing through *q*-plate. (a) The transverse mode of a Gaussian beam after passing through a *q*-plate and being focused by a 50 cm lens. (b) The transmitted spectrum of a *q*-plate with different bias voltages. When the voltage is below 1.5 V the effective thickness does not change and almost no light can flip its polarization. When the bias voltage is set to be 1.8 V, the whole spectrum can be converted from left circularly polarized state to right circularly polarized state.

3.2 Controlling orbital angular momentum using ultrahigh order wave mixing

The driving field in the experiment is created by interfering two beams. Fig. 3-2 illustrates the experimental arrangement used to generate high-harmonic beams with OAM. A linearly polarized 800-nm infrared Gaussian beam, pulse duration of 30 fs, and energy of 500 μJ, is focused to an intensity of 2×10^{14} W cm^{-2} by a 40 cm lens in a noble-gas medium. Another weaker beam with the same polarization and the same colour is given one unit of OAM by passing it through a *q*-plate. The weak vortex beam has 50 fs pulse duration and 250 μJ energy and is focused by a 20 cm lens to an intensity of ~2×10^{12} W cm^{-2}. These two beams overlap in both time and space in the nonlinear medium at a relative angle of 40 mrad. The strong Gaussian beam drives the high-harmonic generation, while the weak vortex beam controls the process.

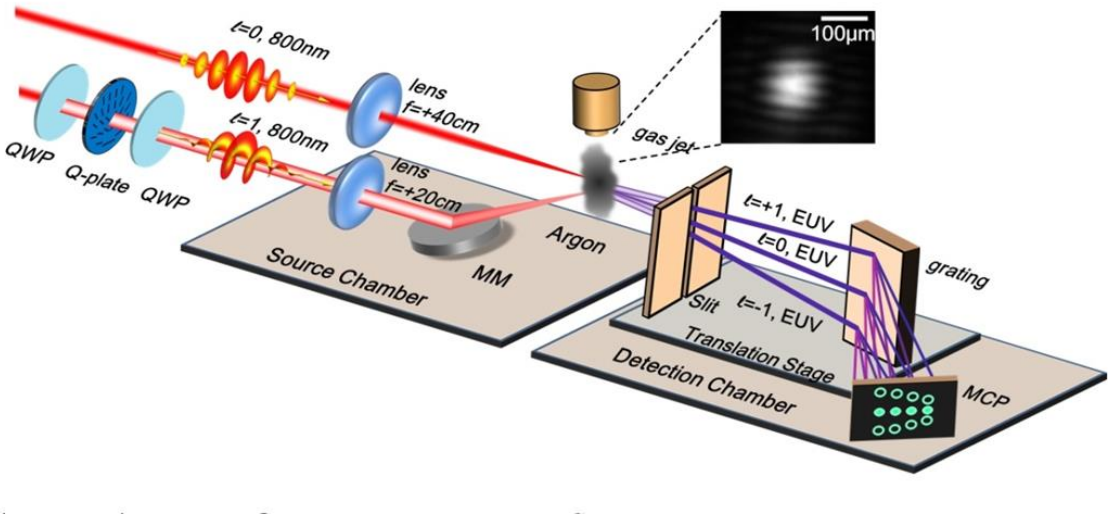

Fig. 3-2 Experimental setup for generating XUV beams with arbitrary OAM. A strong infrared laser beam is overlapped with a weak infrared vortex beam in the argon-gas interaction medium. Their interference creates an intensity and phase distribution with a forked structure in the gas medium. The distribution is transferred to the phase of the emitting dipoles. The produced XUV is diffracted by this forked-grating structure. The three diffracted high-harmonic XUV beamlets that are produced carry +1, 0 and -1 units of OAM. The XUV beams are spectrally resolved in a detection chamber and detected by a micro-channel plate. The slit and the grating can be translated together to reconstruct the beam profile. QWP: quarter wave plate; MCP: micro-channel plate; MM: motorized mirror. Inset: the interference pattern between the Gaussian driving beam and the vortex beam at the focal plane. This distribution induces the fork-shaped phase grating of the emitting dipole.

Argon gas is used as the nonlinear medium. We use a thin noble-gas medium to minimize propagation effects [145]. The gas is injected through a 200 μm nozzle into the vacuum chamber via a synchronized Even Lavie gas jet at a 500 Hz repetition rate. The backing pressure in the chamber reaches 10^{-4} mbar.

The centre wavelength of the *q*-plate is tuned to 800 nm and the *q*-plate is designed to give the transmitted beam a topological charge of one. The two non-collinear beams overlap in both time and space. Their 40 mrad relative angle ensures that the diffracted XUV beams are also spatially separated. Since the OAM of a light depends on the axis of the beam, a motorized mirror ensures good spatial overlap of the two beam centres.

The two infrared beams are both linearly polarized and interfere in the gas medium, as shown in Fig. 3-2. Since the weak vortex beam has a helical wave front, the overlapping IR beams form a fork-shaped electric field distribution. In contrast to the model with second harmonic perturbation [74], by using the same colour wave mixing scheme, we form a static holographic pattern in both its intensity and phase. Such a fork-shaped distribution imprinted on the driving field alters the electron trajectories, which consequently modifies the phase of the dipole emission. This distribution induces a weak grating-like spatial phase variation in the emitting dipoles, thereby causing the XUV beam to diffract in the vertical direction. The first-order diffracted beams should carry the same OAM as the perturbing beam. This prediction is based

on the semi-classical model of high-harmonic generation in the strong-field limit [30] and can be understood qualitatively. The phase modulations appear directly on the XUV beam, while the amplitude modulation is transferred to phase through the influence of amplitude changes to the re-collision electron phase and therefore to the induced dipole that is emitted [133].

To detect and characterize the generated XUV radiation, the harmonic beam propagates to a spectrometer in a differentially pumped detection chamber. The spectrometer consists of a slit, a grating and a micro-channel plate. The slit and grating are translated together to reconstruct the beam profiles of the high harmonics. The beams are then spectrally resolved in the horizontal direction by an 87-degree grazing-incidence grating with 1200 lines/mm, and are then detected by a micro-channel plate. A camera records the fluorescent screen at the back of the micro-channel plate. On the spectrogram, different positions along the horizontal direction correspond to different photon energies, or alternatively, to the order of the harmonics. We move the slit and the diffraction grating together to reconstruct the spatial profile of each harmonic.

We use the semiclassical model introduced in Chapter 2 to simulate the high harmonic generation process. Since the gas medium is only 200 μm thick, we simulate the generation process with emitters in a single plane, without propagation effects. Each emitter is driven by the local time-dependent electric field created by the interference of the strong Gaussian beam and the weak vortex beam. The strong field approximation dipole moment in 2D is calculated pointwise at the focal plane. It is then decomposed in the Fourier domain to obtain near-field emission of each harmonic order, as shown in Fig. 3-3. The far-field Fraunhofer diffraction image is obtained by performing 2D Fourier transformation, which simulate the free space propagation in the spectrometer.

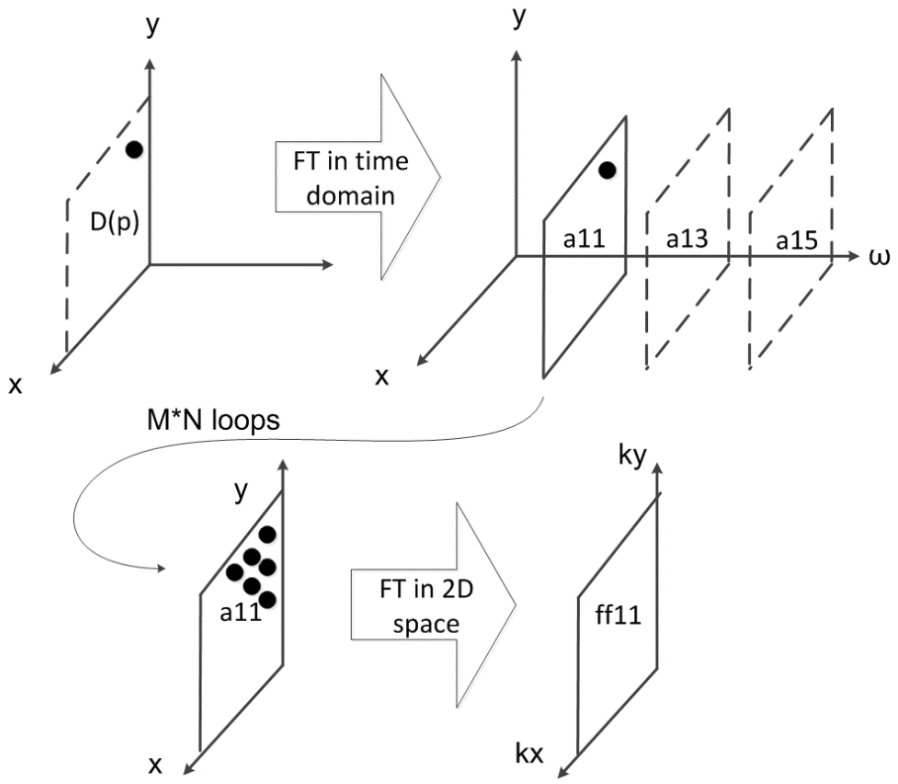

Fig. 3-3 Simulation of high harmonic generation with vortex beams with single plane emitters. The near field dipole emission is calculated at each point in space and the far field distribution is obtained by 2-dimensioanl Fourier transform.

To validate the simulation code, we reproduce the results of conservation of orbital angular momentum with single vortex driving beam. One unit of orbital angular momentum is imparted onto the fundamental beam and the phase variation on the harmonic beam is multiplied by the corresponding harmonic order. In Fig. 3-4, the first row shows the normalized intensity distribution of fundamental, 11^{th}, 13^{th} and 15^{th} order harmonic beams. Their phase fronts are plotted in the second row, which advances $1\times2\pi$, $11\times2\pi$, $13\times2\pi$ and $15\times2\pi$ phase on in azimuthal direction of fundamental, 11^{th} ,13^{th} and 15^{th} harmonic beams, respectively. The simulated results are consistent with the experimental results reported in [74] and [115].

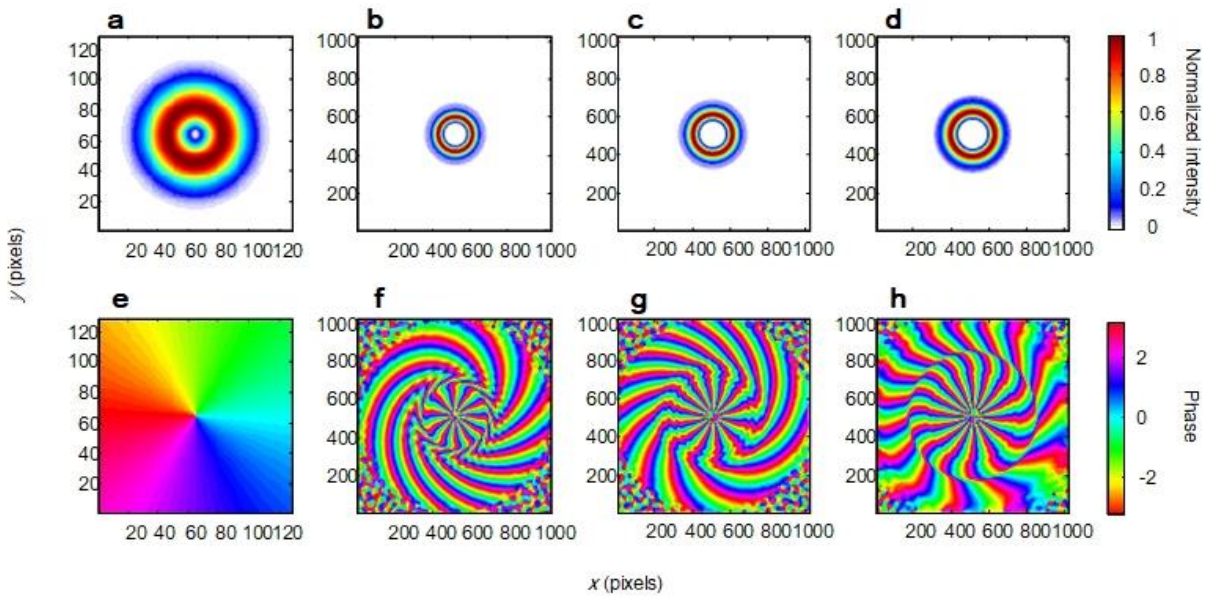

Fig. 3-4 Simulated results phase and intensity distribution of high harmonic beam driven by single vortex fundamental beam. (a-d) the intensity distributions of fundamental, 11th, 13th and 15th harmonics. (e-h) the phase distribution of fundamental, 11th, 13th and 15th harmonics.

The code is extended to have two input beams with a small relative angle ~40 mrad and to simulate the high harmonic generation process proposed in Fig. 3-2. Instead of the single vortex beam with a spiral wave front, the total driving field becomes the interference between a Gaussian and a vortex beam. The dipole response is calculated at each meshed point in space where the intensity is high. For the points far away from the beam the dipole responses are set to be zeros, which saves computation time while keeping the far field spatial resolution.

We obtain the simulated results in the far field that is shown in Fig. 3-5. The figure shows that the beams diffracted in first order exhibit donut shapes in their intensity profiles and have spiral wave front changing from 0 to 2π in the phase plot, which is the same as that of the fundamental. The phase front spirals are the same for both 17th and 19th harmonics, in other words, the orbital angular momentum we transferred to the high harmonic beams are independent on their harmonic orders. We can obtain arbitrary unit of orbital angular momentum by changing the topological charge of the perturbing beam or spatially select a different diffracted order.

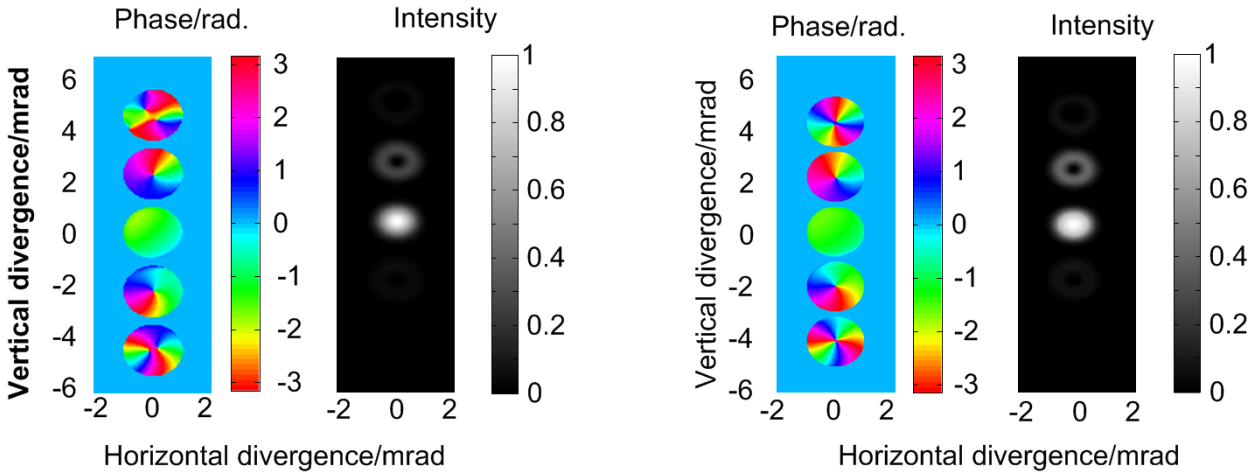

Fig. 3-5 Phase and intensity profiles of the high-harmonic vortex beams with controlled OAM. Simulated results of phase and intensity profiles of the 17th (left) and 19th (right) harmonic emission in the far field.

To experimentally reconstruct the intensity profiles of diffracted XUV vortex beams, the generated harmonics propagate to the far field and are detected by an imaging spectrometer. The spectrometer is composed of a vertical slit, an XUV imaging grating, a micro-channel plate, and a CCD camera; the plane of the slit is imaged onto the micro-channel plate using the imaging grating, and the CCD camera records the intensity profile on the phosphor screen of the micro-channel plate. The grating separates different orders of harmonics by mapping wavelength to the horizontal axis of the micro-channel plate.

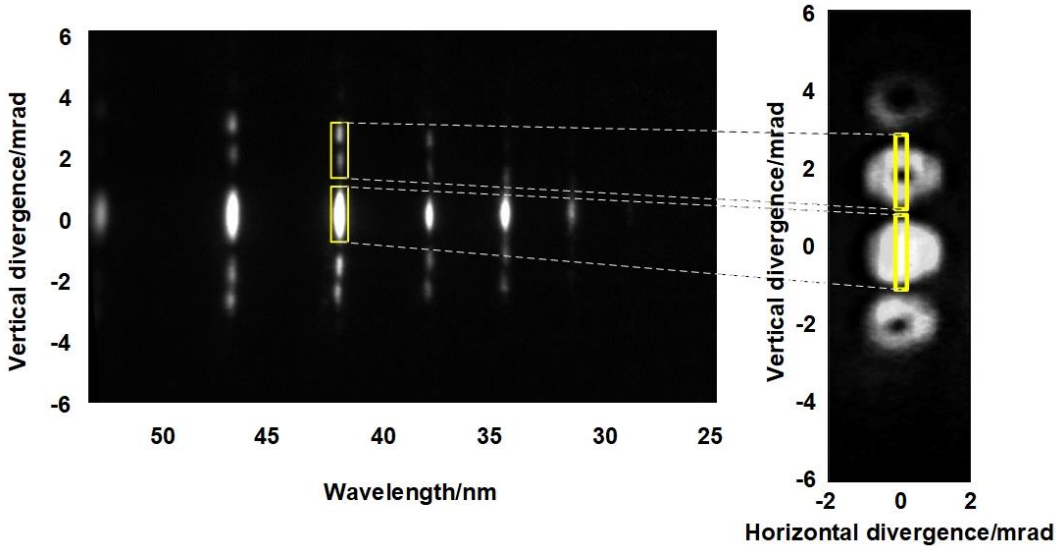

Fig. 3-6 Reconstructing the intensity profiles of diffracted XUV vortex beams. Left: the image recoded directly by the camera from the phosphor screen. The large spots around 0 mrad corresponds to the zeroth order Gaussian beams (l_{XUV} = 0 modes), while the split spots

above and below correspond to the diffracted XUV vortex; Right: reconstructed image by horizontally translating the slit and the grazing incident grating.

The harmonics beams are truncated vertically when passing through the slit of the spectrometer, as shown the yellow boxes in Fig. 3-6. In order to measure the full transverse profile of each harmonic, the slit and grating are moved simultaneously by a translation stage. Multiple images are recorded when the stage is moving and are composed according to different stage positions. The vertical slit is chosen to have a width of 100 μm, which ensures both sufficient flux and horizontal resolution.

Fig. 3-7 shows the reconstructed intensity profile of the 17th and 19th harmonics of 800 nm beams. The non-diffracted beams at the centre has Gaussian profile with bright centres while other diffracted beams have donut-like shape with dark centres. The separation between the first diffracted order and the non-diffracted beam is larger for 17th harmonic, which is also consistent with the conservation of linear momentum [146].

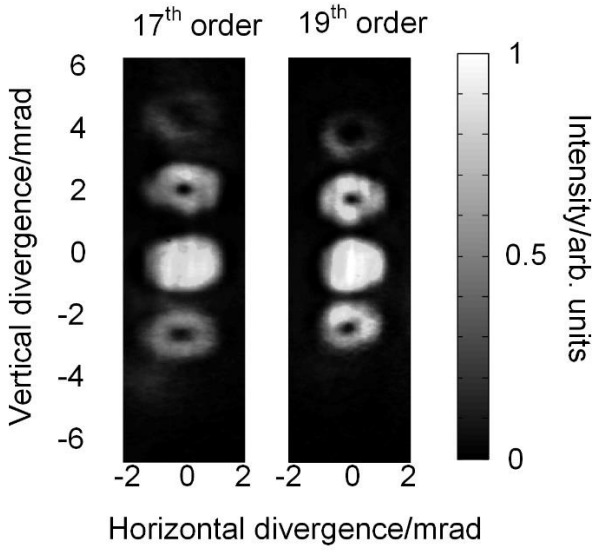

Fig. 3-7 Intensity profiles of the 17th and 19th order high-harmonic vortex beams with controlled OAM. Experimental results of the normalized intensity profile of the 17th and 19th harmonics recorded on the micro-channel plate.

An analogy with holography may be helpful to interpret this far field pattern. It is possible to think of the vortex XUV beam as being generated in a holographic fashion: the driving Gaussian beam and weak vortex beam respectively serve the roles of a reference beam and an object beam. Their interference imposes a fork-shaped holographic structure onto the plane of the emitting dipoles. As in standard holography, the diffracted orders preserve the wave front of the incident object (vortex) beam. As the analogy with holography implies, any method

that can induce phase modulation in the dipole emission, including a forked grating pattern in the alignment distribution of multi-electron molecules [147], can be used to imprint such holographic phase pattern in the gas medium.

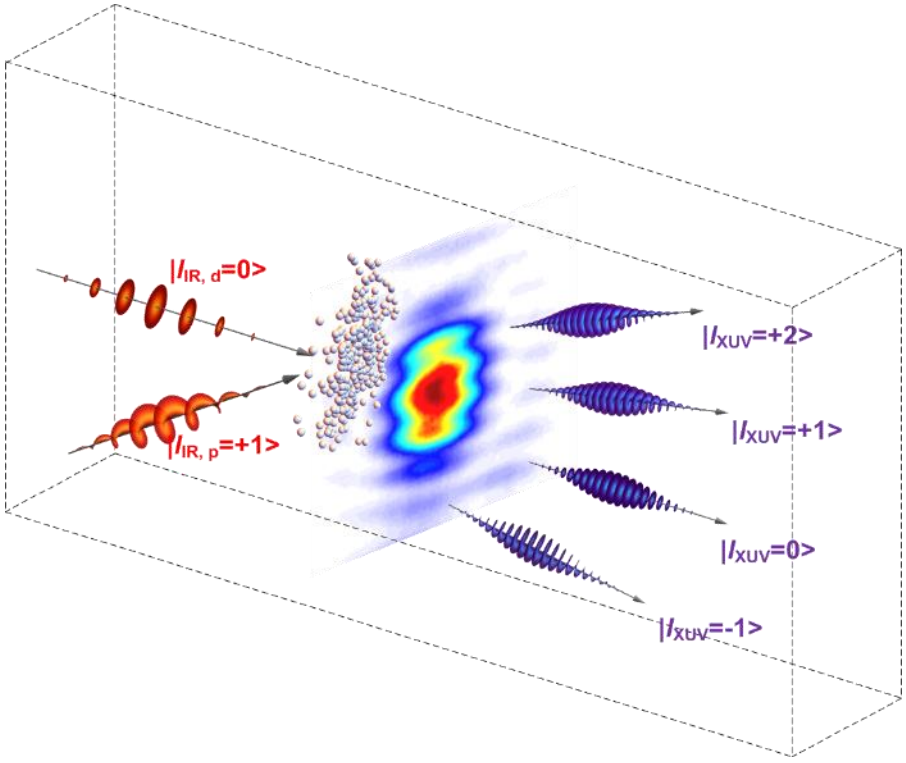

Fig. 3-8 Illustration of the holographic wave front control of high harmonic beams. The emitted phase of high harmonics is modulated by the interreference between the strong driving beam and the weak perturbing beam. The modulated dipole forms a hologram and transfer the pattern to the generated high harmonics. The generated high harmonic beams diffract into different orders and the diffracted beam replicate the wave front of the vortex perturbing beam.

As is often the case in nonlinear optics, momentum conservation gives a useful complementary perspective. Fig. 3-9 depicts the conservation of both the linear and the orbital angular momentum of the absorbed infrared photons, in the simplest case of third-harmonic generation. The emitted angle of the XUV photon is determined by the vector addition of linear momentum [146]. For this reason, the diffraction order in the vertical direction indicates how many photons from the vortex beam are absorbed. If OAM is also conserved, as shown in Equation (1),

$$l_{\mathrm{XUV}} = n_{\mathrm{IR,d}} l_{\mathrm{IR,d}} + n_{\mathrm{IR,p}} l_{\mathrm{IR,p}}\,, \tag{3.2}$$

where l_{XUV} is the topological charge of the emitted XUV photon, $n_{IR,d}$ and $n_{IR,p}$ are the number of photons absorbed from the driving and perturbing beams, respectively, $l_{IR,d}$ and $l_{IR,p}$ are the topological charges of the driving and perturbing beams, respectively. Then the topological charge of the XUV photon l_{XUV} must equal the sum of the topological charges of all the absorbed infrared photons, as predicated in Ref. 11. Because photons from the strong driving field carry zero OAM ($l_{IR,d} = 0$), and the $\pm 1^{st}$ order absorbs or emits one photon from the weak vortex beam ($n_{IR,p} = \pm 1$, $l_{IR,p} = 1$), any harmonic in the $\pm 1^{st}$ order diffracted spectrum should have ±1 unit of OAM. In other words, the topological charges of the XUV beams are determined by the perturbing infrared beam.

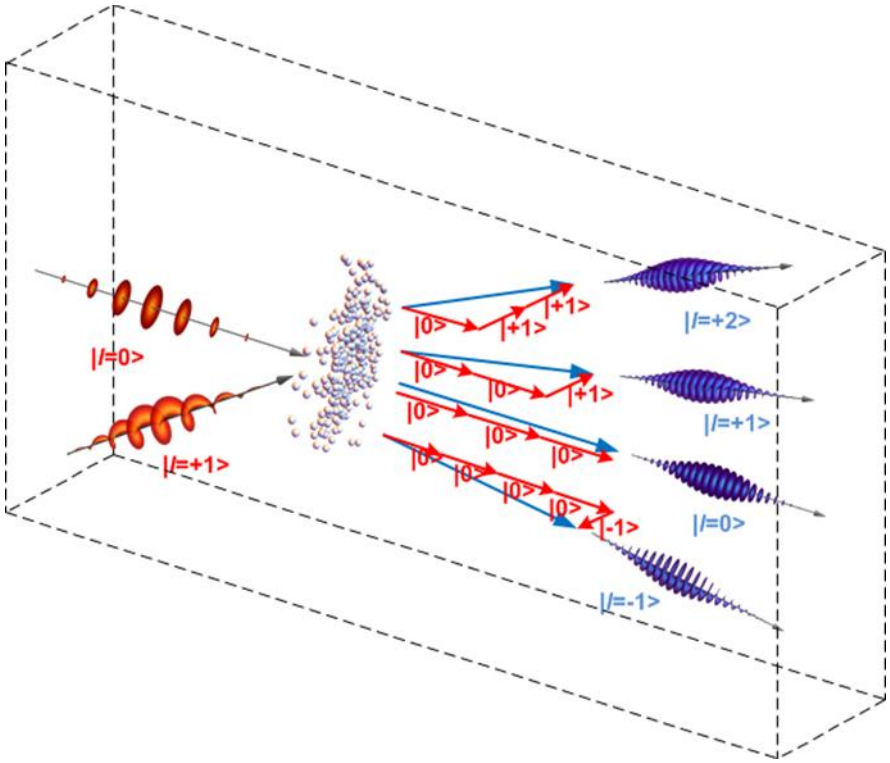

Fig. 3-9 Illustration of the conservation of linear and orbital angular momentum in a third order harmonics generation case. The emitted angle of the XUV photon is determined by vector addition of linear momentum. The topological charge of the XUV photon equals the sum of the topological charges of all the absorbed infrared photons.

As we increase the energy in the perturbing vortex beam, the depth of the phase modulation increases, and a second diffraction order appears. It also has a donut-shaped intensity profile but is less intense than the first-order beams. When the perturbing field has an intensity of $\sim 10^{-2}$ to the driving field, the energy ratio between the +1 diffraction order and the zero order at the 17^{th} harmonics is 0.18. The diffraction efficiency depends on the intensity of the perturbing beam and the mode overlap between the perturbing and driving beams. Experimental results, including second-order diffraction, are shown in Fig. 3-7 for the 19^{th}

harmonics and 17th harmonics. Since the process is perturbed by a same colour 800 nm beam, harmonic 18th is missing due to the half-cycle symmetry of the electric field [133].

The second-order diffracted beams have absorbed two photons from the perturbing vortex beams and from the conservation of OAM should therefore carry two units of OAM. These double-helical wave fronts with an azimuthal phase that varies from 0 to 4π, are also confirmed in our model simulations. In the experimental result in Fig. 3-7, we see that the second-order beams have a larger hole in their centre. The faster azimuthal phase variation of the $l_{XUV} = 2$ beam causes radiation to diffract from the singular centre more rapidly.

The intensity profile of each beam is highlighted in Fig. 3-10 for both the first and second-order beams of 19th harmonics. The larger dark centre of the $l_{XUV} = 2$ beam fits the second-order polynomial much better than it does a first-order ($l_{XUV} = 1$) beam profile. This can also be an evidence of the topological charge carried by the diffracted beams, since the higher charged beam have a larger hole at its centre. However, this indirect measument of intensity profile is still insufficient to determined the topological charge or the direction of helices. We need to obtain additional information to assess the wave front structure of the diffracted XUV beams.

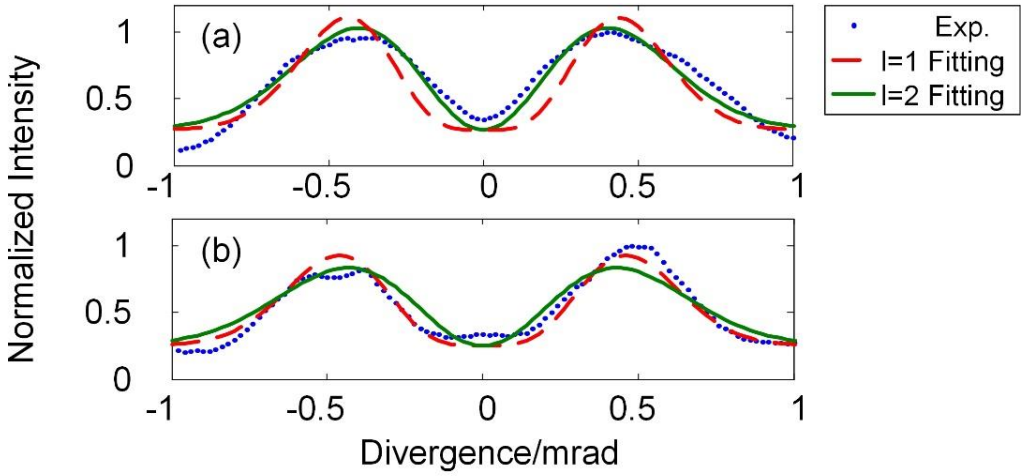

Fig. 3-10 Intensity fittings of 1st and 2nd diffracted beam intensity profiles with 1st and 2nd order Laguerre polynomials. (a) The measured beam profile for 1st diffracted order (blue dotted line) fits the green solid line ($l_{XUV} = 1$). (b) The measured beam profile for 2nd diffracted order (blue dotted line) fits the red dashed line ($l_{XUV} = 2$). This is an indication of the absolute value of the topological charges.

3.3 Determine the topological charge of high harmonics

We use interferometry to characterize the wave front and the direction of the helices. The experimental setup for measuring the phase structure is shown in Fig. 3-11(a). When characterizing the wave front by means of interferometry, a third infrared beam is added to produce XUV reference beams. The third beam has a larger beam diameter before the focusing lens, which leads to a tighter focus than the focus of the generating infrared beam. The divergence of the reference beam is large enough to enable the reference XUV beams to

overlap the $+1^{st}$, 0^{th} and -1^{st} orders XUV vortex beams. The two generating sources are separated by 150 μm, which is far enough to eliminate crosstalk between the two XUV sources.

The detection setup in the interferometric measurement for the holographic measurement does not contain a slit. This allows the entire beam to be observed. To allow both spatial and spectral resolution, the micro-channel plate is placed close enough to the grating that phase front information is preserved.

After passing through the spectrograph, the harmonics from the two sources interfere on the micro-channel plate. Fig. 3-11(b, c, d) show the interference patterns between the reference XUV beams and diffracted XUV vortex beams. For the $+1^{st}$ order diffracted beam, the forked pattern has one more fringe on the left than on the right, labeled by dashed line in Fig. 3-11(b). In contrast, the interference of the reference beam with the -1^{st} order (Fig. 3-11(d)) shows one additional fringe on the right. This difference in the fringe pattern indicates the opposite handedness of the helical wave fronts.

The sign of the topological charge on any diffracted harmonic can be changed by changing the linear polarization of the control beam that is incident on a *q*-plate [76], and the incident polarization can be modulated at MHz rates with a polarization modulator such as a Pockels cell [144]. We demonstrate this control by rotating a wave plate to change the topological charge from $l_{XUV} = +1$ to $l_{XUV} = -1$ as shown in Fig. 3-11(d,e). For applications in super-dense coding [145] and quantum communication [148], one can even use cascaded Pockels cells and *q*-plates of various topological charges [149], with each Pockels cell operating at MHz rates, consistent with the MHz-repetition-rate, high-harmonic sources that have already been demonstrated with both cavity-based and single-pass schemes [150].

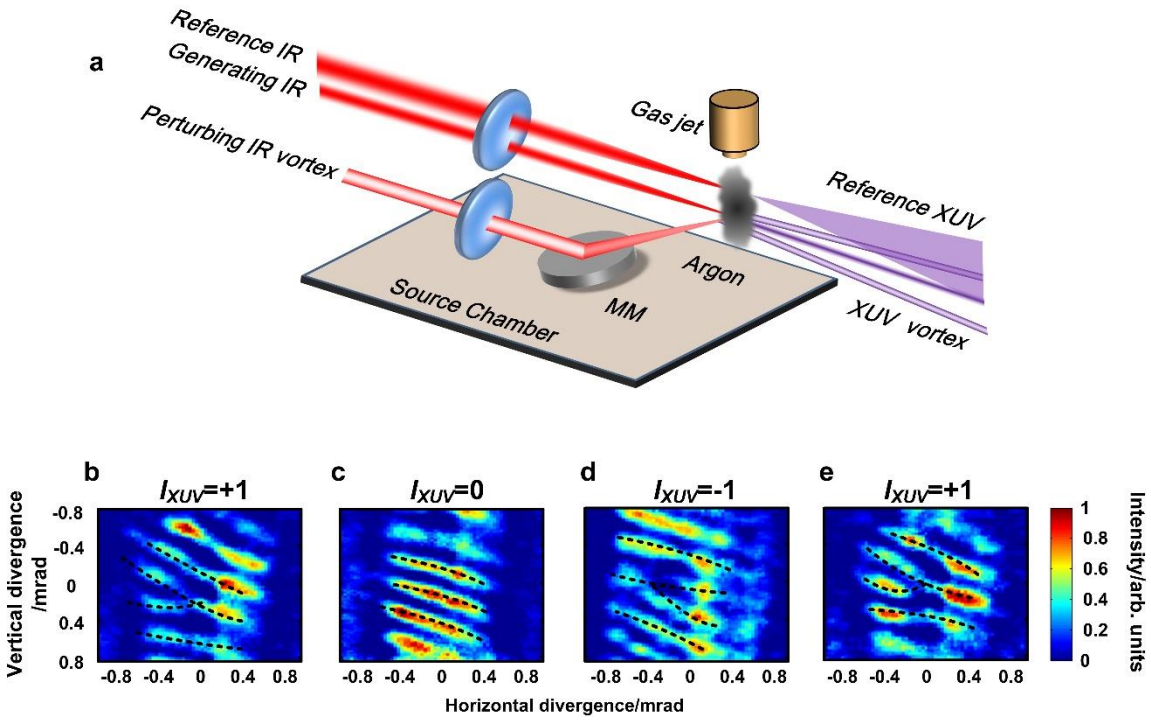

Fig. 3-11 Characterization of wave fronts and modulation of topological charges. (a) Schematic of the interferometric wave front characterization procedure. (b,c,d) Interference patterns of the Gaussian reference beams and OAM beams of charges l_{XUV} = +1,0,-1. (e) The sign of topological charge at -1st order diffraction is flipped from l_{XUV} = -1 to l_{XUV} = +1 by changing the incident polarization.

3.4 Discussion and Implications

The first application that we propose here is super-resolution laser machining. The essence of STED microscopy is to use the saturation of depletion to exploit the feature at the centre of an OAM beam [88]. This STED idea can be used for other phenomena that have a similar response. In laser processing, for example, desorption of a thin layer [151] can potentially be exploited in a STED-like manner. Consider the case where a donut-shaped XUV beam is linearly absorbed by a thin layer of polymer deposited on a fused silica substrate. XUV-injected electron-hole pairs are created in the thin-layer material except at the dark centre of the beam. A following IR laser pulse can cause an avalanche buildup of these carriers, depositing energy in the material where the carriers were created. The intensity of the guiding pulse can be much lower than the damage threshold because the following IR pulse [152] deposits any extra energy that is required. The thin layer will be desorbed where the deposited energy exceeds the damage threshold. Since XUV beams are selectively absorbed near the surface and the absorption can be tuned to exploit the atomic structure of the layer or substrate, the machining stops at the thin film/substrate interface when the thin layer is completely removed. Such selective absorption prevents the substrate from being engraved and gives rise to the saturable behavior that enables super-resolution processing.

The short wavelength of XUV beams affords much higher resolution than the machining process based on the use of an IR field. Therefore, we propose that carrier-injection-controlled machining, which so far has only been explored with Gaussian control beams at ultra violet wavelength [152], will now enable laser machining (and lithography) on the sub-nanometre scale.

The approach of using a weak field to control the harmonics created by the strong fundamental pulse opens an important channel to link mature infrared optical devices to XUV radiation and can serve as an alternative solution to making optical components that function in the XUV and soft X-ray region. Since the perturbing beam is more than two orders of magnitude weaker than the driving laser, this method allows liquid-crystal-based, programmable optical devices to be used in spite of their rather low damage thresholds. This brings us to X-ray-based communications, which is the second important applications that we propose.

The potential for fast modulation makes high-harmonic beams potential candidates for long-distance space communications, since shorter-wavelength beams diffract much less upon propagation and support extremely large data transmission bandwidths. X-ray-based communication may also overcome ionization blackouts and make it possible to communicate with hypersonic vehicles or re-entering spacecraft.

But this is not all: there is a rapidly increasing interest in using the entanglement of OAM in quantum key distribution and communication. Using classical concepts, we estimate of the diffracted efficiency of the dipole phase grating and illustrate the potential for interesting quantum optics of extreme nonlinear interactions in high harmonic generation. We make the following assumptions to describe the interaction of a single perturbing photon.

- a single perturbing photon in a mode that optimally overlaps in space (S) and time (t) the driving laser pulse.
- $E = h\nu$ is used to estimate a classical energy of a single photon.
- The classical intensity is estimated by by E/St.
- We use the known characteristics of diffraction gratings to estimate the diffracted light, although the diffraction efficiency is insufficient to describe the behavior of a single photon at specific frequency.

Our intension with the estimate below is to motivate the requirement for a quantum theory of extreme nonlinear optics. We are motivated by the potential to use one photon of an entangled pair as the perturbation beam. Of course, quantum optics can be important under much less extreme circumstances.

For our estimate, we will use an 800nm fundamental pulse with 1mJ energy per pulse or $N = 4\times10^{15}$ photons per pulse, 5×10^{14} W cm^{-2} intensity at focus and 10^{-4} energy conversion to the sum of all harmonics in neon gas. For convenience we will assume that 100eV (65th harmonic) can represent the properties of all diffracted photons. These choices define the threshold diffraction efficiency $\eta_{TXUV} = 1.67\times10^{-10}$ that we will need for the grating to diffract one photon.

The diffraction efficiency of a sinusoidal phase grating is given by,

$$\eta_{\mathrm{XUV}} = \left(\frac{J_1(\delta_{\mathrm{XUV}})}{J_0(\delta_{\mathrm{XUV}})} \right)^2 \underset{\delta \to 0}{=} \frac{1}{4} {\delta_{\mathrm{XUV}}}^2, \tag{3.3}$$

where δ_{XUV} is the phase modulation depth of the emission dipole at XUV wavelength in near field. Using equation (3.3) we calculate the threshold phase modulation depth for XUV

$$\delta_{\mathrm{TXUV}} = \sqrt{4\eta_{\mathrm{TXUV}}} = 2.6 \times 10^{-5} \text{ rad}. \tag{3.4}$$

Knowing the required modulation, we can estimate the energy ratio between the strong and weak IR beams needed to create it. We define a perturbation parameter $\varepsilon = E_{\mathrm{p}}/E_{\mathrm{d}}$, where E_{p} and E_{d} are the perturbing and driving electric field respectively.

The phase estimate can be broken into two parts: a. the phase modification due to changes of the electron trajectory caused by amplitude variation of the driving laser field; b. the phase modification due to change of recombination time due to the phase variation of the driving field.

a. For the nonlinear phase that arises due to changes to the electron trajectory, the unperturbed phase of q^{th} harmonics at frequency Ω is

$$\Phi_{\mathrm{amp}}(\Omega) = \frac{1}{\hbar} \int_{t_{\mathrm{b}}}^{t_{\mathrm{c}}} \frac{(p - e\mathbf{A})^2}{2m_e} + I_{\mathrm{p}} dt - \Omega t_{\mathrm{c}}. \tag{3.5}$$

The change of action caused by a perturbed field can be evaluated by

$$\begin{aligned} \Delta\Omega_{\mathrm{amp}}(\Omega) &= \frac{\partial \Phi}{\partial t_{\mathrm{c}}} dt_{\mathrm{c}} + \frac{\partial \Phi}{\partial t_{\mathrm{b}}} dt_{\mathrm{b}} + \frac{\partial \Phi}{\partial p} dp + \int_{t_{\mathrm{b}}}^{t_{\mathrm{c}}} \frac{-e(p - e\mathbf{A})}{\hbar m_e} dA dt \\ &= -I_{\mathrm{p}} dt_{\mathrm{b}} + \int_{t_{\mathrm{b}}}^{t_{\mathrm{c}}} \frac{-e(p - e\mathbf{A})\mathbf{A}_{\mathrm{p}}}{\hbar m_e} dt \\ &= \varepsilon \int_{t_{\mathrm{b}}}^{t_{\mathrm{c}}} -\frac{eE_0}{\hbar m_e \omega^2} E_0 \left[\sin(\omega t_{\mathrm{b}}) - \sin(\omega t) \right] \sin(\omega t + \Delta\varphi) dt - I_{\mathrm{p}} dt_{\mathrm{b}} \end{aligned}, \tag{3.6}$$

where t_{c} is time of recombination and t_{b} is time of birth, p is the canonical momentum, I_{p} is the ionization potential of the gas medium, A is the unperturbed vector potential of the driving laser field, A_{p} is the vector potential of the perturbing laser field, E_0 is the amplitude of the

driving laser field, ω is the frequency of driving laser field and $\Delta\varphi$ is the phase difference between the driving and perturbing laser fields.

b. For the nonlinear phase influenced by the phase variation of the driving field,

$$\Delta\Phi_{\mathrm{ph}}(\Omega) = q \arctan \frac{\varepsilon \sin \Delta\phi}{1+\varepsilon \cos \Delta\phi} \ . \tag{3.7}$$

The total phase shift of the dipole emission equals to the sum of the above two contributions. Since the perturbation is small, we only keep the first order term. The coefficient $d\delta/d\varepsilon$ is plotting in Fig. 3-12. The phase modulation is stronger for electrons which recombined later (the higher order harmonics).

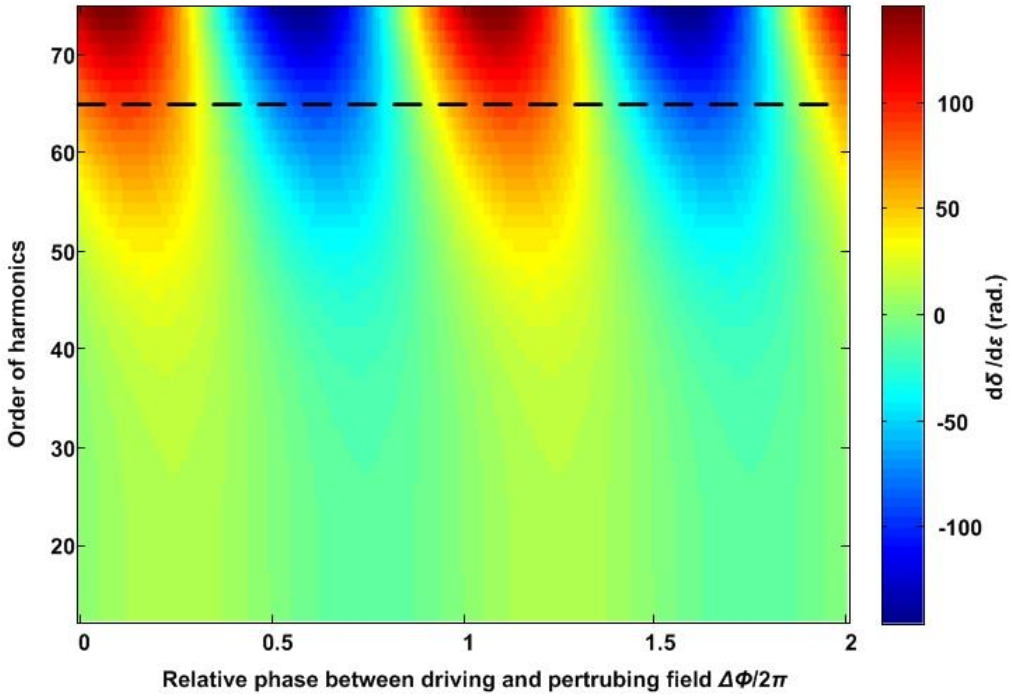

Fig. 3-12 Phase modulation coefficient dδ/dε in radians for different electron trajectories

Taking the trajectory corresponding to the 65th order (the dashed line), we can find that the ratio between modulation depth ($d\delta$) and the perturbation parameter ($d\varepsilon$) is 95. Therefore the ratio between the weak and strong IR field is

$$\varepsilon = \frac{d\varepsilon}{d\delta}\delta_{\mathrm{TXUV}} \approx 2.7\times10^{-7}, \tag{3.8}$$

and the minimum number of photons in the weak beam to deflect one XUV photon into the first order is

$$N_{\mathrm{p}} = N\varepsilon^2 \approx 290. \tag{3.9}$$

This implies that one high harmonic photon would be scattered for each 290 incident photons.

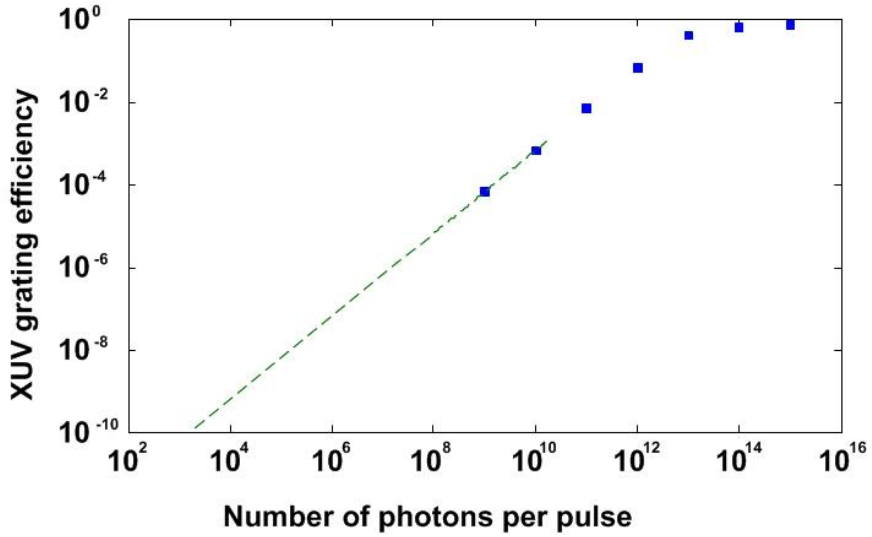

Fig. 3-13 Scaling XUV diffraction efficiency verse the number of photons per weak pulse

A similar diffraction efficiency is found by simulations using the strong field approximation. We plot the intensity ratio between the 1st and 0th order diffraction on XUV versus the number of photons in the weak pulse. Fig. 3-13 shows a linear dependence of the diffracted light intensity on the intensity of the weak control beam. This is the same scaling that we have discussed above. Projected to low intensity, the simulation results arrive at the same XUV diffraction efficiency η_{xuv} calculated above.

To conclude, we use wave-mixing to add a single photon from a weak beam together with its orbital angular momentum to a XUV beam created by a strong Gaussian fundamental beam. We then measure the beam that we have created with holography. The general approach that we demonstrate allows whatever orbital momentum that is placed in the weak beam to be transferred to the XUV. This holographic approach is not only limited in creating orbital angular momentum beams but also other wave front structures [138].

We also analyze and discuss on three possible implications: 1) Space communications: It is well known in conventional information and communications technology (ICT) that digital information can be encoded in the orbital angular momentum states of a beam. By showing

that orbital angular momentum can be transferred from a weak beam to the XUV and switched with a pockels cell, we open a route to high-data-rate (>100 MHz) XUV communications. To our knowledge, ours is the first proposal for how data-rate information can be encoded on an XUV beam. 2) STED-like laser machining: By producing $l = 1$ beams in the XUV, it may seem that we have opened sub-wavelength imaging in the XUV where the wavelength of 1-10nm suggests Angstrom scale spatial resolution. It will be especially significant given that IR assisted laser machining provide alternative solution to overcomes the limited flux of current harmonic-based sources. 3) Quantum photonics in the XUV – Our approach to wave-mixing allows us to predict that the electric field equivalent of only about 100 photons in the weak beam is sufficient to produce a single photon with orbital angular momentum on the XUV beam. We believe that this is the first indication that there will be a possibility of exploring quantum optics (and perhaps quantum information) that relies on strong field physics and high harmonic generation.

Chapter 4 High harmonic generation with polarization structured beams

Strong field laser physics has primarily been concerned with controlling beams in time while keeping their spatial profiles invariant. In the case of high harmonic generation, the harmonic beam is the result of the coherent superposition of atomic dipole emissions. Therefore, fundamental beams can be tailored in space, and their spatial characteristics, for example their phase structures will be imparted onto the harmonics [74,114,118,138,139].

Besides the wave front, we can also shape the polarization of the fundamental beam. In this chapter, we produce high harmonics using a space-varying polarized fundamental laser beam, which we refer to as a vector beam [96]. By exploiting the natural evolution of a vector beam as it propagates, we convert the fundamental beam into high harmonic radiation at its focus where the polarization is primarily linear. This evolution results in circularly polarized high harmonics in the far field. Such beams will be important for ultrafast probing of magnetic materials [153].

The liquid crystal devices introduced in previous chapters allow us to shape the spatial mode of a laser beam not only in phase but also polarization "at will", point by point, in their transverse plane [95,154]. Despite their wide utility in the visible and near infrared, such devices cannot be used directly in the extreme ultraviolet. However, it is possible through high harmonic generation to upconvert the polarization structures of the fundamental beams to the extreme ultraviolet, similar to the phase front shaping [118,138,155].

Nevertheless, it is much more common to shape the fundamental beam that produces high harmonics in time rather than in space. Numerous studies have shown the power of shaping the temporal polarization in strong field experiments. A typical method for producing isolated attosecond pulses uses a fundamental pulse with time varying polarization [42–44]. This method relies on the fact that conversion from the fundamental to the XUV requires nearly linear polarization [30]. Generating circularly polarized XUV beams by mixing counter rotating bicircular field with different colours is another good example of shaping the laser field in the temporal domain. The field is shaped to have three-fold symmetry and enables the tunnelled electron to recombine with its parental ion every one third of the fundamental optical cycle [33,120,156]. The field shaping in temporal domain enables efficient generation of circularly polarized high-order harmonics. Alternatively, the circularly polarized harmonics are also reported by mixing two non-collinear bicircular driving laser beams [122,157]. Reducing the relative angle is helpful to optimize the phase matching in producing XUV radiation. To further exploit the spatial degree of freedom, the beam-mixing scheme evolves into the direct modulation of spatial modes of laser beams. Comparing to the non-colinear beam-mixing schemes, the laser beam can be modulated pixel-by-pixel enabling a complete and more flexible control of its spatial properties. This opens a new field of vectorizing the radiation in both strong infrared and XUV radiation.

In this chapter, we use liquid crystal technology [69,111] to shape the polarization of a beam in space rather than in time. Such a beam naturally evolves upon propagation, with the polarization structure of the beam changing from near to far field [113,158]. The liquid crystal

plate that we use is tuned [69,159] to give half-wave retardation at the fundamental wavelength. The device's liquid crystal molecules are aligned in different orientations in each quadrant. With this device and a quarter-wave plate, we can generate the vector beam with space-varying beam profile and produces high harmonics with complex polarizations.

4.1 Structuring the polarization of the driving laser beam

Specifically, we modify the transverse profile of a Gaussian fundamental beam such that its optical properties vary from one quadrant to another. In this case, adjacent quadrants are defined by opposite circular polarizations with different optical phases. The local polarization state evolves when the beam propagates. Fig. 4-1 depicts the evolution of the polarization state upon being focused. In the far field, we show that this beam evolves into one with linear polarized light in each of four quadrants with neighbouring segment perpendicularly polarized and each phase delayed by $\pi/2$. This beam then interacts with a gas-phase nonlinear medium, thus creating high harmonics in the XUV where the spatial structure of the original linearly polarized regions is preserved. As with the fundamental, the polarization state of the resulting XUV vector beam will also evolve as the beam propagates from near to far field.

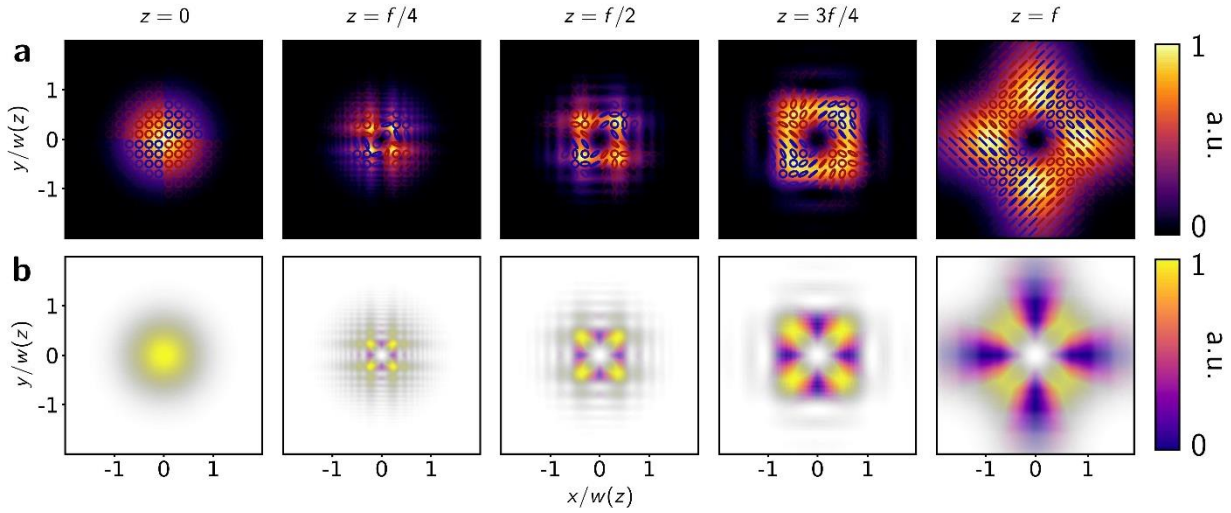

Fig. 4-1 Profile of the structured pump beam upon being focused The beam profile is considered after the phase plate to its focus, where *f* is the focal length. (a) Total intensity of the beam overlaid with its space-varying polarization pattern. Left-handed polarized ellipses are drawn in red while right-handed polarized ellipses are drawn in blue. (b) Absolute value of the third Stokes parameter indicating the degree to which the beam is elliptical, where 0 corresponds to purely linear polarization and 1 corresponds to purely circular polarization.

More specifically, the fundamental laser beam passes through the liquid crystal plate and then is focused by a lens with a focal length of *f*. The polarizations profile of the fundamental in its transverse plane is plotted in Fig. 4-1(a). Both the polarization and the intensity distribution change, while the beam is propagating from z = 0 to z = *f*. In addition, the ellipticity of the

beam change from everywhere circular to locally linear as shown in Fig. 4-2(b), where yellow colour corresponds to purely circular polarization and the blue colour corresponds to purely linear polarization.

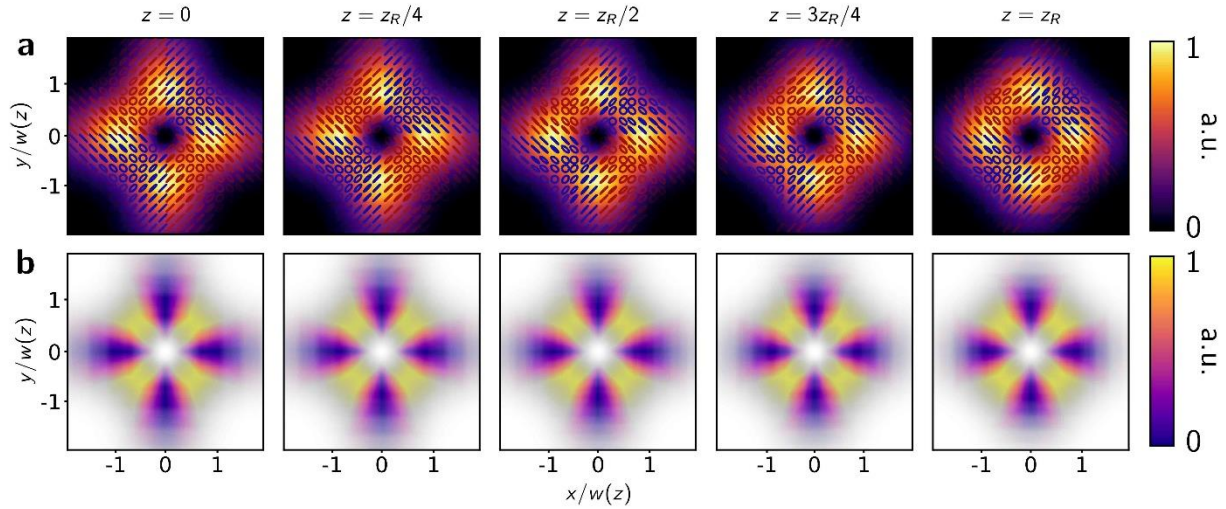

Fig. 4-2 Profile of the focused structured pump beam The beam profile is considered along one Rayleigh range from its focus. (a) Total intensity of the beam overlaid with its space-varying polarization pattern. Left-handed polarized ellipses are drawn in red while right-handed polarized ellipses are drawn in blue. (b) Absolute value of the third Stokes parameter indicating the degree to which the beam is elliptical, where 0 corresponds to purely linear polarization and 1 corresponds to purely circular polarization.

In contrast that the polarization profile changes while the beam propagating from the phase plate to its focal plane, the polarization profile keeps almost unchanged within the Rayleigh range, as shown in Fig. 4-2. This allows us to assume that high harmonic emitter in a single-plane model while using a thin gas jet that is much shorter than the Rayleigh range of the fundamental beam.

4.2 Generating high harmonics with varying polarizations

We focus the infrared beam with a 30 cm lens into a pulsed Argon gas jet placed within a vacuum chamber. The diffractive nature of light causes the field from each segment to interfere and form new local polarization states at the focal plane. This conversion is illustrated in Fig. 4-3(a), where we see how ellipticity evolves while the driving beam is focused: the incident beam is entirely circularly polarized, a feature represented by its yellow colour. After being focused by a lens, the polarization approaches to a linear polarization state, represented by the blue sections of the beam. The linear polarization appears first at the interface between two adjacent segments defined by counter rotating circular states. The orientation of the linear polarization is determined by the quadrants' relative phase difference. As the beam propagates diffraction increases the overlap between two adjacent quadrants. At the focus, the fundamental beam is linearly polarized where the field is most intense, and these regions are where high harmonics will be generated.

Efficient high-harmonic production relies on linearly polarized driving laser fields [30,32]. The local ellipticity of the fundamental beam at the focal plane can be obtained by measuring the transmitted intensity profile through a linear polarizer. By rotating the linear polarizer, the light field is projected onto different linear bases. The ratio between the minimum and maximum intensity of each point in space is plotted in Fig. 4-3(b). The strong modulation confirms that the field propagation constructively interferes to create locally linearly polarized light at the focus, thus enabling efficient high harmonic generation. The relative phase delay is measured by interfering the fundamental beam with a diagonally polarized plane wave. The resulting interference pattern is shown in Fig. 4-3(c). The shifted fringe pattern indicates a π-phase difference between the opposing segments, and each segment is phase delayed from its neighbour by $\pi/2$.

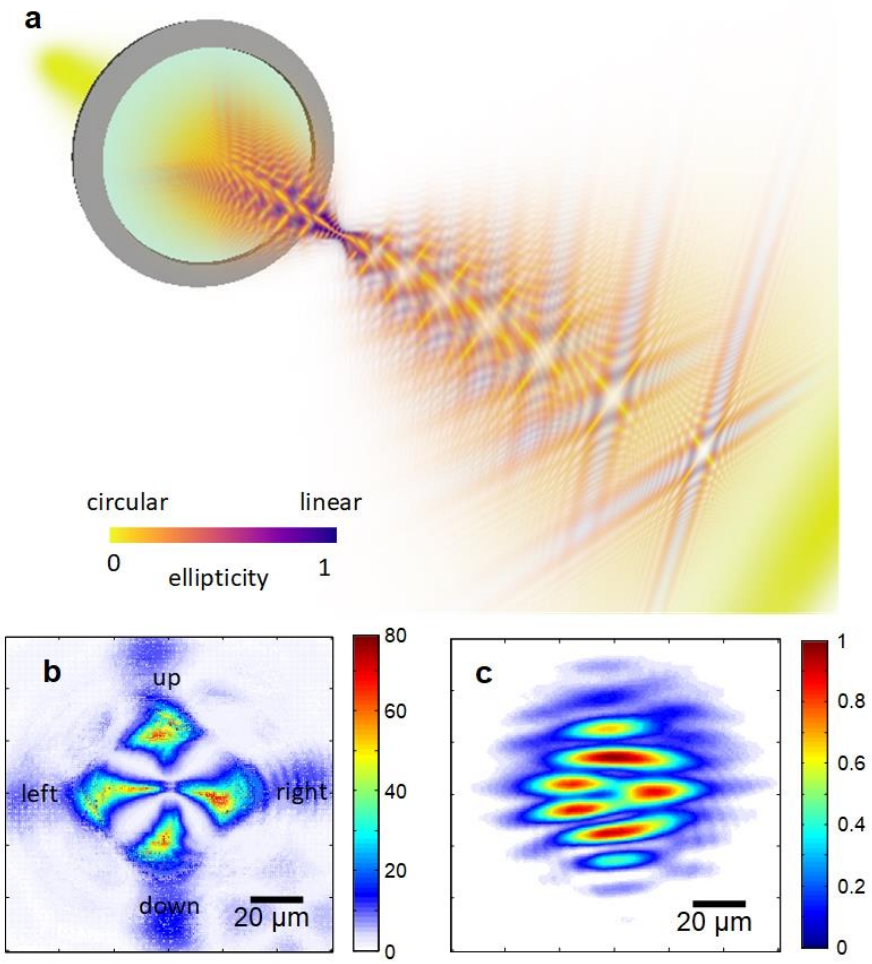

Fig. 4-3 Shaping and characterizing the optical polarization of the fundamental driving laser beam. (a) The evolution of polarization state of a vector beam while it is being focused. The yellow-coloured part shows where the polarization is circular and blue-coloured part shows where it is linear. The linear parts start to show up at the interface between adjacent

segments and are dominant at the focal plane. The circular state is restored when the beam propagates away from the focal plane. (b) Measured ratios between the maximum and minimum intensity at each point in space for various rotation angles of the linear polarizer. A higher extinction ratio indicates that the local polarization state is more linear. (c) The interference pattern between the fundamental vector beam and Gaussian beam at the focal plane. The shifted fringe pattern indicates a π-phase difference between the opposing segments, and each segment is phase delayed from this neighbour by $\pi/2$.

Next, we analyze what we expect as the beam is converted to harmonics. Between the adjacent segments, the driving field has a $\pi/2$ phase difference. This phase difference between the quadrants is transferred to XUV dipole emission by multiplying them by $N = 2k+1$, where N is the high harmonic order and k is an integer. Then the XUV emitting phase φ_{XUV} of the four segments becomes [160]:

$$\varphi_{\mathrm{XUV}} = N\begin{bmatrix} \frac{\pi}{2} & 0 \\ \pi & \frac{3\pi}{2} \end{bmatrix} = (2k+1)\begin{bmatrix} \frac{\pi}{2} & 0 \\ \pi & \frac{3\pi}{2} \end{bmatrix} = \begin{cases} \begin{bmatrix} \frac{3\pi}{2} & 0 \\ \pi & \frac{\pi}{2} \end{bmatrix} \bmod 2\pi, \text{ for } k \text{ odd} \\ \begin{bmatrix} \frac{\pi}{2} & 0 \\ \pi & \frac{3\pi}{2} \end{bmatrix} \bmod 2\pi, \text{ for } k \text{ even} \end{cases} \tag{4.1}$$

Eq. (4.1) shows that the phase pattern is preserved even after the frequency up-conversion of all odd order harmonics. After the high harmonics are generated at the focus, the XUV radiation propagates in free space. Since both the local polarization and the $\pi/2$ phase retardation between neighboring quadrants are preserved on conversion, the XUV beam will restore the circular polarization when it propagates away from the generating site. The intensity induced dipole phase will also contribute to the phase structure in each quadrant. However, each quadrant has same intensity distribution and therefore the same dipole phase structure in the emitting phase. Therefore, the phase relation between the quadrants described in Eq. (4.1) is still valid. The up-converted phase has a reversed handedness in the helical phase fronts between adjacent harmonic orders. As a result, the harmonic emission of adjacent harmonic orders will have opposite handedness in the same segment, since the phase differences between the orthogonal linear components are $\pi/2$ and $-\pi/2$, respectively.

4.3 Characterizing the polarization structured high harmonics

We characterize the polarization distribution of the XUV beams in space by measuring their two-dimensional spatial profiles in the far field. The experimental setup is shown in Fig. 4-4.

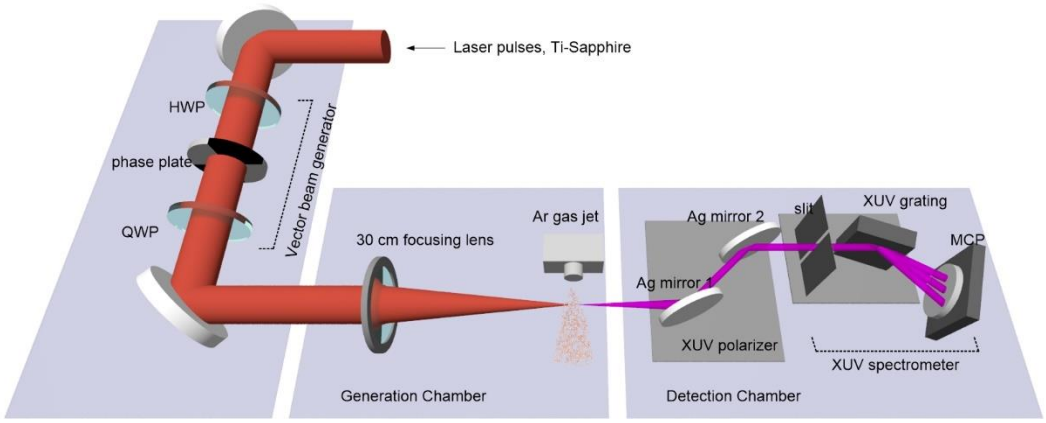

Fig. 4-4 Experimental setup for measuring XUV polarization using an XUV polarizer. The linearly polarized driving laser beam is prepared by going through a half-wave plate, a designed phase plate and a quarter-wave plate to convert into circular state. It is then focused by a f = 30cm lens into a vacuum chamber to interact with argon noble gas. The generated XUV radiation propagates through a XUV linear polarizer placed 50cm from the gas jet and in the far field for the XUV light. The reflectivity of a silver mirror in the XUV is polarization dependent. With a 23-degree angle of incidence to a pair of silver mirrors we construct a XUV polarizer in front of a XUV spectrometer to select one linearly polarized state.

The fundamental infrared femtosecond pulses come from Ti:S laser system at 1 kHz repetition rate. The beam passes through a vector beam generator, which consists of a set of wave plates and a liquid crystal phase plate to control the local polarization. Then a 30 cm lens focuses the beam into a vacuum chamber where the intense laser pulses interact with noble gas atoms and produce high harmonics. The generated harmonics propagate into a differentially-pumped detection chamber, in which there is an XUV polarizer and an XUV spectrometer. To distinguish the two orthogonal linear polarization states, we implement two parallel silver mirrors as an XUV polarizer [161] with ~1:10 extinction ratio, as shown in Fig. 4-5. The high harmonic intensity detected on the micro-channel plate is measured while rotating the linearly polarized driving laser beam. The high harmonics are assumed to be polarized along the same direction as their fundamental. The polarized angle of the XUV polarizer is then defined by the XUV maximum transmission.

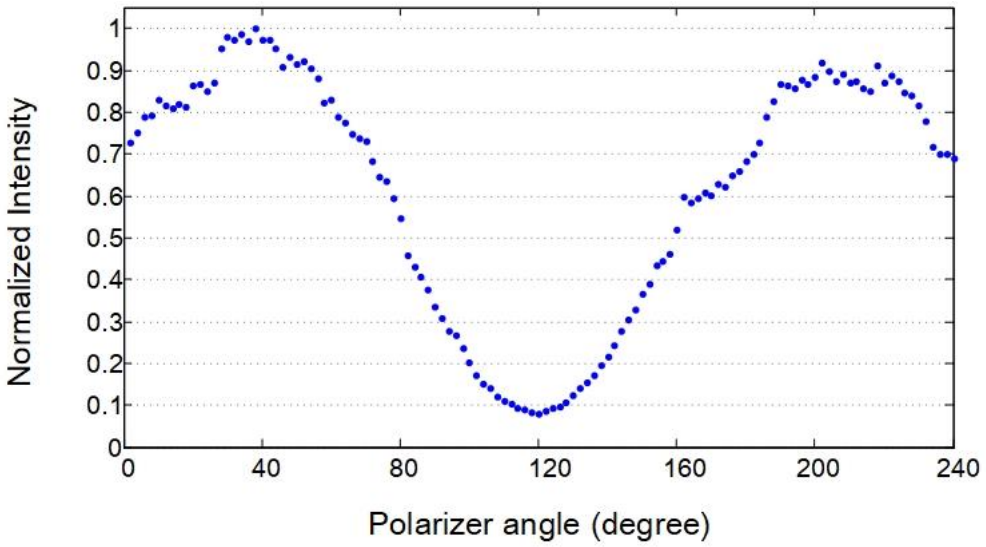

Fig. 4-5 Linear calibration of XUV spectrometer. Normalized transmitted intensity of XUV beam at the 25th harmonics order versus different equivalent polarizer angles, with respect to the direction of the polarization of the XUV beam. The extinction ratio between s- and p-polarizations is ~10:1.

First, the intensity beam profile of the 25th harmonic, Fig. 4-6(a), is reconstructed without passing through the XUV polarizer. Since our vector beam does not have azimuthal symmetry in either its intensity or polarization state, a two-dimensional beam profile measurement is required for every harmonic order. We send the XUV beam to an XUV spectrometer to get spectrally resolved signals. Any variation of the beam intensity profile in the vertical direction is directly recorded on our spectrometer in a single image. Then we take multiple images while translating the XUV spectrometer horizontally to obtain the intensity variation along horizontal direction. The two-dimensional image of the XUV beam profile is reconstructed by stacking the translated recorded spectrograms according to the position of the XUV spectrometer. We perform this beam profile measurement both with and without the XUV polarizer.

The beam consists of an array of bright spots, which is predicted to be circularly polarized. The multiple-spot distribution is the two-dimensional Fourier transform of harmonics distribution at the focal plane. It is also a signature of the high-order nonlinearity of this process, in which the high harmonics are produced nonlinearly as a function of the intensity and ellipticity. Such nonlinear transfer function is also Fourier transformed and convoluted in the far field, which results in multiple spots structure in the detecting plane. Furthermore, the adjacent spots have the opposite handedness, which they inherit from the driving field.

The polarizer is difficult to rotate physically. In addition, it is difficult to align with the beam propagation direction, so that the incident angle can be maintained while the XUV polarizer is rotated. In lieu of rotating the XUV polarizer, we rotate the polarization of the incident beam by introducing a half-wave plate in front of the liquid crystal plate in the experiment. We change the polarizing orientation of the incident driving laser beam, which is equivalent to

physically rotating the XUV polarizer, except for the polarization selectivity of the XUV grating. In our setup, two parallel mirrors are installed in front of the spectrometer to ensure the same incident angle. To rotate the polarization state of the incident fundamental driving laser beam, a half-wave plate is placed in front of the phase plate. When the half-wave plate is rotated by a small angle θ, the polarization of the incident beam is rotated by 2θ. After going through a phase plate, the polarization of each segment is rotated by -4θ with respect to the phase plate and obtains a -2θ rotation in the lab frame. Then the quarter-wave plate is rotated by -2θ, to retain the same incident angle between optical axes of the wave plate with the incident polarization.

Using the same approach, we reconstruct the intensity profile of the transmitted beam, after the XUV vector beam passes through the XUV polarizer. If the polarizer is set at a 0° relative angle, with respect to the polarization direction of the upper and lower segments of the fundamental as labelled in Fig. 4-3(b), the transmitted beam shows horizontal fringes (Fig. 4-6(b)). These fringes can be interpreted as two-source interference of the two generating segments (upper and lower ones), which are displaced in the vertical direction. Each dark node in the vertical direction indicates a π-phase jump in the XUV due to the interference. Radiation from the other two segments (left/right) is not transmitted, since it is orthogonal to the direction of the XUV polarizer, which is aligned with the polarization of the upper/lower segments.

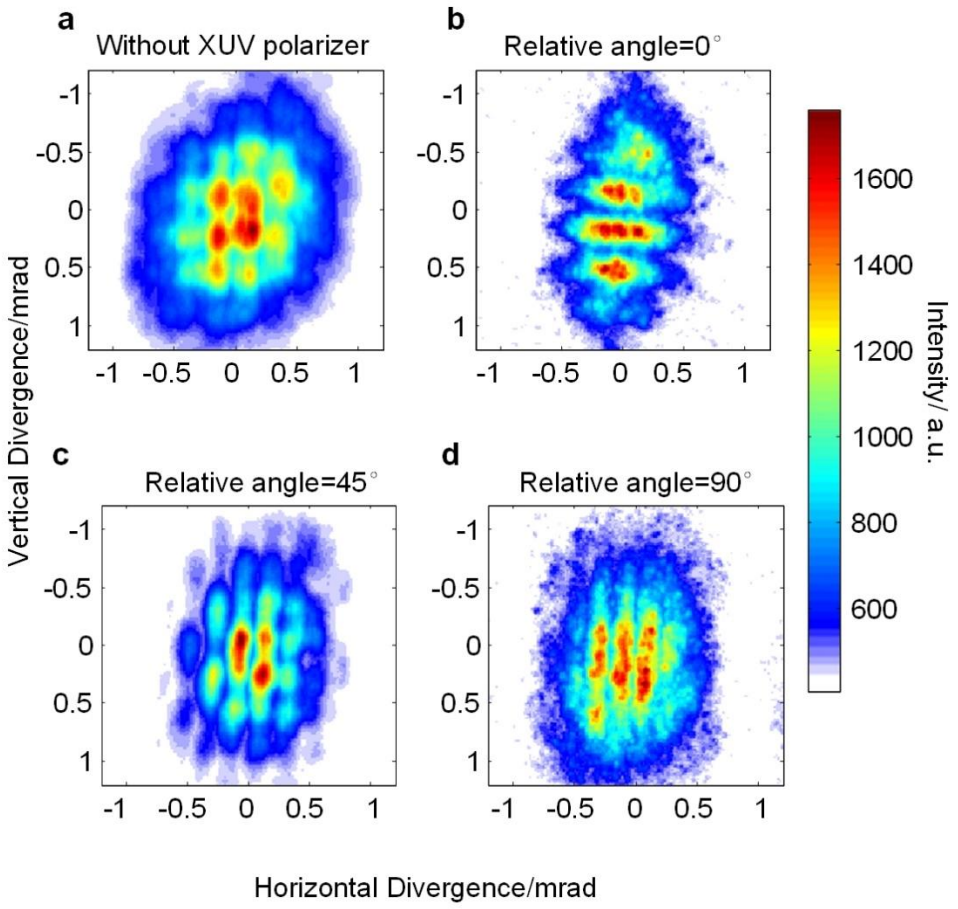

Fig. 4-6 Reconstructed two-dimensional beam intensity profiles of the 25th harmonic beam. The spectrally resolved 2D profile of generated XUV beams can be reconstructed by translating the spectrometer while recording the spectrogram. (a) Measured beam profile without going through the XUV polarizer. (b-d) Projected intensity profiles for different linear bases. By changing the relative angle (b) 0°, (c) 45°, (d) 90° between the vector beam generator and the XUV polarizer, we measure the intensity distribution of 25th harmonic beam after going through the XUV polarizer. Driven by the designed vector fundamental beam, the generated XUV radiation consists of both s- and p-polarized components shown in (b) and (d). The intensity does not vanish at bright spots, while changing the relative angle between the polarizer and polarization of the beam. (c) When the relative angle is set to 45°, modulation appears in both vertical and horizontal directions.

When we change the waveplate angle, the intensity will never vanish at the position of bright spots shown in Fig. 4-6(a). This shows the XUV field has nonzero component in every direction and is consistent with the behavior of a circular/elliptical polarization state. Fig. 4-6(c) shows the intensity profile when the polarizer is oriented at 45°. The intensity profile has a similar multi-spot structure to that in Fig. 4-6(a), and all segments transmit through the XUV polarizer. The interferometric modulations occur in both vertical and horizontal directions, since radiation from all four generating segments can be equally transmitted through the XUV

polarizer. This intensity profile also disproves the linear polarization at those segments, since adjacent segments would have orthogonal -45° polarization and would not transmit through the 45° XUV polarizer.

If the relative angle reaches to 90°, the transmitted intensity shows vertical fringes, as in Fig. 4-6(d), which is similar to the 0° case but in an orthogonal direction. These fringes come from the interference between the left/right segments, which are horizontally displaced in space. The signal-to-noise ratio is degraded in these measurements due to the scattering and low reflectance of the silver mirrors in the XUV polarizer. Figs. 4-6(b,d) depict the intensity distribution when the vector XUV beam is projected to the orthogonal linear basis. This again illustrates, at the intersection of these two sets of fringes, the bright spot of the XUV beam has both orthogonally polarized linear components.

Next, we turn to the phase relation in the XUV vector beam and confirm experimentally the opposite handedness of adjacent bright spots. For our measurement, we employ a linear reference XUV beam, produced by a separated and more tightly focused high-harmonic source. This reference XUV beam interferes with the vector XUV beam we generate, shown in Fig. 4-7(a), over its whole transverse profile. We can control the polarization of the reference XUV beam with a half-wave plate acting on its fundamental, since the generated XUV beam has the same linearly polarized state as its driving field.

In the relative phase measurement, we fix the position of the XUV spectrometer and allow only two vertically displaced adjacent XUV segments to pass through the spectrometer slit. They are identified by the two boxes in Fig. 4-7(b). Then we use the linear reference XUV beam to interfere with the two transmitted segments. The blue and green curves in Fig. 4-7(b) show the interferences when the reference XUV beam is p- and s-polarized, respectively. If the two segments have the same handedness, then the modulation in each segment will line up for both polarizations. If they have opposite handedness, then there will be a phase shift of one cycle with respect to the other. In the figure, we see that the intensity is modulated vertically as expected. The dashed red lines in Fig. 4-7(b) reference the peaks of modulation periodicity.

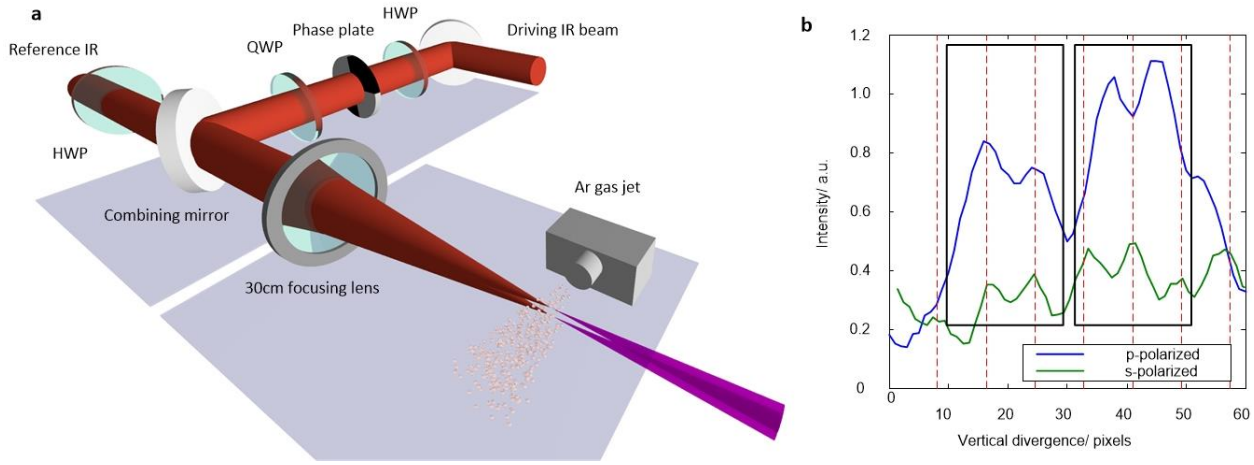

Fig. 4-7 Measuring interference between an XUV vector beam and a linear polarized XUV reference beam. (a) Experimental setup. The polarization of the reference beam is controlled by a half-wave plate (HWP) for the fundamental. The XUV beams are spectrally resolved and spatially overlapped in an XUV spectrometer. The interference images are recorded by the micro-channel plate (MCP). (b) Interference between the XUV reference and vector beam. The blue curve shows the fringes when the reference beam is p-polarized, and the green curve shows the fringes when the reference beam is s-polarized. The dotted red lines indicate periods of the modulation. All the red dotted lines aligned with all the peaks of the green curve, which indicates the s-component at intersections are all in phase. For the p-component shown with the blue curve, either the peaks or the valleys are aligned with the red dotted line, and that indicates p-components at intersections that are out of phase with respect to the adjacent one.

When the reference beam is s-polarized (green curve), all peaks are aligned with the reference lines in both left and right boxes. In the case of p-polarized interference, the peaks are in-phase with the dashed reference lines in the left box and out-of-phase in the right box. This shows that the p-polarized components have a π-phase jump between the adjacent spots. The in-phase s-component and out-of-phase p-component cause counter rotating polarization between the two segments. With this measurement, we can perform phase sensitive optical tomography on the vector XUV beam along two orthogonal polarization bases.

4.4 Discussion and implications

The ability to control the spatial mode of the driving beam enables us to generate more complex beams by engineering their transverse profile. The phase retardation can be designed by patterning different phase structures on the liquid crystal plate, while the polarization of XUV can be changed by changing the driving polarization. In this case, the high harmonic generation process provides access to transferring the spatial manipulation to XUV beams. Such manipulation is not only limited to the 2D transverse plane but can be extended to 3D

space while the beam is propagating and transforming. The generation of complex polarization states will enable increasingly capable table-top XUV sources to probe the dynamics of polarization sensitive systems [123].

One important application of circularly polarized XUV is the sensitivity of magnetic domains or chiral molecules to the handedness of light. Currently, both the structure and dynamics of magnetic domains are measured with circularly polarised harmonics created by manipulating the sub-cycle time structure of the fundamental beam. Specifically, these experiments use a driving beam composed of counter rotating light at the fundamental frequency and its second harmonic [120].

Using the spatial structure of the fundamental rather than the time structure has potential advantages. The monochromatic driving field leads to a higher cut-off energy, which is mainly limited by the damage threshold of the liquid crystal plate, as required by the $3U_p$ cut-off law [30,33,156,162] under a same ionization rate. Expanding the beam size on the liquid crystal plate or deploying water cooling system will increase the damage threshold. The extended cut-off that the vector beam approach appears to offer will be important for high photon-energy probes. Structuring the spatial mode of single laser beam provides a paraxial geometry that generally favors phase matching. The interaction length will be limited by the variation of the polarization state and accumulated phase during propagation if the thickness of the interaction medium is significantly increased compared to the Rayleigh length.

In addition, the polarization remains linear in the region where intensity is highest in our approach. This results in a higher fraction of the energy that can produce high harmonics relative to polarization gating in temporal domain. We determined the fraction of the energy that can produce high harmonics by turning on and off the ellipticity dependence in the semi-classical simulation.

(1) We assumed that the intensity remained the same, but the polarization was linear, and we calculated the single atom conversion efficiency.

(2) Then we used the actual vector beam polarization profile and performed the same calculation.

The excursion of the electron is calculated by classical trajectory in the presence of the laser field. The spread of the wave packet is estimated by its perpendicular velocity [163].

Then the yield is calculated "point by point" as a function of local intensity and helicity at the focal plane. The laser parameters are 50 fs pulse, 3×10^{14} W cm^{-2} peak intensity interacting with argon gas. Fig. 4-8 shows the 25th harmonic yield when the local fields are artificially turned into linearly polarized. Fig. 4-8 shows when the helicity is included. Harmonics are only generated from the four lobes where the polarization is near linear (and the intensity is strongest). No harmonics are produced where the polarization is elliptical or circular (and the intensity is low).

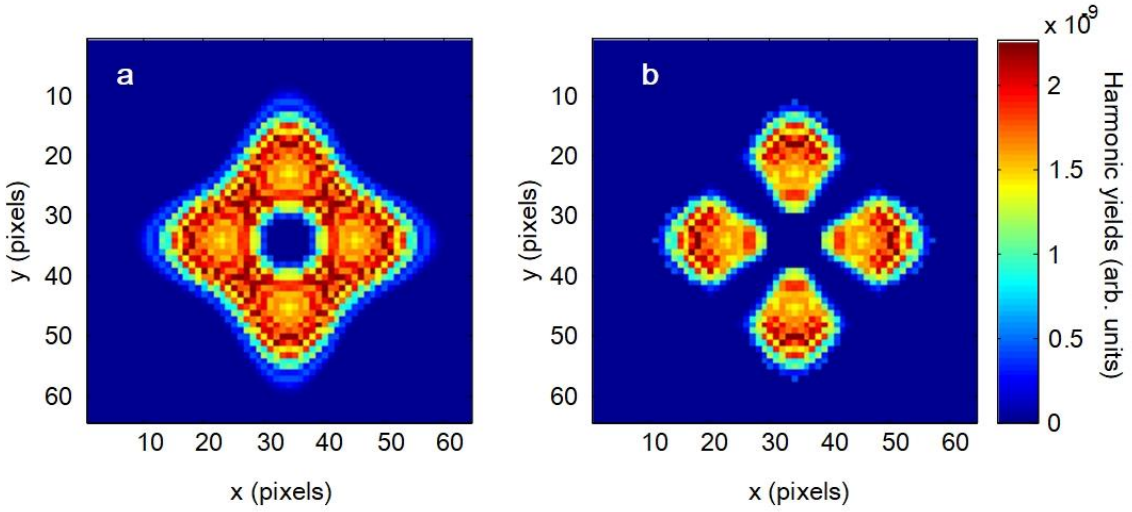

Fig. 4-8 25th harmonic yields in the near field. (a) the 25th harmonic yield in the near field when the field is all linear. (b) the 25th harmonic yield in the near field after the polarization shaping. The harmonics are only produced where the field is high, and polarization is closed to linear.

With respect to the fraction of the energy that can produce high harmonics for different orders due to polarization shaping, we divide the total high harmonic yield in the right Fig. 4-8(b) by that in the Fig. 4-8(a) for each different order. Then the ratio versus the harmonic order is plotted in Fig. 4-9. We can see that, as the order goes higher, the yield is more sensitive to the ellipticity and therefore the fraction of the energy that can produce high harmonics is lower.

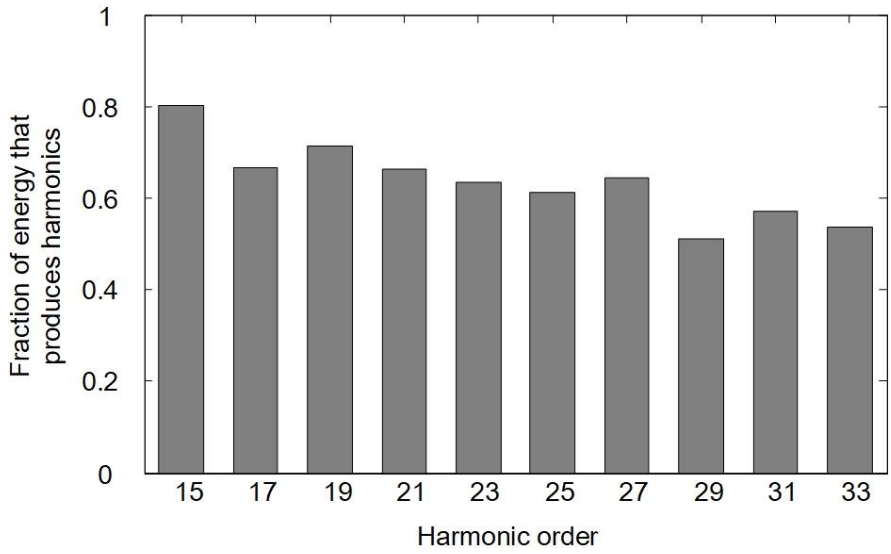

Fig. 4-9 The fraction of the energy that can produce high harmonics of spatial polarization shaping. Comparing to the linearly polarized driving laser field, the fraction of

the energy that can produce high harmonics gradually reduces as the order of harmonics goes higher.

This approach can be considered as a spatial analogy to the temporal domain polarization gating. While temporal polarization gating works, a fraction of the laser energy is wasted since there is no HHG when the polarization is not nearly linear. In the temporal polarization gating, more than half of the energy is wasted, since the main peak of the electric field is elliptically polarized and only half cycle field (even not the strongest one) is used to produce high harmonics. In the spatial case, the flexibility of designing the phase pattern ensures that most energy goes into linearly polarized regions. Fig. 4-9 illustrates a promising efficiency that more than half of the energy is used to produce high harmonics in the spatial polarization gating.

To conclude, shaping the polarization of fundamental beam takes the use of the spatial dimensions and expand the capability of producing complex XUV beams. As we demonstrated in this chapter, three spatial dimensions (two transverse and one longitudinal) contribute to the mode evolution of fundamental and XUV beams. The evolution enables the production of circular polarized at XUV wavelength and overcomes the low yield in the frequency up conversion.

High harmonic vector beams such as these are ideal for probing circular dichroism [123,164] as they can simultaneously provide counter rotating circular polarization states at XUV wavelengths. The spatial separation of circularly polarized spots permits the isolation of one particular state by spatial filtering. Together with the inherent temporal resolution of high harmonic sources, this technique may be used to study how magnetic domains can be switched. This result also proves the capability of using the spatial properties of vector driving beams to generate high harmonics with novel complex spatial profiles. That is, it leads to another degree of freedom which we can design and engineer for tabletop harmonic based XUV sources.

Chapter 5 Spin assisted angular momentum control in high-harmonic generation

In the previous chapters, we show that controlling phase front and polarization in strong field interaction extends the capability of high harmonic sources. The structured beams create XUV radiation with special properties, for example spiral wave front and circular polarization, which are hardly achievable with conventional harmonic-based light sources. The interactions also reveal the conservation law of angular momentum, as the polarization and the phase front are associated with the spin and the orbital angular momentum of photon respectively. These two parts of the angular momentum of photon are closely related and classically the different polarization states can be projected on to a same set of orthogonal bases with different phase terms.

In this chapter, we would like to show how these two parts of angular momentum can influence each other in the high harmonic generation process, while we shape both the polarization and the phase front. The interplay between spin and orbital angular momentum in the up-conversion process allows us to control the macroscopic wave front of high harmonics by manipulating the microscopic polarizations of the driving field. We demonstrate the control of orbital angular momentum in high harmonic generation from both solid and gas phase targets using the selection rules of spin angular momentum. The gas phase harmonics extend the control of angular momentum to extreme-ultraviolet wavelength. We also propose a bi-color scheme to produce spectrally separated extreme-ultraviolet radiation carrying orbital angular momentum.

5.1 Spin and polarization control in high harmonic generation

Manipulating the phase front and the polarization of an optical beam have garnered great attention in the optics and quantum research. For example, as we introduced in Chapter 3, the wave fronts of Laguerre-Gaussian modes have a spiral shape, and are linked to the OAM of photons [75]. Due to the limitation of available optics [165,166], shaping the wave front of extreme-ultraviolet or soft X-ray radiation is challenging, despite demand for these wavelengths in microscopy, spectroscopy and lithography applications [24,167,168]. As we demonstrated in Chapter 3, nonlinear frequency conversion under non-perturbative conditions provides a feasible route to control or transfer structured wave fronts to the XUV and even X-ray regions. By pre-shaping the driving optical field, the phase spirals that define the OAM can be imparted to the generated frequencies through a noncolinear wave mixing [118]. The beams carrying different orbital angular momentum are emitted at different diffraction angles. Similarly, the local polarization or the spin angular momentum (SAM) of the XUV field can also be controlled by engineering the polarization of the incident driving fundamental beam [120,169,170]. The circularly polarized XUV beams are a source for polarization sensitive measurements of inner shell electrons in materials and determining chiral molecules [123,171,172].

Previous experiments show that, on their own, the spin and the orbital angular momentum are conserved during the nonlinear conversions in both perturbative [173–175] and non-perturbative regimes [74,121] under paraxial conditions. These experiments either modify the polarizations or the wave fronts of the driving laser beams, while keeping the other part uniform or planar. Such 'pure mode' configurations concentrate on studying the behavior of either the spin or the orbital angular momentum during the nonlinear conversion and deliberately eliminate possible influences from the other part of the angular momentum. So far, however, there has been little discussion about the interplay between these two types of angular momentum in high-order nonlinearities, which would allow us to further control the angular momentum in desired wavelengths.

5.2 Shaping both the polarization and phase

Instead of using a driving beam with a single spatial mode or a uniform polarization state, we manipulate both the spin and orbital angular momentum of the driving beam using one mode to control the other. In this specific case, the spin selection rule eliminates the channels that could lead to higher OAM state [74,118], confining the OAM of the high harmonics to that of the fundamental, in this case ±1 unit. This interplay between the spin and orbital angular momentum during up-conversion allows us to control the macroscopic wave front in the short wavelength radiation by manipulating the microscopic polarization of the driving field.

The experiments are performed with both solid and gas targets. The solid target gives us access to both above and below bandgap harmonics, which can easily be manipulated and measured with conventional optics due to their low frequency. Harmonics generated from noble gases, on the other hand, allow this technique to be transferred to much higher frequencies. We will show that the results for photon energy ~42 eV are consistent with a beam with OAM values l equal to ±1.

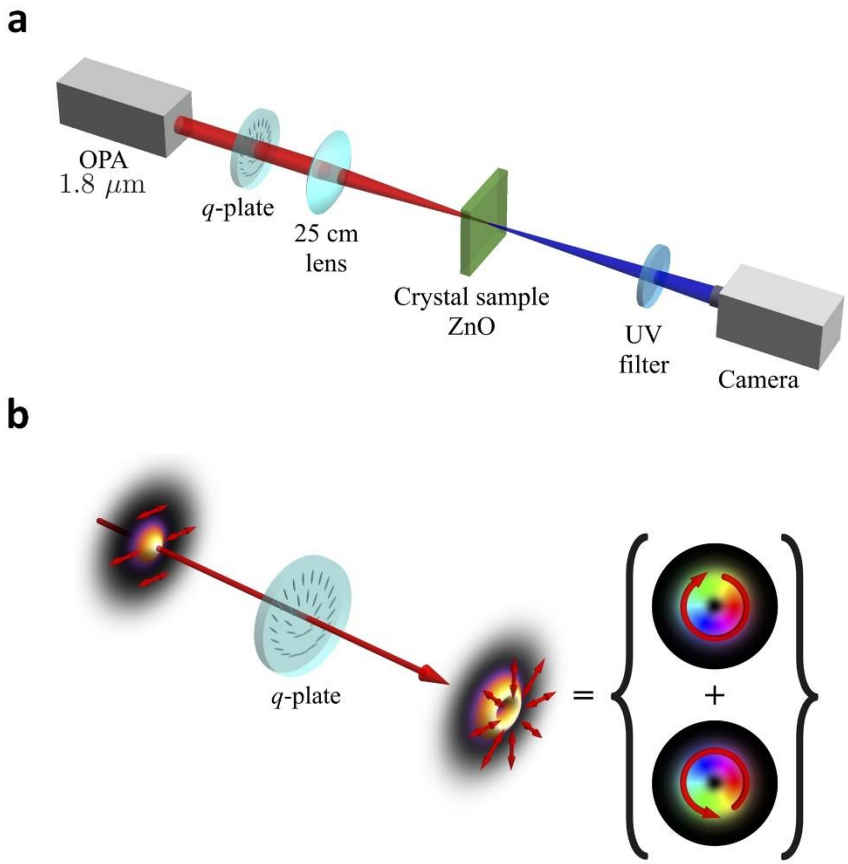

Fig. 5-1 Generating high-order harmonics under non-perturbative conditions. (a) The experimental setup of generating structured high-harmonic beams from a solid crystal target (b) A Gaussian beam is converted by a *q*-plate into a superposition of Laguerre Gaussian modes with opposite circular polarization states.

In this experiment a laser beam (with a duration of 50 fs, center wavelength of 1.8 μm for ZnO crystal and 800 nm for argon gas) generates harmonics in a solid or gas-phase target (Fig. 5-1(a)). We shape the spatial characteristics of the beam with a *q*-plate that can change the polarization (or phase) of the incident laser beam [69,95,159] point by point across the beam profile. After passing through the *q*-plate, the 1.8 μm beam in $LG_{0,0}$ mode is converted to a superposition of $LG_{0,1}$ and $LG_{0,-1}$ modes [176], as illustrated in Fig. 5-1(b). These two modes have opposite circular polarization, corresponding to two eigenstates of SAM, and their superposition results in a radially polarized beam with a zero intensity at its center. The fundamental beam with ~20 μJ pulse energy is then focused by a 30 cm lens to reach ~1 TW cm^{-2} on the crystal surface.

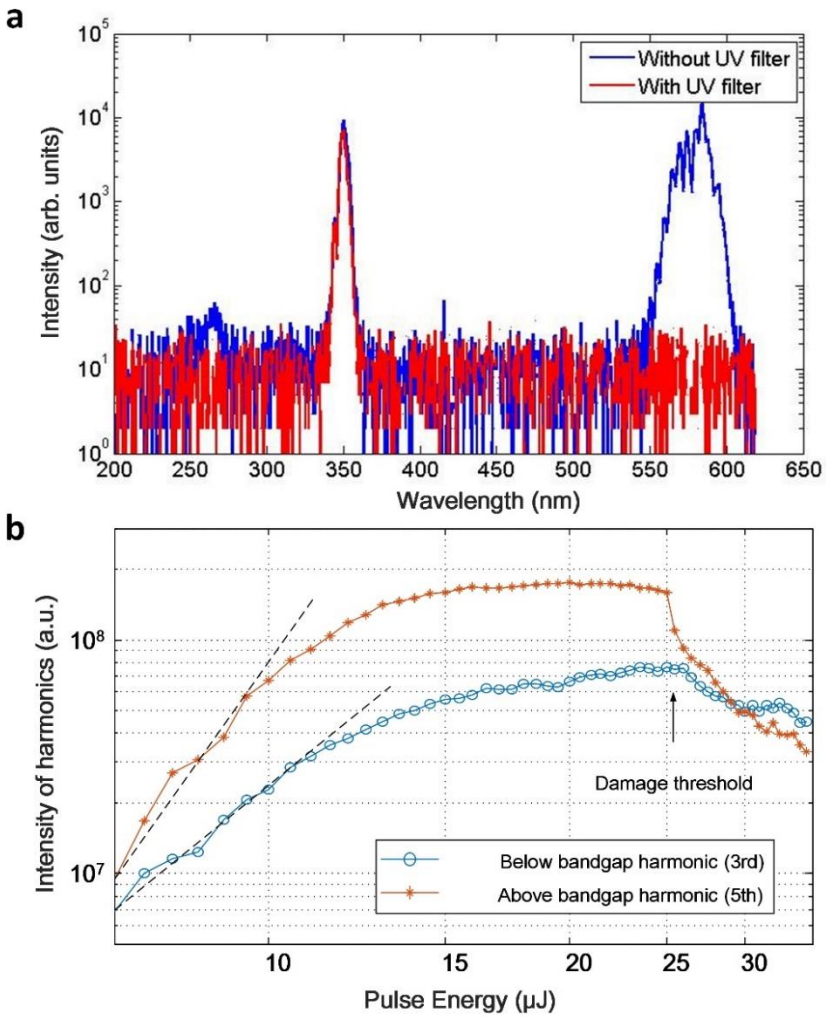

Fig. 5-2 Characterization of 3rd and 5th order harmonic emission. (a) The optical spectrum of the 3rd and 5th harmonics measured with and without the UV filter a bandpass filter with a passband from 250 nm to 400 nm is used to isolate the 5th order harmonic signal from the 3rd order harmonic signal. (b) Intensity of scaling of harmonics yields with respect to different pulse energy of the driving laser pulse. The dashed lines indicate the 3rd and 5th power intensity scaling versus the pulse energy. The damage threshold is the turning point of the intensity curve where the harmonic signal significantly decreases.

Ocean Optics Maya UV fiber spectrometer records the optical spectrum of the harmonic beams generated from ZnO crystal. Both the 3rd and 5th harmonic of the fundamental beam peak at 350 nm and 580 nm, shown in Fig. 5-2(a). In the experiment, a band pass filter with a pass band from 250 nm to 400 nm is inserted to isolate the 5th order harmonic signal from the 3rd order harmonic signal, so that we can characterize the 3rd and 5th harmonic beams individually.

Harmonics can be generated within either the perturbative or non-perturbative regions before irreversible damage. In the perturbative region, electrons are mostly confined in bounded state and introduced time-dependent polarizability in response to the external field. The anharmonic

potential gives rise to the optical harmonic emission. The yield of the harmonic is scaling proportional to I^n, where I is the intensity of the driving laser field and n is the harmonic order [45]. This scaling rules does not apply in nonperturbative region when the intensity of the laser beam is high, and recombination of electron is involved in the harmonic generation process. Therefore, the two different mechanisms can be distinguished by intensity scaling (Fig. 5-2(b)) where both the 3rd and 5th harmonics no longer retains its 3rd and 5th power law behavior (shown as the black dashed lines in Fig. 5-2(b)) [177]. The results presented in this chapter are all obtained under the non-perturbative condition.

When the intensity of the driving laser beam exceeds the damage threshold of the crystal and damage spot is observed on the crystal surface. The harmonic signal drops dramatically as shown in Fig. 5-2(b). This drop of harmonic signal is irreversible in contrast to the nonperturbative saturation.

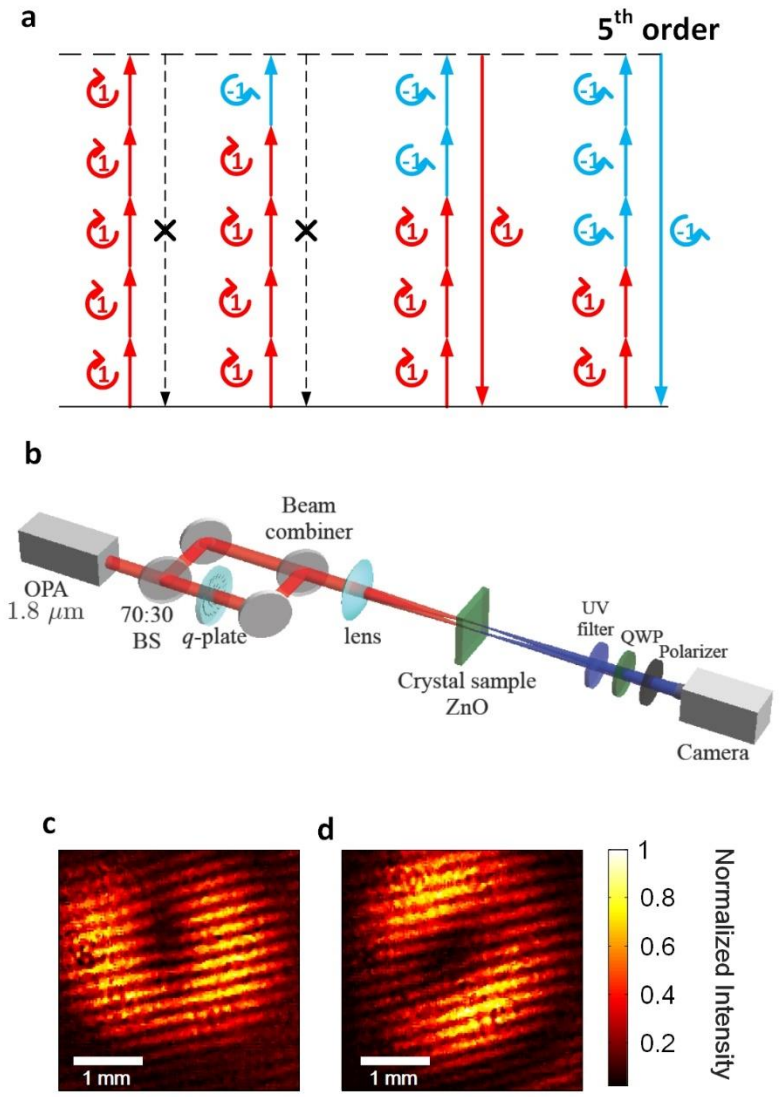

Fig. 5-3 Control of OAM on high-order harmonics by selection rules of SAM. (a) The allowed and forbidden transitions in multiphoton process plotted in energy diagram. (b) The experimental setup of generating structured high-harmonic beams from a solid crystal target and interferometric characterization of the OAM on the harmonic beams. (c) The experimentally observed interference pattern between a reference beam and a left handed circularly polarized OAM carrying beam with l = -1. (d) The experimentally observed interference pattern between a reference beam and a right handed circularly polarized OAM carrying beam with l = +1.

During harmonic generation, energy conservation requires that the number of fundamental photons involved in producing harmonics must equal the harmonic order. For instance, in 5th order harmonic generation shown in Fig. 5-3(a), five fundamental photons are absorbed and

produce one ultraviolet photon emitted at 360 nm. This emitted ultraviolet (UV) photon can only have two possible spin eigenstates, $s = +1$ and $s = -1$, where s is the quantum number of SAM. Therefore, only two possible channels are allowed: either absorbing two left ($s = +1$) and three right circularly polarized photons ($s = -1$), or three left ($s = +1$) and two right ($s = -1$), as shown in Fig. 5-3(a) on the right. Any other combinations, for example those shown on the left, are forbidden, since the final SAM of the UV photon cannot satisfy the condition $\langle s \rangle \leq 1$ when spin is conserved.

The total OAM of the emitted harmonic photons for the two allowed processes equals to the sum of OAM from all involved fundamental photons. In this case, the OAM value for the two processes can only be $l = +1$ and $l = -1$, respectively, where l is the quantum number of the OAM states. In other words, the OAM of the harmonics equals the OAM of the fundamental. It is the bounded spin states and conservation of angular momentum which selects the OAM value of harmonics.

To show that the OAM value of each circularly polarized state is constrained by the spin selection rule, we use a combination of a quarter-wave plate and a linear polarizer to serve as an analyzing element for circular polarization [178]. Since these two optical components do not change the topology of the wave front, the OAM quantum number can be measured by interference with another plane wave sharing the same polarization state [179]. The reference plane wave is coherently created by an independent source from the solid target without wave front shaping.

In experiment a linearly polarized Gaussian reference beam is focused onto the same ZnO sample. The focus of this reference beam is 200 μm spatially apart from structured beam focus. This reference beam produced both 3rd and 5th harmonics which are both linearly polarized with a planar wave front as shown in Fig. 5-3(b). The structured and the reference harmonics interference in the far field and the interference pattern reveals the wave front information of the structured beam. To resolve the wave front on two different circularly polarized states, a quarter waveplate and a broadband linear polarizer is used to serve as a circularly polarizer. It is worth noticing that when combining the reference beam and structured beam, a nearly normal incident geometry is preferred since the structured beam has non uniform polarization.

Fig. 5-3(c,d) show the interferometric results of the $s = +1$ and $s = -1$ state 5th harmonics – above-bandgap harmonics for ZnO. Both results show a fork-shaped pattern and opposite orientations between two circular polarized states. The beam's OAM value can be read from different numbers of fringes from left side of singularity point to its right side. The OAM values on the $s = \pm 1$ components are $l = \mp 1$, respectively, which correspond to the OAM of the fundamental beam.

It is possible for the SAM of the optical beam to be transferred to the crystal lattice [180,181], depending on the rotational symmetry of the crystal sample. In this experiment with (0001)-cut free-standing ZnO, such an effect is not excluded. However, the measured harmonic yields from these channels are below the noise level in the measurement, which are at least two orders-of-magnitude weaker than the channels shown in Fig. 5-3(a) that do not exchange SAM with the crystal lattice. Therefore, the higher order OAM states are negligible, and the $l = \pm 1$ state dominates the harmonic output.

Symmetry-enabled channels that lead to higher-order OAM modes may be revealed in other strongly coupled systems. For such processes to be important, the material should exhibit an anisotropic harmonic yield with varying orientation of a linearly polarized driving field [170,182].

As a superposition of two equally intense circular states, the driving field is locally linear everywhere at its focus. Thus, the generated harmonic beams should maintain the radially polarized structure of the driving beam. The polarization singularity forces a zero intensity at the beam center as shown in Fig. 5-4(a).

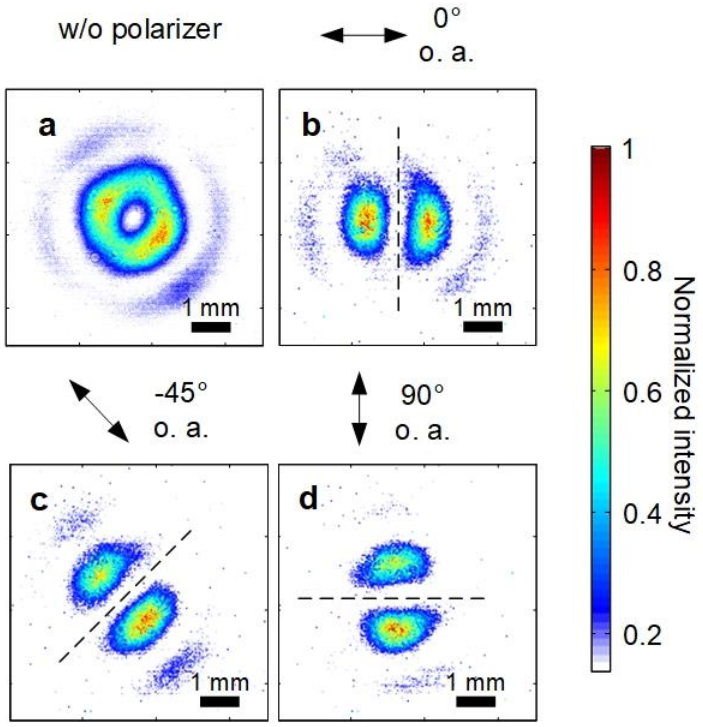

Fig. 5-4 Characterization of polarization states of high-harmonic beams from ZnO crystal using a linear polarizer (a) Intensity profile of generated 5th harmonics from ZnO target. (b-d) The intensity profiles of 5th harmonic beams from ZnO, with wavelength of 360 nm, after passing through a linear polarizer with its optical axis angle placed at 0°, -45° and 90°, respectively.

To confirm the polarization of the generated harmonic beam, we measure the polarization of the 5th harmonic beam using a linear polarizer, a UV band-pass filter and a UV enhanced camera. The intensity profiles of the 5th harmonic after passing through the linear polarizer are shown in Fig. 5-4(b-d) where we have oriented the linear polarizer at 0°, -45° and 90°, respectively. The bright lobes rotate as we change the angle of the linear polarizer. The horizontal/vertical parts of the beam are observed when the optical axis of the linear polarizer is placed horizontally/vertically. This is consistent with the characteristic of a radially polarized beam. From an interferometric point of view, in circular-state bases, the linear

polarizer selects a common linear component from the two circular states and lets them interfere collinearly on the camera. The two bright lobes in their intensity illustrate $2\times2\pi$ phase shift between left and right circular states in the azimuthal direction. This confirm the analysis that one unit of OAM is imparted to the 5th harmonics with opposite signs between the two spin states.

5.3 Towards a shorter wavelength

To reach higher photon energies, we extend the above experiment to a gas-phase target and a much higher intensity. With a noble gas, the effect of transferring SAM to the nonlinear medium is also eliminated, due to the rotational symmetry of the gas atoms [181]. The only possible OAM values on any harmonics are $l = \pm1$.

In the experiment, we use the optical pulse from Ti:Sapphire laser at 800 nm with 50 fs duration and 0.8 mJ energy to produce high harmonics from argon gas. The experiment setup is shown in Fig. 5-5. The pulse is shaped by a *q*-plate just like the beam in the previous section which is used for harmonic generation on solid. The interaction with argon gas jet produces high harmonic emission extends to the 29th harmonics of 800nm with photon energy of ~45 eV. The gas jet is 200 μm thick with a backing pressure at ~5 bar.

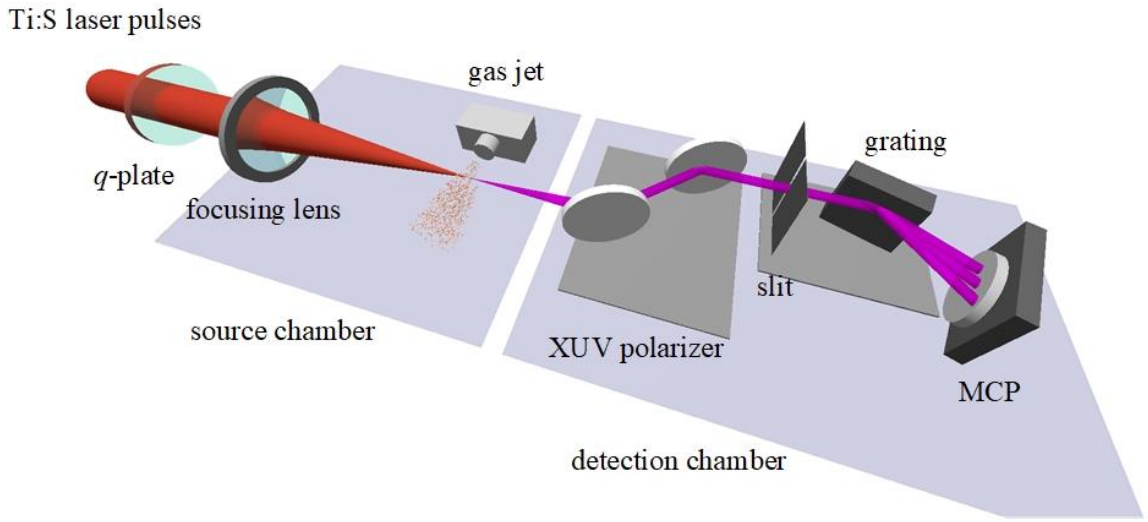

Fig. 5-5 The experimental setup for producing spin-constrained high harmonic vortex beams. The driving pulse is the optical pulse from Ti:Sapphire laser at 800 nm with 50 fs duration and 0.8 mJ energy. The pulses interact with argon gas and produced high harmonic up to the 29th harmonics. The generated XUV radiation is propagated into the detection chamber where the beam profile is recorded XUV spectrometer, which consist of a 100 μm wide slit, a XUV imagining grating and micro-channel plate (MCP). An XUV polarization, which is consist of a pair of paralleled mirrors is inserted before the XUV spectrometer, so that the detection apparatus has polarization selectivity at XUV wavelength.

The harmonic emission from the gas reproduces a doughnut-shaped intensity distribution from the driving beam, which is shown in Fig. 5-6(a). The image is recorded directly by a micro-channel plate without passing through dispersive element, to eliminate the polarization selectivity from the measuring system. Therefore, the intensity distribution is an intensity summation of all high harmonics.

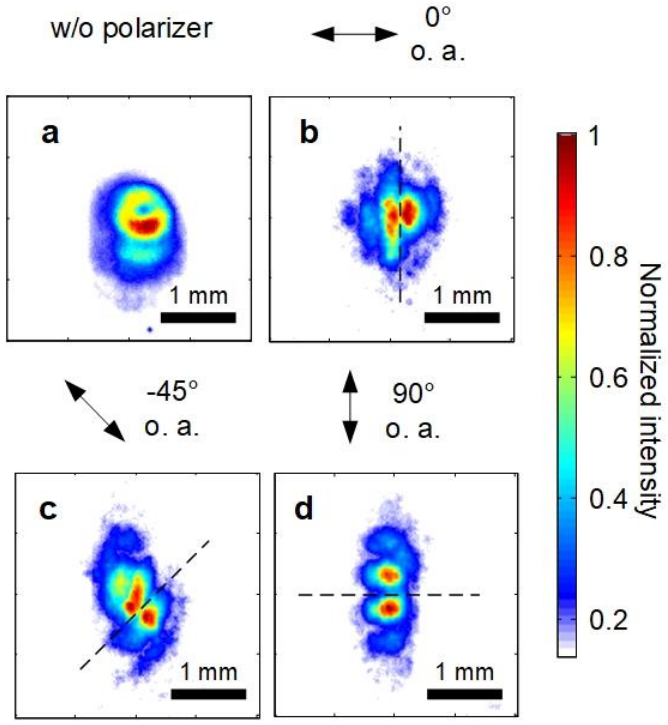

Fig. 5-6 Characterization of polarization states of high-harmonic beams from argon gas target using a XUV linear polarizer. (a) Intensity profile of generated high-order harmonics from argon gas target. (b-d) The intensity profiles of 27th harmonic beams from argon gas, with wavelength of 30 nm, after passing through a linear polarizer with its optical axis angle placed at 0°, -45° and 90°, respectively.

However, it is not trivial to separate the two superimposed circularly polarized beam at XUV wavelength and measure their OAM value separately, as with solid target. To link the result from gas and solid targets, we replace the linear wire grid polarizer used for solids by a pair of silver mirrors [161]. The generated high harmonics are passed through both the mirror pair and the XUV imaging grating before detected by the micro-channel plate. The polarization selectivity of the mirror pair and the grating is ~10:1, and the mirror pair act like an XUV polarizer as we introduced in Chapter 4. Instead of rotating the mirror pairs, we rotate the incident beam to change the optical axis of the linear polarizer. As shown in Fig. 5-6(b-d), we see two nodes orient along different angles as we rotate the driving laser beam. This is the same behavior as we reported in Fig. 5-4(b-d) for a solid target, and it indicates that controllable OAM is also transferred to XUV wavelength.

Controllable OAM (or structured polarization states) of short wavelength radiation will result in tighter optical focusing [183], excite inner shell dynamics [184] and probe ultrafast magnetic dynamics [153]. This study contributes to this growing area of research by exploring the relation between the spin and orbital angular momentum in the up-conversion process under strong field condition. Furthermore, we show the potential of solving control problems by linking the two components of the angular momentum. The topological charge is constrained to be equal to that of the fundamental beam. It can, therefore, be easily manipulated by the conventional optical elements [74,118]. In addition, the collinear geometry and locally linearly polarized driving field ensures efficient conversion to the harmonic emission, which is crucial for the development of a light source.

To further decouple two superimposed circular states at XUV wavelength, we propose a bi-color driving approach to isolate high harmonics beam with controlled OAM. In that case, the driving field would consist of a fundamental OAM beam with l = +1, s = -1 and a second harmonic beam with l = -1, s = +1. According to the conservation of SAM, there are only two allowed channels for high harmonic generation, as shown in Fig. 5-7. Different from the scheme driven by a single-color field, the emissions from these two channels corresponds to 7^{th} and 8^{th} harmonic generation. In other words, the two OAM modes are decoupled in energy. Classically, the mixing of the two-color field will result in a 3-fold symmetric driving field, with a re-collision happening every third of a period [121]. Since the two beams carry different phase front spiral, the 3-fold trajectories rotate their orientations by 2π along azimuthal direction. This geometric phase gives rise to the phase-front spiral of the generated high harmonics.

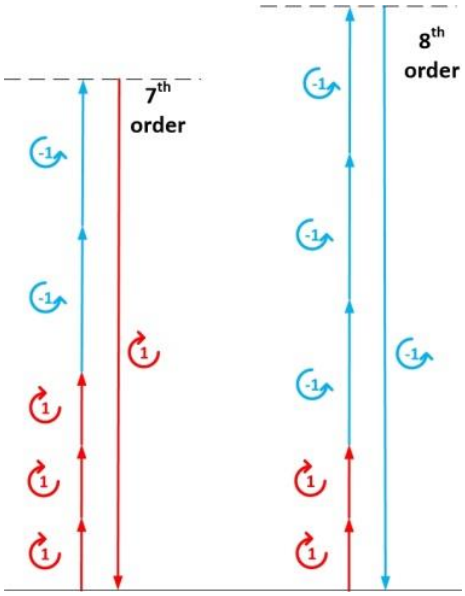

Fig. 5-7 The energy diagram of spectrally decoupled OAM mode in high-order harmonics. Two allowed 5-photon processes in the two-color scheme is split into 7^{th} and 8^{th}

harmonics in spectrum, whereas the emitted photons are energy degenerate using the same color driving field.

In this experiment, both spin and orbital angular momentum are conserved on their own, since the medium that we are interacting with is nearly isotropic and the focusing geometry of the driving laser beam is paraxial. However, exploring the interaction, for example in waveguide or tightly focused geometry [185,186] where spin and orbital angular momentum can be coupled, may lead to even more complex behavior. Just like other fundamental particles, photons exhibit spin-orbit coupling when interacting with matter. The coupling not only exists between spin and orbital angular momentum, as we mentioned above, it can also happen between the photons and crystal/electronic structures. A strongly coupled solid-phase system may help create electro-optic devices that respond to the polarization and wave front of incident light, or new optical sources, such as polarization/spin controlled soft X-ray for magnetically sensitive probing.

Chapter 6 Generating few-cycle cylindrical vector beam

Compressing optical pulses to a shorter time duration is continuous pursued by researchers in the field of ultrafast optics. Recent progress has permitted the generation of light pulses compressed to only a few oscillation cycles of the optical fields. As strong field interactions are often associated with the electron response to the field of driving laser pulses, and emitted photons or electrons are sensitive to the carrier envelope of the field. These field-sensitive effects become significant with few-cycle pulses due to its rapid rise time. By controlling the carrier envelop phase, few-cycle light pulses permit control of the two trajectories of freed electrons in strong-field interactions on a time scale of the light oscillation period. Its rapid rise time also enables unprecedented ultra-intense field to interact with electron system without depleting the ground state population.

In the spatial domain, a radially polarized beam is able to produce tightly focused light fields beyond the Gaussian beam diffraction limit. However, with current technology its duration is limited by the relatively narrow bandwidth that generation techniques can support. Generating pulses which have both ultimate temporal and spatial compressibility has to overcome the bandwidth limit in mode conversion. This chapter tackles this problem by performing nonlinear compression with a spatial structured beam.

Using a 10-cycle pulse with a central wavelength of 1.8 μm, we show that radially polarized beams can be compressed to the few-cycle regime while still maintaining their radially polarized nature. It, therefore, seems feasible, using only well-developed methods, to reach focused intensities of ~10^{19} W cm^{-2}. Conversion via high harmonic generation will also open a route for applications in attosecond science, especially for a wide range of optical measurements and optical control that require high spatial and temporal resolution.

6.1 Generating polarization structured beam

Vector beams are laser beams with a non-uniform polarization structure across their profile and a subclass of them has an intensity and polarization profile that is cylindrically symmetric [96]. An important characteristic of a tightly focused radially polarized beam, for example, is that it forms a smaller focus spot than what can be achieved with a comparable beam of either linear or circular polarization [98,183].

Many methods produce cylindrical vector beams, especially radially and azimuthally polarized beams. There are intracavity devices [187] for lasers that efficiently convert a conventional single mode Gaussian laser beam into one with a different polarization distribution [188,189]. However, these devices always have a relatively narrow bandwidth.

In all areas of ultrafast science, pulses can be amplified or shaped up to the bandwidth limit of the most narrow-band processes involved, and then compressed by self-phase-modulation in a nonlinear medium – often a fiber. This is how the high power few-cycle pulses used for attosecond science are created [190]. This method can also create single-cycle pulses in the visible or near infrared [191,192]. Optical pulse compression by self-phase modulation is a critical element in all ultrashort pulse lasers [193]. In fact, optical continua can even be

generated by self-phase modulation in fibers with noble gases [17,194]. In all of these cases, the final pulse duration can be much shorter than what the bandwidth restriction might imply.

This chapter aims to show that pulse compression is available for cylindrically symmetric vector beams. Pulse compression will greatly expand the application area of these beams.

For our experiment, we have chosen a radially polarized beam that we generate using a linearly polarized Gaussian beam propagating through a *q*-plate [69] and we find very similar results for azimuthal polarization. We will show that the *q*-plate has a bandwidth limit that is insufficient to create a few-cycle pulse. However, once the pulse is shaped and spatially filtered to ensure its cylindrical symmetry, we will show that it can be compressed down to a few-cycles by means of a conventional gas-filled hollow-core fiber compressor.

We use a 1.8 μm beam produced by the laser source which consists of a chirped-pulse-amplified Ti: Sapphire laser system and a white-light seeded high-energy optical parametric amplifier (HE-TOPAS, Light Conversion) [195]. The Ti: Sapphire laser system that we used provides 50 fs laser pulses at 800 nm with a 5 mJ pulse energy at a repetition rate of 1 kHz. The optical parametric amplifier is pumped by the 800 nm light and it provides 1.8 μm pulses with ~50 fs duration. The 1.8 μm pulses from the OPA are spatially cleaned by focusing into a hollow-core fiber (1.4 m long, 400 μm core diameter) with an f = 75 cm lens made of CaF2, as shown in Fig. 6-1.

We use a *q*-plate (q = 1/2) for generating a radially polarized beam [69]. A *q*-plate is composed of two ITO substrates covered by a polyimide layer (50 nm thick PAAD22 from BEAM Co.) and a liquid crystal layer (NLC 6CHBT LC). The ITO substrates are spin coated by polyimide on single side. The liquid crystal is then injected in between the coated sides of the two substrates. The alignment pattern of the liquid crystals in the *q*-plate is 'written' during its fabrication.

Its liquid crystals' optical retardation is controlled through an external electric field which is applied on the plate. Therefore, the device's central wavelength can be tuned by simply adjusting the applied voltage. The center wavelength of the OPA output is 1.8 μm, which has the negative dispersion in fused silica to compensate the chirp induced by spectral broadening in the hollow core fiber. However, ITO substrates can be absorptive for the wavelengths longer than 1 μm depend on the deposition process. In fabricating *q*-plate for 1.8 μm, we use CEC 100S ITO glass substrate from Präzisions Glas & Optik GmbH, which maintains over 80% transmission up to 2.5 μm radiation.

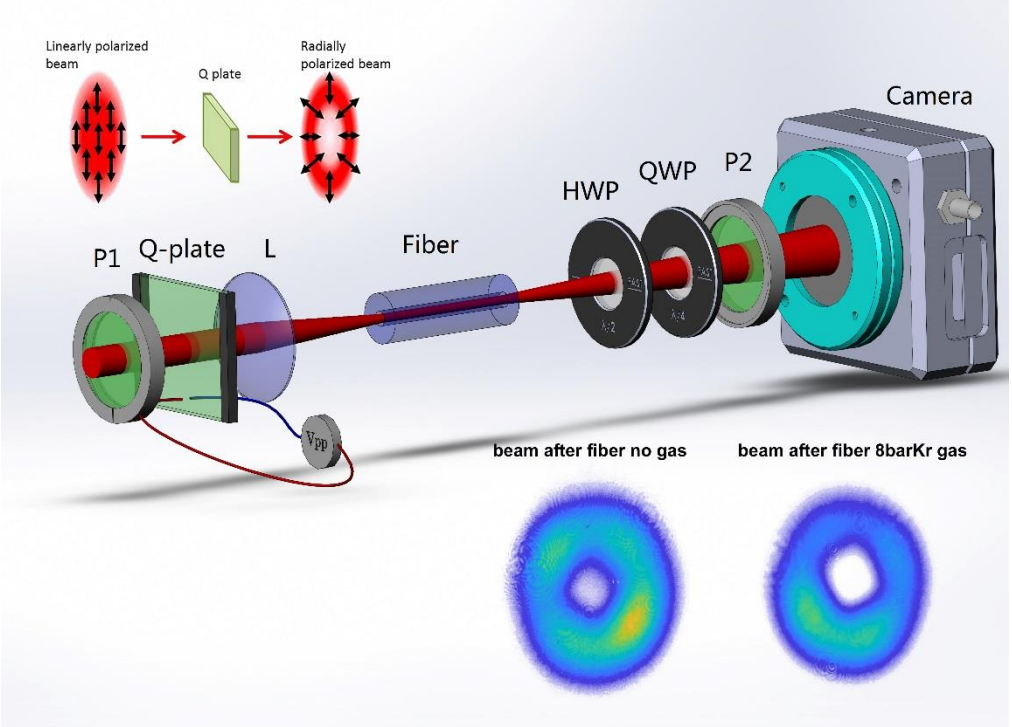

Fig. 6-1. Setup of a few-cycle vortex beam generation experiment with a 1.8 μm laser source. P1, P2: polarizers; Vpp: power supply for the *q*-plate; L: lens. Fiber: 20cm long, 150 μm core; HWP: achromatic half-wave plate for the central wavelength of 1.8 μm; QWP: achromatic quarter-wave plate for the central wavelength of 1.8 μm; The right lower two figures show the beam profile of the output beams after the fiber put under vacuum and filled with 8 bar Kr gas, respectively.

However, similar to other mode convertors, the *q*-plate can only support a relatively narrow spectrum for a given voltage. In Fig. 6-2, we compare the polarization of the initial pulse (blue) and the pulse that has passed the *q*-plate (red). We perform this comparison over a broadband infrared spectrum ranging from 1.5 μm to 2.1 μm and recorded the pulse's spectrum after going through a polarizer with a fiber spectrometer (Ocean Optics, USB 2000+). A *q*-plate fundamentally consists of a structured half-wave plate such that a passing beam's polarization locally remains linear but is rotated to a degree depending on the relative angle between the beam's polarization and the local alignment of the liquid crystals. We can make use of this effect to extract the bandwidth that the *q*-plate supports by examining the degree to which linear polarization is preserved throughout our spectrum. This degree of similarity can be measured by making the beam go through a polarizer. Namely, we expect wavelengths that experience the required conversion to remain linear with 90° rotation and therefore not to go through the polarizer. To gauge this condition, we use a measure called the "polarization identicality" defined as the minimum output of the polarizer as the polarizer is rotated divided by the maximum output. In Fig. 6-1, the blue and red curves show the polarization identicality of the beams before and after the *q*-plate respectively. Only a ~100 nm bandwidth gets a similar optical retardation and maintains a zero-valued polarization

identicality. Therefore, Fig. 6-2 shows that a *q*-plate cannot support the full spectrum of a few-cycle [196].

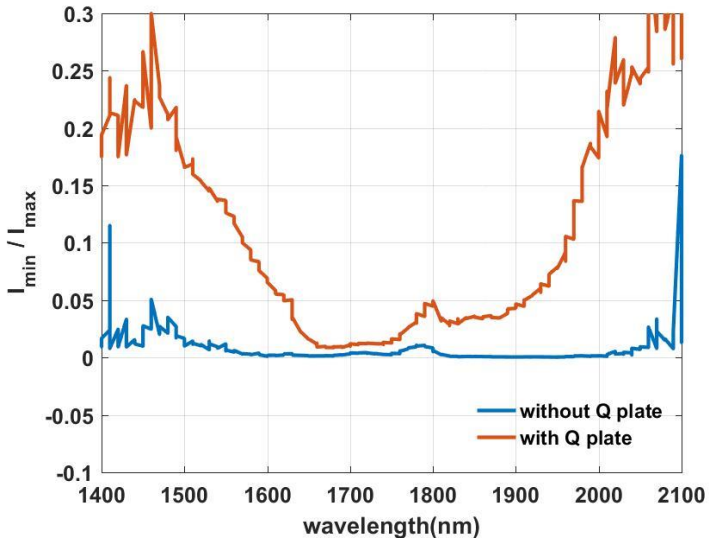

Fig. 6-2. "Polarization identicality" of the laser beam before and after the *q*-plate. This measure is defined in the text and is an indicator of the conversion efficiency of the *q*-plate at a given wavelength where values closer to zero indicate a higher efficiency. The blue and red curves show the identicality of the beam before and after the *q*-plate, respectively.

6.2 Pulse compression after converting the mode

Since most of spatial mode conversion has the bandwidth limit, just like the *q*-plate, we have to use the *q*-plate where the pulse bandwidth is relatively narrow – i.e. before pulse compression. As shown in Fig. 6-1, a polarizer after the fiber spatial filter is used to maintain a homogeneous linear polarization. Then the beam passes a *q*-plate with a proper bias voltage for the central wavelength of 1.8 μm and the linear input polarization is transformed into radial polarization.

The radially polarized beam was then re-focused into a krypton-filled hollow-core fiber (20 cm long, 150 μm or 250 μm core diameter) by an f = 15 cm or 30 cm lens as shown in Fig. 6-2. The nonlinear propagation in the hollow-core fiber adds bandwidth and an approximately linear positive chirp. In Fig. 6-2, the right lower two figures show the beam profile of the output beams after the fiber under vacuum and filled with 8bar krypton gas, respectively. We can see that the beam has a uniform doughnut-shaped intensity profile and is not distorted by passing the hollow-core fiber when it is used passively or when it was filled with krypton gas.

For our experiment, the Gaussian beam on the *q*-plate has a pulse energy of 200μJ within a ~5.5mm FWHM beam diameter. Using a radially polarized beam with input energy of 150 μJ, we achieved 40% transmission. In comparison, the transmission for the Gaussian beam is 47% (using the same coupling geometry). The highest energy we had used on the *q*-plate is 220 μJ. Therefore, the damage threshold of the *q*-plate is higher than 1.85×10^{10} W cm^{-2}.

In the krypton-filled hollow-core fiber, the spectrum of the pulse is broadened by self-phase modulation. Since the polarization is inhomogeneous in the transverse plane, therefore, the pulse characterization is performed by sampling different segments of the beam. Figure 6-3(a) shows the broadened spectrum for four segments of the beam selected from the vector beam. Self-phase modulation within the hollow core fiber broaden the spectrum of all the four segments. The spectra of the lower, left and right parts of the beam have a similar bandwidth while that of the upper part is a little broader.

Similar to conventional fiber compression that a pulse that exits a fiber is chirped, we compensate the chirp with an antireflection coated fused silica plate in the beam path [197]. To characterize the spectral phase and the beam's temporal duration, we performed second-harmonic-generation (SHG) frequency-resolved optical gating (FROG) on these four segments. The temporal profiles of the amplitude and phase of different quadrants of the compressed pulses are shown in Fig. 6-3(b-e). These curves correspond to 15 fs pulses for the upper part of the beam and 17 fs pulses for the remaining three segments. All sampled pulse durations are less than three optical cycles in duration and have a central wavelength of 1.8 μm.

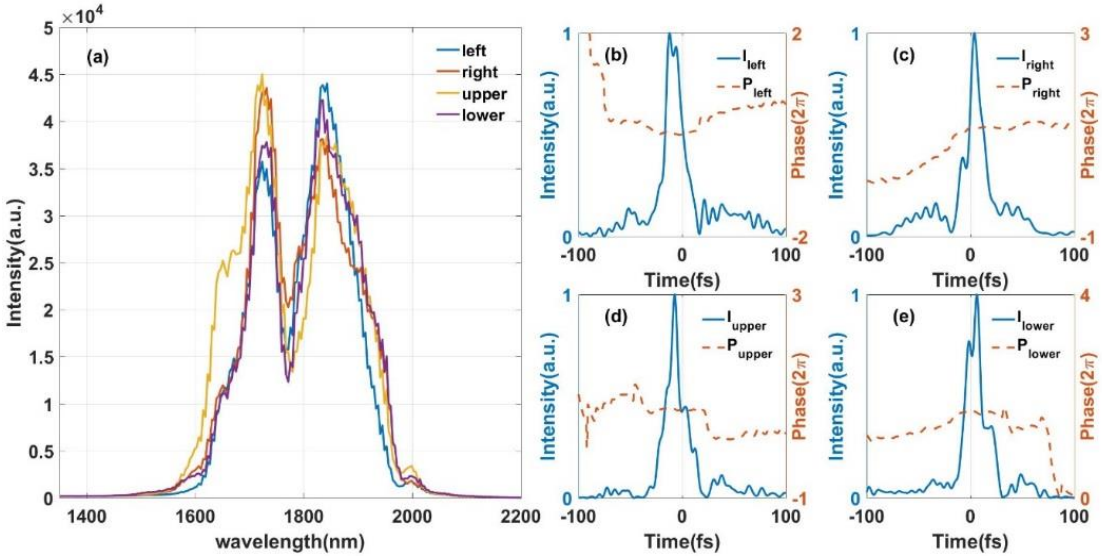

Fig. 6-3. Compression of the radially polarized beam. (a) Spectra of the spatially polarized beam measured at four different spatial locations after the fiber compressor. The spectra of the lower, left and right parts are similar and the upper spectrum is a little broader than the others. (b-e) The temporal profiles (blue curves) and phases (red curves) of the laser fields corresponding to the four spectra in (a) measured using a FROG. The pulse duration of the lower, left and right parts is 17 fs and that of the upper part is 15 fs which agrees with their bandwidths.

In addition to measuring the pulse duration, we also confirm its polarization state is preserved during the compression. We measured the polarization state of the output broadened beam by passing the beam through a polarizer and recorded the beam profile using a CMOS camera (Data Ray WinCamD-LCM). For a radially polarized beam, after the polarizer, the output beam will be a linearly polarized beam with polarization parallel to the transmission axis of

the polarizer. The output electric field strength will have its peak at the polarizer's orientation angle. As shown in Fig. 6-4, the intensity profile has two lobes that rotate with the orientation of the polarizer which is indicated by red arrows (Fig. 6-4 (b) to (e)). Therefore, the beam polarization is always oriented with the radial direction along the polarizer axis. It confirms that the output broadened beam is still a cylindrical vector beam with radial polarization.

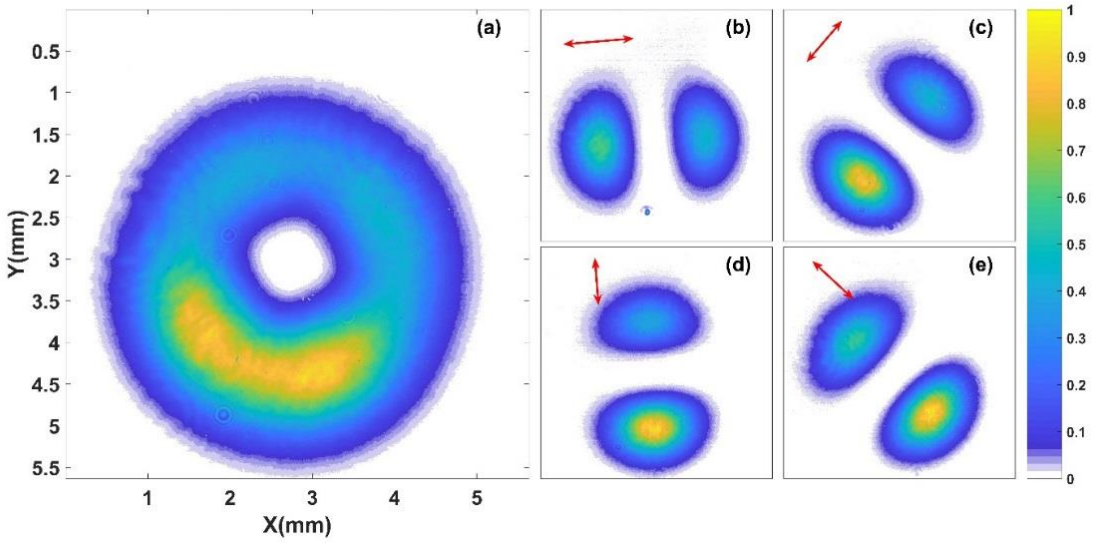

Fig. 6-4. Polarization measurement of the radially polarized beam. (a) beam profile without polarization selection. (b-e) beam profiles upon propagating through a polarizer measured with a CCD camera for four different axis angles.

6.3 Characterizing the polarization topology

We also characterized the topological charge of the compressed polarization vector beam. For beams with phase singularities, the topological charge of the latter is quantified by recording the interference between the beam and a tilted Gaussian, thus resulting in a forked interference pattern [118]. The difference in the number of interference fringes between one side and the other corresponds to the topological charge of the singularity. An equivalent approach can be used to portrait the polarization singularity carried by vector beam, which uses two colinear components in the vector beam with opposite handedness.

A radially polarized beam is a beam that can be considered to be a superposition of left and right circularly polarized components with a phase delay around the circumference. The required phase delay corresponding to the two beams having opposite helicity and both possess one unit of topology charge. The Jones matrix expression of a radially polarized beam with an azimuthal phase $\exp(i\varphi)$ can be written as

$$\begin{pmatrix}\cos\varphi\\ \sin\varphi\end{pmatrix}=\frac{1}{2}\exp(-i\varphi)\cdot\begin{pmatrix}1\\ i\end{pmatrix}+\frac{1}{2}\exp(i\varphi)\cdot\begin{pmatrix}1\\ -i\end{pmatrix} \tag{6.1}$$

which consists of a right-hand circularly polarized (RHCP) beam and a left-hand circularly polarized (LHCP) beam with opposite helicity and opposite topological charge where φ is the azimuthal coordinate angle in the plane perpendicular to the propagation.

If this beam passes through a quarter-wave plate, the two circularly polarized components identified above will be converted into two perpendicular linearly polarized beams. Then a polarizer will interfere the two components when we select a given polarization direction.

Finally, if we insert a half-wave plate between the *q*-plate and the quarter wave plate, the half-wave plate flips the handedness of the circularly polarized beams and also shifts the relative phase between the two circularly polarized components. Assuming the angle that the fast axis of the half-wave plate makes with respect to the x–axis is θ, the Jones matrix of the half-wave plate can be derived as in Eq. (1.3). The Jones representation for the whole setup shown in Fig. 6-2 is:

$$\frac{1}{2}\begin{pmatrix}1 & 0\\ 0 & 0\end{pmatrix}\begin{pmatrix}1 & 0\\ 0 & i\end{pmatrix}\begin{pmatrix}\cos 2\theta & \sin 2\theta\\ \sin 2\theta & -\cos 2\theta\end{pmatrix}\left[\exp(-i\varphi)\begin{pmatrix}1\\ i\end{pmatrix}+\exp(i\varphi)\begin{pmatrix}1\\ -i\end{pmatrix}\right]=\cos(\varphi-2\theta)\cdot\begin{pmatrix}1\\ 0\end{pmatrix} \quad (6.2)$$

Thus, the half-wave plate gives a positive 2θ phase delay to the left circular polarized beam and a negative 2θ phase delay to the right circular polarized beam. Therefore, we should observe a $\pm 2\theta$ phase delay for the two linearly polarized beams and the two arms of the linear interferometer.

As we rotate the half-wave plate, the relative phase between the two arms of the interferometer will be changed accordingly. The relative phase change is four times the phase delay corresponding to the rotated angle of the half-wave plate. During a full scan of the wave plate, the phase delay between the interferometer arms would be 4 times the phase gradient of the beam's wave front. Therefore, the period number of the interference signal for a full circle scan of the half-wave plate also gives the topological charge.

To retrieve the topology of the polarization rotation, we recorded the beam profile with the CMOS camera as a function of the rotation angle of the half-wave plate, as shown in Fig. 6-2. We obtain a two-lobe intensity pattern, similar to the pattern obtained by passing through a polarizer (Fig. 6-2). When the half-wave plate is rotated, the two-lobe pattern rotates accordingly. Figure 6-4 (a) shows the sum of all the beam intensity patterns for a full 360° scan. Alternatively, we can select one $\delta\varphi$ wide segment of the beam and record the signal as the half wave plate is rotated. We plot the beam energy in this segment as a function of the half-wave plate rotation angle θ in Fig. 6-4(b). We obtained four peaks in a full 360° scan indicating that the phase changes by 2π for a full 360° wave plate scan.

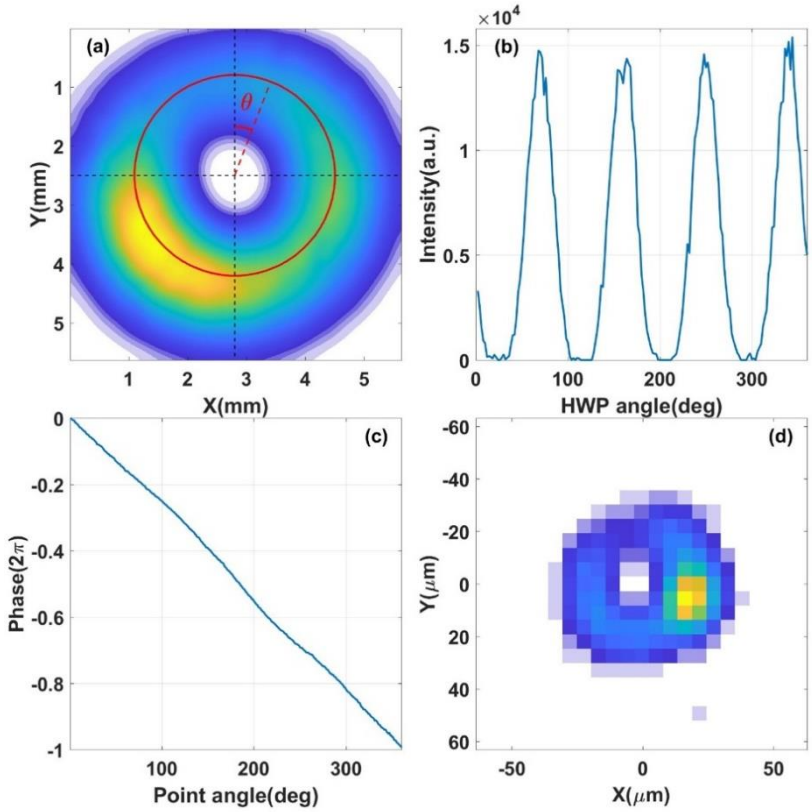

Fig. 6-5. Wave front interference scan and the focus beam profile. (a) Integrated intensity profiles for a full 360° scan. (b) Interference signal for one point of the beam as a function of HWP angle. (c) The phase retrieved for different points on the circle's circumference. (d) The focus beam profile of the compressed radially polarized beam.

The phase φ can be retrieved by fitting the maximum points of the curve in Fig. 6-5(b), since the condition for the maximum intensity is only obtained when $\varphi = 2\theta$. We retrieved the phase of each point on the circle with 2° resolution and plotted it as the function of the point angle in Fig. 6-5(c). The curve confirms the 2π phase shift of the beam wave front for the full 360° scan of the half-wave plate, corresponding to the topological charge equal to one. The phase is almost linear with respect to the point angle.

6.4 Nonlinear optics with few-cycle vector beam

These pulses will have broad applications in high-field physics, and we confirm the focus beam profile of these pulses to estimate the performance of the compressed beam. We focus the compressed pulses with an f = 75mm CaF_2 lens and the profile is shown in Fig. 6-5 (d). The beam diameter is ~60 μm. With 15 fs pulse duration and 60 μJ energy, we can estimate the peak intensity $>1.4\times10^{14}$ W cm^{-2}. This peak intensity is enough for many strong-field experiments on solid target.

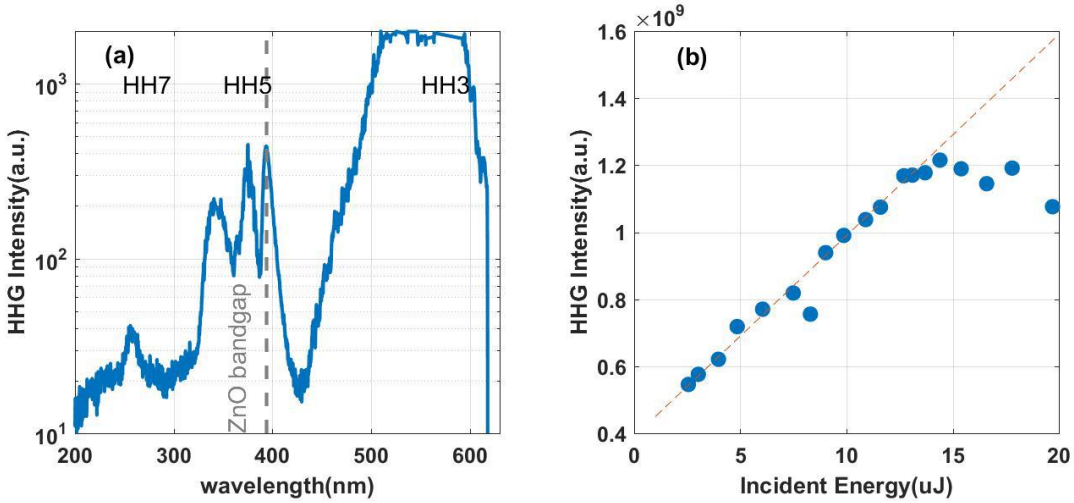

Fig. 6-6 High-order harmonic generation from ZnO. (a) Harmonic spectrum (harmonic orders are indicated as HH3 to HH7) from the ZnO sample. (b) Intensity scaling of the 5th harmonic yields from the ZnO sample with respect to different pulse energy of the driving pulse.

Figure 6-6 shows an experiment using the compressed vector beam to generate optical harmonics from ZnO crystal. Both harmonics below and above the ZnO bandgap are observed in Fig. 6-6(a). Fig. 6-6(b) depicts the harmonic yields verses the incident pulse energy. We can see that the signal start to decreases when the intensity is high, which indicate the pulse is intense enough to go beyond the damage threshold of ZnO crystal. This experiment is an example of observing nonlinear optical phenomenon with ultra-short vector beam.

In our experiment the beam energy is limited by the laser and the size of the *q*-plate we used which is ~5mm. Had we used a larger *q*-plates and a high energy OPA, the energy and peak intensity could have been higher. In fact, S-waveplates [198], a relative of *q*-plates but made by cracking quartz, will with stand much higher intensity. The current limiting factor is hollow core pulse compression with an experimental limit of ~ 15 mJ.

A 5 mJ pulse [199] with pulse duration of 15 fs has a peak power of 3×10^{11} W. Focused to the wavelength scale an intensity of 10^{19} W cm^{-2} is feasible. This would be a very interesting pulse with a longitudinal field reaching relativistic intensities (~10^{18} W cm^{-2} for 800 nm wavelength). Long before such an intensity, high harmonics can be created in gases and solids, opening a new regime of attosecond science.

In conclusion, we have used a gas filled hollow-core fiber to compress a radially polarized vector beam in the same way that we compress Gaussian beams. While we employed 1.8 μm light for this demonstration, we expect that hollow-core fiber compression will be possible for other wavelengths and that it can be generalized to more complex fibers. Pulse compression should be possible for any cylindrically symmetric vector beam and we expect that vector beam pulse compression can be generalized to single [200] or multi-plate pulse compression [201] as well.

These pulses will be important for laser acceleration experiments [202] as well as for high harmonic or attosecond pulse experiments with radially polarized drivers. Using solid or gas as a nonlinear medium, it will be possible to produce radially polarized harmonics with a curved wave front [177] that will reach wavelength scale focal spots compared to Gaussian beams [98], thus opening a route towards vacuum or extreme ultraviolet microscopy.

Chapter 7 Conclusion and perspectives

7.1 Conclusion

In this thesis, I have proposed the implementation of spatially structured beams in strong field experiments, particularly in the case of generating high-order harmonics. Shaping the spatial profile of the fundamental beam provides a new degree of freedom to control the characteristics of high harmonic XUV beams.

Both the phase front and polarization of the high harmonic beams can be tailored entirely by optical means, without the use of special XUV optics. XUV high harmonic beams generated in such a way can obtain spiral shaped phase fronts with arbitrary topological charges and circularly polarized electric fields. These characteristics cannot be produced using conventional high-harmonic based sources. Table 7-1 summarizes the results of this work, which explores the properties of both the spatial phase and polarization of XUV high-harmonic beams, along with other important advances in the development of high harmonic sources. Spatially structured source is a relatively new area of research within the high-harmonic generation research community and its continued development is a highly sought-after goal in the field.

	Amplitude	Frequency	Phase	Polarization
Time	Amplitude gating single attosecond pulse [57] [203] [204]	Waveform synthesis [205] [206]	Few cycle carrier-envelope phase effects [207]	Polarization gating single attosecond pulse [42] [43] [44]
Space	Annular beam high harmonic generation [208]	Attosecond lighthouse [209]	Vortex XUV beams **Chapter 3, 5**	Vector /circularly polarized XUV beam **Chapter 4, 5, 6**

Table 7-1 **Comparison between high-harmonic techniques using beams shaping.** The work explored the underdeveloped research in studying the spatial property of both phase and polarization of strong field experiments. Like other techniques listed in the table, the novel high-harmonic structured beams expand the capabilities of table-top XUV sources.

Regarding the angular momentum of high harmonic beams, this thesis revealed how spin and orbital angular momentum can be transferred to XUV beams in a controlled manner. The generation of XUV beams in this way was shown to conserve angular momentum, despite the highly nonlinear and non-perturbative underlying physics of the XUV generation process.

These results can be understood using the recollisional model of high harmonic generation and can be accurately described with the semiclassical three-step model.

With the semiclassical three-step model, this work explained how the phase structure of the fundamental beam can be transferred to the emitted phase structure of the high harmonic beams. The emitted phase is predominantly accumulated during propagation of the electron in the continuum. By varying the trajectory of the electron during propagation, the phase of the fundamental beam is imprinted onto the resultant phase of the high harmonics.

Based on the relation revealed with the three-step model, we then introduced a holographic approach to shape the wave fronts of high harmonic beams. We used a perturbing beam with a spiral wave front to control the high harmonic generation process and generate XUV beams with controlled orbital angular momenta. The phase front of the first-order diffracted XUV beam replicates the spiral wave front of the fundamental beam. From a wave-mixing point of view, this result also confirms that the orbital angular momentum is conserved in this non-perturbative nonlinear process. In addition to generating XUV vortex beams, this method is generally capable to produce other wave front structures at XUV wavelength. This approach makes the liquid crystal beam shaping techniques immediately available to high harmonic generation experiments and links the research fields of structured light and strong field.

Further, the polarization of the fundamental beam was also shaped to generate circularly polarized harmonics. We used a liquid crystal phase plate to shape the local polarization of the fundamental beam. The polarization of the fundamental beam evolves throughout its propagation. The polarizations are purely circular in the far field and primarily linear in the near field, where the high harmonics are generated. Shaping of the polarization opens up the possibility to use the inhomogeneous polarization mode of the fundamental to expand the capability of high-harmonic-based light sources in the generation of radiation with complex polarizations.

The polarization and the phase front of a beam are associated with the spin and orbital angular momentum, respectively. These two parts of the orbital angular momentum are intrinsically related. To combine the phase and polarization, we also discussed the interplay between the spin and orbital angular momentum in the process of high harmonic generation. We have shown that the spin and orbital angular momentum are respectively conserved within the paraxial region and when the nonlinear system is rotationally symmetric. Therefore, the transfer of orbital angular momentum can be limited by the selection rule of spin angular momentum.

Implementing structured beams enables the production of XUV photons with controllable orbital and spin angular momenta. The interplay between these two components of the total angular momentum imposes additional constraints during the high harmonic generation process. This thesis discussed the conservation of spin-orbital angular momentum under the paraxial condition while interacting with trivial topological systems, which are most commonly applied in high harmonic generation experiments (e.g. diffuse gas jets). Different

types of spin-orbital coupling or selection rules may occur while these conditions do not apply. Therefore, this thesis demonstrates a clear direction for continued research in this area and the extension of high-harmonic and attosecond science to several new fields wherein experiments can be developed, for example, using tight focusing geometries or interactions with non-trivial topological systems.

To further develop spatially structured light sources for high intensity experiments, where the carrier envelop phase plays an important role, we developed a few-cycle vector beam source by compressing broadband vector beams in a hollow core fiber system. This scheme overcomes the bandwidth limitation of the mode converter during the beam shaping and produces pulses with 25 fs duration while preserving the radial polarization. These spatially structured ultrashort pulses combine complex spatial characteristics and high temporal resolution. The large bandwidth and the sub-cycle dynamic of the few-cycle pulse enables coherent control while interacting with matter. The interaction of such precisely structured pulses of light, in both space and in time, provide a new tool to study nonlinear interactions of such pulses with matter.

7.2 Perspectives

Besides generating high energy photons, controlling the electron ionization and motion is an important subject frequently discussed in strong-field physics. Previous studies have shown that strong laser fields can control the behavior of such electrons by tuning their phase and polarization. On the other hand, structured beams exbibit inhomogeneous polarization and phase front characteristics. Combining these two aspects leads to spatial control of ionized electrons, just like what we have done to the XUV photons. Here we propose a possible route to use structured laser fields to generate transient current loops and magnetic impulses in the THz frequency range, which could benefit next generation magnetic metrology.

Electric charge in motion generates magnetic fields, and confining currents to conductors or superconductors in a solenoidal configuration forms the basis of state-of-the-art magnetic field sources. The magnetic field generated at the center of an ideal solenoid is expressed by the following relation: $B = \mu nI$, where μ is the permeability of the core material, $n = N/L$ is the number of wire turns per unit length, and I is the circulating current. Generating large magnetic fields is, therefore, inseparable from confining high current to a compact volume. In the case of electrical conductors, the current is limited by the resistivity of the conductor together with its temperature regulation. The performance of a superconductor is restricted by its critical current density, beyond which a flux-flow resistivity is present.

Ionization and charge acceleration induced by optical fields presents an alternative route to control high current densities. A gas medium with a high ionization potential, I_p, permits the application of strong optical fields before a gas is ionized. Atomic helium (I_p = 24.6 eV) can withstand electric fields exceeding E = 6.75 V/Å (intensity, $I = 6.1 \times 10^{14}$ W cm^{-2}). When ionized by λ = 4000 nm light, the ponderomotive energy is $U_p = e^2E^2/4m\omega_0^2$ = 903eV, where

m is the electron mass, e is the electron charge, and ω_0 is the angular frequency of the optical field), corresponding to an electron velocity, $v = (2eU_p/m)^{1/2} = 1.78 \times 10^7$m/s. The combination of an ionized gas population of $n_i = 10^{18}$ cm^{-3} and an electron velocity of $v = 10^7$ m/s enables a current density beyond $|J| = |q|n_i v = 1.6 \times 10^{12}$ A/m^2 to be driven by the optical fields. This current density surpasses what is possible in conductors or superconductors by approximately three orders of magnitude. Harnessing photo-excited currents offers the possibility for ultrafast, optically synchronized magnetic fields of record-breaking magnetic field amplitudes.

Delicate control of charge motion in solids and gases can be achieved through "coherent control", an optical technique whereby a laser pulse with angular frequency, ω, is applied to a system simultaneously and co-linearly with its second harmonic, 2ω [210,211]. The system can be driven into degenerate excited states by each of the two pulses independently. Applying the two pulses coherently and adjusting their relative phase enables control of quantum interference between the two excitations. In atomic systems, the two laser pulses can be used to ionize an atom, and their relative phase exerts control on the direction and energy of the photo-ionized population.

By relaxing the requirement for a solenoid composed of wires, one can envisage a solenoid consisting of a continuous sheet of circulating charge. In this case, an equivalent expression for the ideal solenoid equation can be written as: $B = \mu I_L$, where I_L is the circulating current per unit length.

This scenario can be realized using coherent control driven by two cylindrical vector beams with azimuthal polarization. The electric fields of the azimuthal beam have linear polarization pointing in the azimuthal direction at each point in the beam. When ω and 2ω azimuthal beams are used to control photoionization in a gas, the spatial intensity and polarization configuration of the azimuthal beams are transferred to the collective electron motion of the ionized gas. The collective electron trajectories circulate around the longitudinal axis of the laser beam, and the charge motion produces an azimuthal current density, J_θ. This current density induces a longitudinal magnetic field, B_z. The direction and amplitude of both the current and the induced magnetic field can be precisely controlled by adjustment of the relative phase between the two light waves.

For an azimuthal laser beam focused into helium gas to a $\omega_0 = 200$ μm beam waist, one can estimate confinement of the gas ionization to a radial extent of approximately $\Delta r = 40$ μm. The current per unit length can be calculated as, $I_L = J\Delta r = 6.4 \times 10^7$ A/m, which would produce magnetic fields on the order of $B = \mu_0 I_L = 80$ T, similar to those available in state-of-the-art magnetic field facilities. However, turning on such high magnetic fields using femtosecond laser pulses would result in a large back electromotive force (herein back-EMF) acting on the ionized electrons. Faraday's Law, $\oint E_{EMF} \cdot \mathrm{d}l = -\int \frac{\partial B}{\partial t} \cdot \mathrm{d}A$, can be used to estimate the amplitude of the back-EMF field present at the beam radius, ω_0: $2\pi\omega_0 E_{EMF} = -\pi\omega_0^2 \Delta B/\Delta t$. Turning on $\Delta B = 80$ T within $\Delta t = 50$ fs produces a back-EMF, $E_{EMF} = -16$ V/Å, which is even larger than the driving field. These estimates suggest that, while the final

magnetic field may not reach 80 T, large, rapid rise-time, isolated, *B*-fields are feasible. To proceed, we need a model that can capture the complex spatio-temporal coupling of charge motion, induced magnetic and back-EMF fields. To account for these intricacies, a detailed simulation is conducted in [212], which suggested up a few Tesla magnetic field. Since atmospheric density plasmas lose coherence on a picosecond timescale, the current loop radiates electro- magnetic impulses at terahertz bandwidth.

Such fields would be a powerful new tool for condensed matter physics, atomic and molecular physics, and could potentially be used for guiding charged particle beams for plasma physics. In contrast to conventional magnetic fields, which have been limited in bandwidth to gigahertz frequencies, this scheme provides a route to magneto-optical pump-probe measurements at terahertz frequencies. The introduction of short, intense magnetic impulses in the form of electromagnetic waves would also enable optical synchronization with sophisticated detection schemes, such as magneto-optical sampling, high-harmonic magnetic circular dichroism spectroscopy, or spin-polarized attosecond electron diffraction, enabling temporal resolution of magnetic-field-induced microscopic dynamics. Magnetic field metrology based on this ultrafast optical generation scheme will enable new frontiers in magnetism, particularly scaling to higher magnetic fields and resolution of femtosecond and attosecond magnetization dynamics.

Bibliography

[1] A. Einstein, Ann. Phys. **17**, 132 (1905).

[2] H. D. Young, R. A. Freedman, A. L. (Albert L. Ford, and F. W. Sears, *University Physics with Modern Physics , Thirteenth Edition* (Addison-Wesley, 2012).

[3] A. M. Bonch-Bruevich and V. A. Khodovoĭ, Sov. Phys. Uspekhi **8**, 1 (1965).

[4] N. B. Delone and V. P. Krainov, *Multiphoton Processes in Atoms* (Springer Berlin Heidelberg, Berlin, Heidelberg, 2000).

[5] W. Chao, B. D. Harteneck, J. A. Liddle, E. H. Anderson, and D. T. Attwood, Nature **435**, 1210 (2005).

[6] J. Itatani, J. Levesque, D. Zeidler, H. Niikura, H. Pépin, J. C. Kieffer, P. B. Corkum, and D. M. Villeneuve, Nature **432**, 867 (2004).

[7] M. Dantus, M. J. Rosker, and A. H. Zewail, J. Chem. Phys **87**, 2395 (1987).

[8] A. H. Zewail, J. Phys. Chem. A **104**, 5660 (2000).

[9] L. E. Myers, R. C. Eckardt, M. M. Fejer, R. L. Byer, W. R. Bosenberg, and J. W. Pierce, J. Opt. Soc. Am. B **12**, 2102 (1995).

[10] A. Wirth, M. Th Hassan, I. Grguraš, J. Gagnon, A. Moulet, T. T. Luu, S. Pabst, R. Santra, Z. A. Alahmed, A. M. Azzeer, V. S. Yakovlev, V. Pervak, F. Krausz, and E. Goulielmakis, *Synthesized Light Transients* (n.d.).

[11] M. Ossiander, J. Riemensberger, S. Neppl, M. Mittermair, M. Schäffer, A. Duensing, M. S. Wagner, R. Heider, M. Wurzer, M. Gerl, M. Schnitzenbaumer, J. V. Barth, F. Libisch, C. Lemell, J. Burgdörfer, P. Feulner, and R. Kienberger, Nature **561**, 374 (2018).

[12] A. Kessel, V. E. Leshchenko, O. Jahn, M. Krüger, A. Münzer, A. Schwarz, V. Pervak, M. Trubetskov, S. A. Trushin, F. Krausz, Z. Major, and S. Karsch, Optica **5**, 434 (2018).

[13] X. Xie, J. Dai, and X.-C. Zhang, Phys. Rev. Lett. **96**, 075005 (2006).

[14] G. J. Schneider, J. A. Murakowski, C. A. Schuetz, S. Shi, and D. W. Prather, Nat. Photonics **7**, 118 (2013).

[15] P. A. Franken, A. E. Hill, C. W. Peters, and G. Weinreich, Phys. Rev. Lett. **7**, 118 (1961).

[16] M. M. Fejer, G. A. Magel, D. H. Jundt, and R. L. Byer, IEEE J. Quantum Electron. **28**, 2631 (1992).

[17] P. B. Corkum, C. Rolland, and T. Srinivasan-Rao, Phys. Rev. Lett. **57**, 2268 (1986).

[18] R. R. Alfano and S. L. Shapiro, Phys. Rev. Lett. **24**, 592 (1970).

[19] J. M. Dudley, G. Genty, and S. Coen, Rev. Mod. Phys. **78**, 1135 (2006).

[20] J. K. Ranka, R. S. Windeler, and A. J. Stentz, Opt. Lett. **25**, 25 (2000).

[21] M. Cassataro, D. Novoa, M. C. Günendi, N. N. Edavalath, M. H. Frosz, J. C. Travers, and P. S. J. Russell, Opt. Express **25**, 7637 (2017).

[22] F. Belli, A. Abdolvand, W. Chang, J. C. Travers, and P. S. J. Russell, Optica **2**, 292 (2015).

[23] A. D. Shiner, B. E. Schmidt, C. Trallero-Herrero, H. J. Wörner, S. Patchkovskii, P. B. Corkum, J.-C. Kieffer, F. Légaré, and D. M. Villeneuve, Nat. Phys. **7**, 464 (2011).

[24] H. J. Wörner, J. B. Bertrand, D. V. Kartashov, P. B. Corkum, and D. M. Villeneuve, Nature **466**, 604 (2010).

[25] A. L. Cavalieri, N. Müller, T. Uphues, V. S. Yakovlev, A. Baltuška, B. Horvath, B. Schmidt, L. Blümel, R. Holzwarth, S. Hendel, M. Drescher, U. Kleineberg, P. M. Echenique, R. Kienberger, F. Krausz, and U. Heinzmann, Nature **449**, 1029 (2007).

[26] C. Wagner and N. Harned, Nat. Photonics 2010 41 (2010).

[27] J. P. Delaboudinière, G. E. Artzner, J. Brunaud, A. H. Gabriel, J. F. Hochedez, F. Millier, X. Y. Song, B. Au, K. P. Dere, R. A. Howard, R. Kreplin, D. J. Michels, J. D. Moses, J. M. Defise, C. Jamar, P. Rochus, J. P. Chauvineau, J. P. Marioge, R. C. Catura, J. R. Lemen, L. Shing, R. A. Stern, J. B. Gurman, W. M. Neupert, A. Maucherat, F. Clette, P. Cugnon, and E. L. Van Dessel, in *Sol. Phys.* (Springer Netherlands, Dordrecht, 1995), pp. 291–312.

[28] J. J. Macklin, J. D. Kmetec, and C. L. Gordon, Phys. Rev. Lett. **70**, 766 (1993).

[29] A. L'Huillier and P. Balcou, Phys. Rev. Lett. **70**, 774 (1993).

[30] P. B. Corkum, Phys. Rev. Lett. **71**, 1994 (1993).

[31] J. L. Krause, K. J. Schafer, and K. C. Kulander, Phys. Rev. Lett. **68**, 3535 (1992).

[32] M. Lewenstein, P. Balcou, M. Y. Ivanov, A. L'Huillier, and P. B. Corkum, Phys. Rev. A **49**, 2117 (1994).

[33] H. Eichmann, A. Egbert, S. Nolte, C. Momma, B. Wellegehausen, W. Becker, S. Long, and J. K. McIver, Phys. Rev. A **51**, R3414 (1995).

[34] M. Hentschel, R. Kienberger, C. Spielmann, G. A. Reider, N. Milosevic, T. Brabec, P. Corkum, U. Heinzmann, M. Drescher, and F. Krausz, Nature **414**, 509 (2001).

[35] H. Niikura, F. Légaré, R. Hasbani, A. D. Bandrauk, M. Y. Ivanov, D. M. Villeneuve, and P. B. Corkum, Nature **417**, 917 (2002).

[36] H. Niikura, F. Légaré, R. Hasbani, M. Y. Ivanov, D. M. Villeneuve, and P. B. Corkum, Nature **421**, 826 (2003).

[37] E. Priori, G. Cerullo, M. Nisoli, S. Stagira, S. De Silvestri, P. Villoresi, L. Poletto, P. Ceccherini, C. Altucci, R. Bruzzese, and C. de Lisio, Phys. Rev. A **61**, 063801 (2000).

[38] Z. Chang, A. Rundquist, H. Wang, M. M. Murnane, and H. C. Kapteyn, Phys. Rev. Lett. **79**, 2967 (1997).

[39] C. Spielmann, A. Durfee, N. Chang, R. Herne, D. Backus, S. Murnane, I. P. Kapteyn, A. Aquila, E. M. Gullikson, D. T. Attwood, M. M. Murnane, and H. C. Kapteyn, Science (80-.). **278**, 661 (1997).

[40] T. Popmintchev, M.-C. Chen, D. Popmintchev, P. Arpin, S. Brown, S. Alisauskas, G. Andriukaitis, T. Balciunas, O. D. Mücke, A. Pugzlys, A. Baltuska, B. Shim, S. E. Schrauth, A. Gaeta, C. Hernández-García, L. Plaja, A. Becker, A. Jaron-Becker, M. M. Murnane, and H. C. Kapteyn, Science **336**, 1287 (2012).

[41] M. Drescher, M. Hentschel, R. Kienberger, M. Uiberacker, V. Yakovlev, A. Scrinzi, T. Westerwalbesloh, U. Kleineberg, U. Heinzmann, and F. Krausz, Nature **419**, 803 (2002).

[42] O. Tcherbakoff, E. Mével, D. Descamps, J. Plumridge, and E. Constant, Phys. Rev. A **68**, 043804 (2003).

[43] B. Shan, S. Ghimire, and Z. Chang, J. Mod. Opt. **52**, 277 (2005).

[44] I. J. Sola, E. Mével, L. Elouga, E. Constant, V. Strelkov, L. Poletto, P. Villoresi, E. Benedetti, J.-P. Caumes, S. Stagira, C. Vozzi, G. Sansone, and M. Nisoli, Nat. Phys. **2**, 319 (2006).

[45] R. W. Boyd, *Nonlinear Optics* (Academic Press, 2008).

[46] D. Umstadter, J. Phys. D. Appl. Phys. **36**, R151 (2003).

[47] L. V Keldysh, J. Exptl. Theor. Phys. **20**, 1945 (1965).

[48] K. J. Schafer, B. Yang, L. F. DiMauro, and K. C. Kulander, Phys. Rev. Lett. **70**, 1599 (1993).

[49] B. Walker, B. Sheehy, L. F. DiMauro, P. Agostini, K. J. Schafer, and K. C. Kulander, Phys. Rev. Lett. **73**, 1227 (1994).

[50] A. McPherson, G. Gibson, H. Jara, U. Johann, T. S. Luk, I. A. McIntyre, K. Boyer, and C. K. Rhodes, J. Opt. Soc. Am. B **4**, 595 (1987).

[51] D. N. Fittinghoff, P. R. Bolton, B. Chang, and K. C. Kulander, Phys. Rev. Lett. **69**, 2642 (1992).

[52] M. Ferray, A. L'Huillier, X. F. Li, L. A. Lompre, G. Mainfray, and C. Manus, J. Phys. B At. Mol. Opt. Phys. **21**, L31 (1988).

[53] P. Dietrich, N. H. Burnett, M. Ivanov, and P. B. Corkum, Phys. Rev. A **50**, R3585 (1994).

[54] C. Danson, D. Hillier, N. Hopps, and D. Neely, High Power Laser Sci. Eng. **3**, e3 (2015).

[55] M. D. Perry and G. Mourou, Science **264**, 917 (1994).

[56] D. Strickland and G. Mourou, Opt. Commun. **56**, 219 (1985).

[57] E. Goulielmakis, M. Schultze, M. Hofstetter, V. S. Yakovlev, J. Gagnon, M. Uiberacker, A. L. Aquila, E. M. Gullikson, D. T. Attwood, R. Kienberger, F. Krausz, and U. Kleineberg, Science (80-.). **320**, 1614 (2008).

[58] A. M. Weiner, J. P. Heritage, and E. M. Kirschner, J. Opt. Soc. Am. B **5**, 1563 (1988).

[59] A. M. Weiner, Rev. Sci. Instrum. **71**, 1929 (2000).

[60] Z. Jiang, D. E. Leaird, and A. M. Weiner, Opt. Express **13**, 10431 (2005).

[61] D. Meshulach and Y. Silberberg, Nature **396**, 239 (1998).

[62] N. Dudovich, D. Oron, and Y. Silberberg, Nature **418**, 512 (2002).

[63] J. A. Salehi, A. M. Weiner, and J. P. Heritage, J. Light. Technol. **8**, 478 (1990).

[64] I. S. Lin, J. D. McKinney, and A. M. Weiner, IEEE Microw. Wirel. Components Lett. **15**, 226 (2005).

[65] D. Sanvitto, F. M. Marchetti, M. H. Szymańska, G. Tosi, M. Baudisch, F. P. Laussy, D. N. Krizhanovskii, M. S. Skolnick, L. Marrucci, A. Lemaître, J. Bloch, C. Tejedor, and L. Viña, Nat. Phys. **6**, 527 (2010).

[66] M. V. Berry, J. Mod. Opt. **34**, 1401 (1987).

[67] S. Pancharatnam, Proc. Indian Acad. Sci. - Sect. A **44**, 247 (1956).

[68] E. Cohen, H. Larocque, F. Bouchard, F. Nejadsattari, Y. Gefen, and E. Karimi, Nat. Rev. Phys. **1**, 437 (2019).

[69] H. Larocque, J. Gagnon-Bischoff, F. Bouchard, R. Fickler, J. Upham, R. W. Boyd, and E. Karimi, J. Opt. **18**, 124002 (2016).

[70] N. R. Heckenberg, R. McDuff, C. P. Smith, H. Rubinsztein-Dunlop, and M. J. Wegener, Opt. Quantum Electron. **24**, S951 (1992).

[71] J. Arlt, K. Dholakia, L. Allen, and M. J. Padgett, J. Mod. Opt. **45**, 1231 (1998).

[72] A. Forbes, A. Dudley, and M. McLaren, Adv. Opt. Photonics **8**, 200 (2016).

[73] J. Leach and M. Padgett, New J. Phys. **5**, 154 (2003).

[74] G. Gariepy, J. Leach, K. T. Kim, T. J. Hammond, E. Frumker, R. W. Boyd, and P. B. Corkum, Phys. Rev. Lett. **113**, 153901 (2014).

[75] L. Allen, M. W. Beijersbergen, R. J. C. Spreeuw, and J. P. Woerdman, Phys. Rev. A **45**, 8185 (1992).

[76] L. Marrucci, C. Manzo, and D. Paparo, Phys. Rev. Lett. **96**, 163905 (2006).

[77] M. R. Dennis, R. P. King, B. Jack, K. O'Holleran, and M. J. Padgett, Nat. Phys. **6**, 118 (2010).

[78] J. Leach, M. R. Dennis, J. Courtial, and M. J. Padgett, New J. Phys. **7**, 55 (2005).

[79] H. Larocque, D. Sugic, D. Mortimer, A. J. Taylor, R. Fickler, R. W. Boyd, M. R. Dennis, and E. Karimi, Nat. Phys. **14**, 1079 (2018).

[80] A. E. Willner, H. Huang, Y. Yan, Y. Ren, N. Ahmed, G. Xie, C. Bao, L. Li, Y. Cao, Z. Zhao, J. Wang, M. P. J. Lavery, M. Tur, S. Ramachandran, A. F. Molisch, N. Ashrafi, and S. Ashrafi, Adv. Opt. Photonics **7**, 66 (2015).

[81] A. Mair, A. Vaziri, G. Weihs, and A. Zeilinger, Nature **412**, 313 (2001).

[82] A. Vaziri, J.-W. Pan, T. Jennewein, G. Weihs, and A. Zeilinger, Phys. Rev. Lett. **91**, 227902 (2003).

[83] F. Bouchard, R. Fickler, R. W. Boyd, and E. Karimi, Sci. Adv. **3**, e1601915 (2017).

[84] A. Sit, F. Bouchard, R. Fickler, J. Gagnon-Bischoff, H. Larocque, K. Heshami, D. Elser, C. Peuntinger, K. Günthner, B. Heim, C. Marquardt, G. Leuchs, R. W. Boyd, and E. Karimi, Optica **4**, 1006 (2017).

[85] G. Gibson, J. Courtial, M. J. Padgett, M. Vasnetsov, V. Pas'ko, S. M. Barnett, and S. Franke-Arnold, Opt. Express **12**, 5448 (2004).

[86] J. Wang, J.-Y. Yang, I. M. Fazal, N. Ahmed, Y. Yan, H. Huang, Y. Ren, Y. Yue, S. Dolinar, M. Tur, and A. E. Willner, Nat. Photonics **6**, 488 (2012).

[87] K. J. Mitchell, N. Radwell, S. Franke-Arnold, M. J. Padgett, and D. B. Phillips, Opt. Express **25**, 25079 (2017).

[88] S. W. Hell and J. Wichmann, Opt. Lett. **19**, 780 (1994).

[89] T. A. Klar and S. W. Hell, Opt. Lett. **24**, 954 (1999).

[90] M. D. Seaberg, D. E. Adams, E. L. Townsend, D. A. Raymondson, W. F. Schlotter, Y. Liu, C. S. Menoni, L. Rong, C.-C. Chen, J. Miao, H. C. Kapteyn, and M. M. Murnane, Opt. Express **19**, 22470 (2011).

[91] A. Ravasio, D. Gauthier, F. R. N. C. Maia, M. Billon, J.-P. Caumes, D. Garzella, M. Géléoc, O. Gobert, J.-F. Hergott, A.-M. Pena, H. Perez, B. Carré, E. Bourhis, J. Gierak, A. Madouri, D. Mailly, B. Schiedt, M. Fajardo, J. Gautier, P. Zeitoun, P. H. Bucksbaum, J. Hajdu, and H. Merdji, Phys. Rev. Lett. **103**, 028104 (2009).

[92] M. D. Seaberg, B. Zhang, D. F. Gardner, E. R. Shanblatt, M. M. Murnane, H. C. Kapteyn, and D. E. Adams, Optica **1**, 39 (2014).

[93] O. Kfir, S. Zayko, C. Nolte, M. Sivis, M. Möller, B. Hebler, S. S. P. K. Arekapudi, D. Steil, S. Schäfer, M. Albrecht, O. Cohen, S. Mathias, and C. Ropers, Sci. Adv. **3**, eaao4641 (2017).

[94] S. C. Tidwell, D. H. Ford, and W. D. Kimura, Appl. Opt. **29**, 2234 (1990).

[95] F. Cardano, E. Karimi, S. Slussarenko, L. Marrucci, C. de Lisio, and E. Santamato, Appl. Opt. **51**, C1 (2012).

[96] Q. Zhan, Adv. Opt. Photonics **1**, 1 (2009).

[97] K. S. Youngworth and T. G. Brown, Opt. Express **7**, 77 (2000).

[98] S. Quabis, R. Dorn, M. Eberler, O. Glöckl, and G. Leuchs, Opt. Commun. **179**, 1 (2000).

[99] D. P. Biss, K. S. Youngworth, and T. G. Brown, Appl. Opt. **45**, 470 (2006).

[100] Y. Kozawa and S. Sato, Opt. Express **18**, 10828 (2010).

[101] Q. Zhan, Opt. Express **12**, 3377 (2004).

[102] M. Meier, V. Romano, and T. Feurer, Appl. Phys. A **86**, 329 (2007).

[103] M. G. Rahimian, F. Bouchard, H. Al-Khazraji, E. Karimi, P. B. Corkum, and V. R. Bhardwaj, APL Photonics **2**, 086104 (2017).

[104] V. G. Niziev and A. V Nesterov, J. Phys. D. Appl. Phys. **32**, 1455 (1999).

[105] Q. Zhan and J. Leger, Opt. Express **10**, 324 (2002).

[106] S. Payeur, S. Fourmaux, B. E. Schmidt, J. P. MacLean, C. Tchervenkov, F. Légaré, M. Piché, and J. C. Kieffer, Appl. Phys. Lett. **101**, 041105 (2012).

[107] B. Hafizi, E. Esarey, and P. Sprangle, Phys. Rev. E **55**, 3539 (1997).

[108] G. D. Tsibidis, E. Skoulas, and E. Stratakis, Opt. Lett. **40**, 5172 (2015).

[109] M. Alameer, A. Jain, M. G. Rahimian, H. Larocque, P. B. Corkum, E. Karimi, and V. R. Bhardwaj, Opt. Lett. **43**, 5757 (2018).

[110] F. Kong, H. Larocque, E. Karimi, P. B. Corkum, and C. Zhang, Optica **6**, 160 (2019).

[111] L. Marrucci, J. Nanophotonics **7**, 078598 (2013).

[112] A. M. Beckley, T. G. Brown, and M. A. Alonso, Opt. Express **18**, 10777 (2010).

[113] G. M. Lerman, L. Stern, and U. Levy, Opt. Express **18**, 27650 (2010).

[114] M. Zürch, C. Kern, P. Hansinger, A. Dreischuh, and C. Spielmann, Nat. Phys. **8**, 743 (2012).

[115] R. Géneaux, A. Camper, T. Auguste, O. Gobert, J. Caillat, R. Taïeb, and T. Ruchon, Nat. Commun. **7**, 12583 (2016).

[116] A. Turpin, L. Rego, A. Picón, J. San Román, and C. Hernández-García, Sci. Rep. **7**, 43888 (2017).

[117] S. Li, B. Shen, X. Zhang, Z. Bu, and W. Gong, Opt. Express **26**, 23460 (2018).

[118] F. Kong, C. Zhang, F. Bouchard, Z. Li, G. G. Brown, D. H. Ko, T. J. Hammond, L. Arissian, R. W. Boyd, E. Karimi, and P. B. Corkum, Nat. Commun. **8**, 14970 (2017).

[119] A. Leblanc, A. Denoeud, L. Chopineau, G. Mennerat, P. Martin, and F. Quéré, Nat. Phys. **13**, 440 (2017).

[120] O. Kfir, P. Grychtol, E. Turgut, R. Knut, D. Zusin, D. Popmintchev, T. Popmintchev, H. Nembach, J. M. Shaw, A. Fleischer, H. Kapteyn, M. Murnane, and O. Cohen, Nat. Photonics **9**, 99 (2015).

[121] A. Fleischer, O. Kfir, T. Diskin, P. Sidorenko, and O. Cohen, Nat. Photonics **8**, 543 (2014).

[122] D. D. Hickstein, F. J. Dollar, P. Grychtol, J. L. Ellis, R. Knut, C. Hernández-García,

D. Zusin, C. Gentry, J. M. Shaw, T. Fan, K. M. Dorney, A. Becker, A. Jaroń-Becker, H. C. Kapteyn, M. M. Murnane, and C. G. Durfee, Nat. Photonics **9**, 743 (2015).

[123] T. Fan, P. Grychtol, R. Knut, C. Hernández-García, D. D. Hickstein, D. Zusin, C. Gentry, F. J. Dollar, C. A. Mancuso, C. W. Hogle, O. Kfir, D. Legut, K. Carva, J. L. Ellis, K. M. Dorney, C. Chen, O. G. Shpyrko, E. E. Fullerton, O. Cohen, P. M. Oppeneer, D. B. Milošević, A. Becker, A. A. Jaroń-Becker, T. Popmintchev, M. M. Murnane, and H. C. Kapteyn, Proc. Natl. Acad. Sci. U. S. A. **112**, 14206 (2015).

[124] A. Singer, F. Sorgenfrei, A. P. Mancuso, N. Gerasimova, O. M. Yefanov, J. Gulden, T. Gorniak, T. Senkbeil, A. Sakdinawat, Y. Liu, D. Attwood, S. Dziarzhytski, D. D. Mai, R. Treusch, E. Weckert, T. Salditt, A. Rosenhahn, W. Wurth, and I. A. Vartanyants, Opt. Express **20**, 17480 (2012).

[125] R. L. Sandberg, A. Paul, D. A. Raymondson, S. Hädrich, D. M. Gaudiosi, J. Holtsnider, R. I. Tobey, O. Cohen, M. M. Murnane, H. C. Kapteyn, C. Song, J. Miao, Y. Liu, and F. Salmassi, Phys. Rev. Lett. **99**, 098103 (2007).

[126] H. Kinoshita, K. Kurihara, Y. Ishii, and Y. Torii, J. Vac. Sci. Technol. B Microelectron. Nanom. Struct. **7**, 1648 (1989).

[127] D. G. Stearns, R. S. Rosen, and S. P. Vernon, Appl. Opt. **32**, 6952 (1993).

[128] V. P. K. M.V. Ammosov, N.B. Delone, J. Exp. Theor. Phys. **64**, 1191 (1986).

[129] H. R. Reiss, Phys. Rev. A **22**, 1786 (1980).

[130] H. R. Reiss, in *Prog. Ultrafast Intense Laser Sci. III* (Springer Berlin Heidelberg, Berlin, Heidelberg, 2008), pp. 1–31.

[131] S. Haessler, J. Caillat, W. Boutu, C. Giovanetti-Teixeira, T. Ruchon, T. Auguste, Z. Diveki, P. Breger, A. Maquet, B. Carré, R. Taïeb, and P. Salières, Nat. Phys. **6**, 200 (2010).

[132] P. M. Paul, E. S. Toma, P. Breger, G. Mullot, F. Auge, P. Balcou, H. G. Muller, and P. Agostini, Science **292**, 1689 (2001).

[133] N. Dudovich, O. Smirnova, J. Levesque, Y. Mairesse, M. Y. Ivanov, D. M. Villeneuve, and P. B. Corkum, Nat. Phys. **2**, 781 (2006).

[134] Z. Li, F. Kong, G. Brown, T. Hammond, D.-H. Ko, C. Zhang, and P. B. Corkum, J. Phys. B At. Mol. Opt. Phys. **51**, 125601 (2018).

[135] K. T. Kim, C. Zhang, A. D. Shiner, S. E. Kirkwood, E. Frumker, G. Gariepy, A. Naumov, D. M. Villeneuve, and P. B. Corkum, Nat. Phys. **9**, 159 (2013).

[136] J. Lu, E. F. Cunningham, Y. S. You, D. A. Reis, and S. Ghimire, Nat. Photonics **13**, 96 (2019).

[137] T. Hammond, E. Balogh, and K. T. Kim, J. Phys. B At. Mol. Opt. Phys. **50**, 014006 (2017).

[138] Z. Li, G. Brown, D. H. Ko, F. Kong, L. Arissian, and P. B. Corkum, Phys. Rev. Lett. **118**, 033905 (2017).

[139] D. Gauthier, P. R. Ribič, G. Adhikary, A. Camper, C. Chappuis, R. Cucini, L. F. DiMauro, G. Dovillaire, F. Frassetto, R. Géneaux, P. Miotti, L. Poletto, B. Ressel, C. Spezzani, M. Stupar, T. Ruchon, and G. De Ninno, Nat. Commun. **8**, 14971 (2017).

[140] M. Padgett and R. Bowman, Nat. Photonics **5**, 343 (2011).

[141] E. Rittweger, K. Y. Han, S. E. Irvine, C. Eggeling, and S. W. Hell, Nat. Photonics **3**, 144 (2009).

[142] D. Naidoo, F. S. Roux, A. Dudley, I. Litvin, B. Piccirillo, L. Marrucci, and A. Forbes, Nat. Photonics **10**, 327 (2016).

[143] L. Marrucci, Mol. Cryst. Liq. Cryst. **488**, 148 (2008).

[144] L. Marrucci, E. Karimi, S. Slussarenko, B. Piccirillo, E. Santamato, E. Nagali, and F. Sciarrino, J. Opt. **13**, 064001 (2011).

[145] A. D. Shiner, C. Trallero-Herrero, N. Kajumba, H.-C. Bandulet, D. Comtois, F. Légaré, M. Giguère, J.-C. Kieffer, P. B. Corkum, and D. M. Villeneuve, Phys. Rev. Lett. **103**, 073902 (2009).

[146] J. B. Bertrand, H. J. Wörner, H.-C. Bandulet, É. Bisson, M. Spanner, J.-C. Kieffer, D. M. Villeneuve, and P. B. Corkum, Phys. Rev. Lett. **106**, 023001 (2011).

[147] J. B. Bertrand, H. J. Wörner, P. Salières, D. M. Villeneuve, and P. B. Corkum, Nat. Phys. **9**, 174 (2013).

[148] S. Straupe and S. Kulik, Nat. Photonics **4**, 585 (2010).

[149] L. Marrucci, C. Manzo, and D. Paparo, Appl. Phys. Lett. **88**, 221102 (2006).

[150] C. Gohle, T. Udem, M. Herrmann, J. Rauschenberger, R. Holzwarth, H. A. Schuessler, F. Krausz, and T. W. Hänsch, Nature **436**, 234 (2005).

[151] L. Mercadier, J. Peng, Y. Sultan, T. A. Davis, D. M. Rayner, and P. B. Corkum, Appl. Phys. Lett. **103**, 061107 (2013).

[152] X. Yu, Z. Chang, P. B. Corkum, and S. Lei, Opt. Lett. **39**, 5638 (2014).

[153] A. V. Kimel, A. Kirilyuk, P. A. Usachev, R. V. Pisarev, A. M. Balbashov, and T. Rasing, Nature **435**, 655 (2005).

[154] C. Maurer, A. Jesacher, S. Fürhapter, S. Bernet, and M. Ritsch-Marte, New J. Phys. **9**, 78 (2007).

[155] C. Hernández-García, A. Turpin, J. San Román, A. Picón, R. Drevinskas, A. Cerkauskaite, P. G. Kazansky, C. G. Durfee, and Í. J. Sola, Optica **4**, 520 (2017).

[156] D. B. Milošević, W. Becker, and R. Kopold, Phys. Rev. A **61**, 063403 (2000).

[157] P.-C. Huang, C. Hernández-García, J.-T. Huang, P.-Y. Huang, C.-H. Lu, L. Rego, D. D. Hickstein, J. L. Ellis, A. Jaron-Becker, A. Becker, S.-D. Yang, C. G. Durfee, L. Plaja, H. C. Kapteyn, M. M. Murnane, A. H. Kung, and M.-C. Chen, Nat. Photonics **12**, 349 (2018).

[158] F. Cardano, E. Karimi, L. Marrucci, C. de Lisio, and E. Santamato, Opt. Express **21**,

8815 (2013).

[159] S. Slussarenko, A. Murauski, T. Du, V. Chigrinov, L. Marrucci, and E. Santamato, Opt. Express **19**, 4085 (2011).

[160] P. R. Ribič, D. Gauthier, and G. De Ninno, Phys. Rev. Lett. **112**, 203602 (2014).

[161] J. Levesque, Y. Mairesse, N. Dudovich, H. Pépin, J.-C. Kieffer, P. B. Corkum, and D. M. Villeneuve, Phys. Rev. Lett. **99**, 243001 (2007).

[162] K.-J. Yuan and A. D. Bandrauk, Phys. Rev. A **97**, 023408 (2018).

[163] M. Y. Ivanov, M. Spanner, and O. Smirnova, J. Mod. Opt. **52**, 165 (2005).

[164] G. van der Laan and A. I. Figueroa, Coord. Chem. Rev. **277**–**278**, 95 (2014).

[165] W. Harm, S. Bernet, M. Ritsch-Marte, I. Harder, and N. Lindlein, Opt. Express **23**, 413 (2015).

[166] L. Shi, Z. Zhang, A. Cao, X. Luo, and Q. Deng, Opt. Express **23**, 8620 (2015).

[167] S. Fuchs, C. Rödel, A. Blinne, U. Zastrau, M. Wünsche, V. Hilbert, L. Glaser, J. Viefhaus, E. Frumker, P. Corkum, E. Förster, and G. G. Paulus, Sci. Rep. **6**, 20658 (2016).

[168] C. Wagner and N. Harned, Nat. Photonics **4**, 24 (2010).

[169] P. Antoine, A. L'Huillier, M. Lewenstein, P. Salières, and B. Carré, Phys. Rev. A **53**, 1725 (1996).

[170] N. Saito, P. Xia, F. Lu, T. Kanai, J. Itatani, and N. Ishii, Optica **4**, 1333 (2017).

[171] A. Ferré, C. Handschin, M. Dumergue, F. Burgy, A. Comby, D. Descamps, B. Fabre, G. A. Garcia, R. Géneaux, L. Merceron, E. Mével, L. Nahon, S. Petit, B. Pons, D. Staedter, S. Weber, T. Ruchon, V. Blanchet, and Y. Mairesse, Nat. Photonics **9**, 93 (2015).

[172] G. Lambert, B. Vodungbo, J. Gautier, B. Mahieu, V. Malka, S. Sebban, P. Zeitoun, J. Luning, J. Perron, A. Andreev, S. Stremoukhov, F. Ardana-Lamas, A. Dax, C. P. Hauri, A. Sardinha, and M. Fajardo, Nat. Commun. **6**, 6167 (2015).

[173] G. Walker, A. S. Arnold, and S. Franke-Arnold, Phys. Rev. Lett. **108**, 243601 (2012).

[174] N. V. Bloch, K. Shemer, A. Shapira, R. Shiloh, I. Juwiler, and A. Arie, Phys. Rev. Lett. **108**, 233902 (2012).

[175] K. Dholakia, N. B. Simpson, M. J. Padgett, and L. Allen, Phys. Rev. A **54**, R3742 (1996).

[176] E. Karimi, B. Piccirillo, L. Marrucci, and E. Santamato, Opt. Lett. **34**, 1225 (2009).

[177] M. Sivis, M. Taucer, G. Vampa, K. Johnston, A. Staudte, A. Y. Naumov, D. M. Villeneuve, C. Ropers, and P. B. Corkum, Science **357**, 303 (2017).

[178] J. Leach, J. Courtial, K. Skeldon, S. M. Barnett, S. Franke-Arnold, and M. J. Padgett, Phys. Rev. Lett. **92**, 013601 (2004).

[179] M. Harris, C. A. Hill, P. R. Tapster, and J. M. Vaughan, Phys. Rev. A **49**, 3119 (1994).

[180] H. J. Simon and N. Bloembergen, Phys. Rev. **171**, 1104 (1968).

[181] C. L. Tang and H. Rabin, Phys. Rev. B **3**, 4025 (1971).

[182] Y. S. You, D. A. Reis, and S. Ghimire, Nat. Phys. **13**, 345 (2017).

[183] R. Dorn, S. Quabis, and G. Leuchs, Phys. Rev. Lett. **91**, 233901 (2003).

[184] M. Uiberacker, T. Uphues, M. Schultze, A. J. Verhoef, V. Yakovlev, M. F. Kling, J. Rauschenberger, N. M. Kabachnik, H. Schröder, M. Lezius, K. L. Kompa, H.-G. Muller, M. J. J. Vrakking, S. Hendel, U. Kleineberg, U. Heinzmann, M. Drescher, and F. Krausz, Nature **446**, 627 (2007).

[185] K. Y. Bliokh, E. A. Ostrovskaya, M. A. Alonso, O. G. Rodríguez-Herrera, D. Lara, and C. Dainty, Opt. Express **19**, 26132 (2011).

[186] K. Y. Bliokh, F. J. Rodríguez-Fortuño, F. Nori, and A. V. Zayats, Nat. Photonics **9**, 796 (2015).

[187] D. Pohl, Appl. Phys. Lett. **20**, 266 (1972).

[188] M. Stalder and M. Schadt, Opt. Lett. **21**, 1948 (1996).

[189] M. R. Beversluis, L. Novotny, and S. J. Stranick, Opt. Express **14**, 2650 (2006).

[190] M. Nisoli and G. Sansone, Prog. Quantum Electron. **33**, 17 (2009).

[191] M. Nisoli, S. De Silvestri, O. Svelto, R. Szipöcs, K. Ferencz, C. Spielmann, S. Sartania, and F. Krausz, Opt. Lett. **22**, 522 (1997).

[192] B. E. Schmidt, A. D. Shiner, P. Lassonde, J.-C. Kieffer, P. B. Corkum, D. M. Villeneuve, and F. Légaré, Opt. Express **19**, 6858 (2011).

[193] W. J. Tomlinson, R. H. Stolen, and C. V. Shank, J. Opt. Soc. Am. B **1**, 139 (1984).

[194] M. Nisoli, S. De Silvestri, and O. Svelto, Appl. Phys. Lett. **68**, 2793 (1996).

[195] C. Zhang, G. Vampa, D. M. Villeneuve, and P. B. Corkum, J. Phys. B At. Mol. Opt. Phys. **48**, 061001 (2015).

[196] L. Yan, P. Gregg, E. Karimi, A. Rubano, L. Marrucci, R. Boyd, and S. Ramachandran, Optica **2**, 900 (2015).

[197] B. E. Schmidt, P. Béjot, M. Giguère, A. D. Shiner, C. Trallero-Herrero, É. Bisson, J. Kasparian, J.-P. Wolf, D. M. Villeneuve, J.-C. Kieffer, P. B. Corkum, and F. Légaré, Appl. Phys. Lett. **96**, 121109 (2010).

[198] M. Beresna, M. Gecevičius, P. G. Kazansky, and T. Gertus, Appl. Phys. Lett. **98**, 201101 (2011).

[199] V. Cardin, N. Thiré, S. Beaulieu, V. Wanie, F. Légaré, and B. E. Schmidt, Appl. Phys. Lett. **107**, 181101 (2015).

[200] M. Seidel, G. Arisholm, J. Brons, V. Pervak, and O. Pronin, Opt. Express **24**, 9412

(2016).

[201] C.-H. Lu, Y.-J. Tsou, H.-Y. Chen, B.-H. Chen, Y.-C. Cheng, S.-D. Yang, M.-C. Chen, C.-C. Hsu, and A. H. Kung, Optica **1**, 400 (2014).

[202] C. Varin, S. Payeur, V. Marceau, S. Fourmaux, A. April, B. Schmidt, P.-L. Fortin, N. Thiré, T. Brabec, F. Légaré, J.-C. Kieffer, M. Piché, C. Varin, S. Payeur, V. Marceau, S. Fourmaux, A. April, B. Schmidt, P.-L. Fortin, N. Thiré, T. Brabec, F. Légaré, J.-C. Kieffer, and M. Piché, Appl. Sci. **3**, 70 (2013).

[203] R. Kienberger, E. Goulielmakis, M. Uiberacker, A. Baltuska, V. Yakovlev, F. Bammer, A. Scrinzi, T. Westerwalbesloh, U. Kleineberg, U. Heinzmann, M. Drescher, and F. Krausz, Nature **427**, 817 (2004).

[204] F. Ferrari, F. Calegari, M. Lucchini, C. Vozzi, S. Stagira, G. Sansone, and M. Nisoli, Nat. Photonics **4**, 875 (2010).

[205] R. Bartels, S. Backus, E. Zeek, L. Misoguti, G. Vdovin, I. P. Christov, M. M. Murnane, and H. C. Kapteyn, Nature **406**, 164 (2000).

[206] C. Jin, G. Wang, H. Wei, A.-T. Le, and C. D. Lin, Nat. Commun. **5**, 4003 (2014).

[207] N. Ishii, K. Kaneshima, K. Kitano, T. Kanai, S. Watanabe, and J. Itatani, Nat. Commun. **5**, 3331 (2014).

[208] J. Peatross, J. L. Chaloupka, and D. D. Meyerhofer, Opt. Lett. **19**, 942 (1994).

[209] H. Vincenti and F. Quéré, Phys. Rev. Lett. **108**, 113904 (2012).

[210] M. Shapiro and P. Brumer, *Quantum Control of Molecular Processes* (Wiley-VCH, 2012).

[211] E. Dupont, P. B. Corkum, H. C. Liu, M. Buchanan, and Z. R. Wasilewski, Phys. Rev. Lett. **74**, 3596 (1995).

[212] S. Sederberg, F. Kong, and P. Corkum, ArXiv 1901.07444 (2019).